



THESIS  
2  
2001

This is to certify that the

thesis entitled

**The Influence of the Microstructure of Sintered  
Hydroxyapatite on the Properties of Hardness, Fracture  
Toughness, Thermal Expansion and the Dielectric Permittivity**

presented by

Timothy P. Hoepfner

has been accepted towards fulfillment  
of the requirements for

Master's degree in Materials Science  
and Engineering

Eldon D. Case

Major professor

Date April 23, 2001

**LIBRARY**  
**Michigan State**  
**University**

**PLACE IN RETURN BOX** to remove this checkout from your record.  
**TO AVOID FINES** return on or before date due.  
**MAY BE RECALLED** with earlier due date if requested.

DATE DUE	DATE DUE	DATE DUE
APR 05 2004		
AUG 27 2006		
DEC 12 2009		

**THE INFLUENCE OF THE MICROSTRUCTURE OF SINTERED  
HYDROXYAPATITE ON THE PROPERTIES OF HARDNESS, FRACTURE  
TOUGHNESS, THERMAL EXPANSION AND THE DIELECTRIC PERMITTIVITY**

**By**

**Timothy P. Hoepfner**

**A THESIS**

**Submitted to  
Michigan State University  
in partial fulfillment of the requirements  
for the degree of**

**MASTER OF SCIENCE**

**Department of Materials Science and Mechanics**

**April 2001**

## ABSTRACT

### THE INFLUENCE OF THE MICROSTRUCTURE OF SINTERED HYDROXYAPATITE ON THE PROPERTIES OF HARDNESS, FRACTURE TOUGHNESS, THERMAL EXPANSION AND THE DIELECTRIC PERMITTIVITY

By

Timothy P. Hoepfner

Sintered hydroxyapatite specimens with a 58-98% relative density range and average grain sizes between 1.64  $\mu\text{m}$  and 7.44  $\mu\text{m}$  were made with a commercial hydroxyapatite powder. No decomposition of the hydroxyapatite was detected, by x-ray diffraction, for any specimen. Vickers hardness ( $H_v$ ) of the sintered hydroxyapatite specimens was successfully fit, as a function of the volume fraction porosity ( $P$ ), to the minimum solid area model (MSA):  $H_v = H_{v0} e^{-bP}$ . The zero porosity hardness value  $H_{v0} = 6.00 \pm 0.79$  GPa and the material dependent constant  $b = 6.03$ . Fracture toughness ( $K_{Ic0}$ ) of the sintered hydroxyapatite specimens, measured by indentation methods, diverged from the MSA model. Fracture toughness increased as the porosity increased.  $K_{Ic0} \approx 0.5$  MPa  $\text{m}^{1/2}$  for sintered hydroxyapatite specimens of 97% relative density increasing to  $K_{Ic0} \approx 2.6$  MPa  $\text{m}^{1/2}$  for specimens of 72% relative density. Thermal expansion coefficients for sintered hydroxyapatite, measured by dilatometry =  $12.9 \times 10^{-6} / ^\circ\text{C}$  at  $100^\circ\text{C}$ ,  $13.8 \times 10^{-6} / ^\circ\text{C}$  at  $200^\circ\text{C}$ ,  $16.3$  at  $400^\circ\text{C}$  and  $19.8 \times 10^{-6} / ^\circ\text{C}$  at  $600^\circ\text{C}$ . The relative dielectric permittivity was measured for several sintered hydroxyapatite specimens of varying porosity and the zero porosity relative dielectric permittivity was calculated using a dielectric mixing law to  $k_0 = 17.63 \pm 0.70$ .

## TABLE OF CONTENTS

LIST OF TABLES	vii
LIST OF FIGURES	x
<b>1.0 Introduction</b>	<b>1</b>
1.1 Goals of research	1
1.2 Chemistry of sintering	2
1.2.1 Dehydroxylation and decomposition	2
1.2.2 Process control of phase purity during sintering	3
1.3 Relevant crystal structures	4
1.3.1 Hydroxyapatite	4
1.3.2 Tricalcium phosphate	8
1.3.3 Tetra calcium phosphate	8
1.4 Microstructure of sintered hydroxyapatite	8
1.4.1 Residual strain energy and microcracking	9
1.5 Microstructure and material Properties	10
1.5.1 Indentation hardness	10
1.5.2 Indentation method to determine fracture toughness	10
1.5.3 Hardness and fracture toughness studies	13
1.5.4 Fracture energy and microstructure	16
1.5.5 Indentation studies of sintered hydroxyapatite	17
1.5.6 Summary of hardness and toughness studies	21
1.5.6.1 Hardness	21

1.5.6.2	Fracture toughness	21
1.6	Material properties and porosity and the minimum solid area	22
1.7	Thermal expansion and microstructure	24
1.7.1	Thermal expansion and microcracking	25
1.8	Dielectric properties and microstructure	25
<b>2.0</b>	<b>Experimental Procedure</b>	<b>27</b>
2.1	Starting material	27
2.1.1	Particle size analysis	27
2.1.2	Ball milling	28
2.2	Specimen preparation	28
2.2.1	Die forming	30
2.2.2	Cold isostatic pressure	30
2.2.3	Conventional furnace sintering	37
2.2.4	Microwave sintering	39
2.2.5	Sectioning the sintered specimens	41
2.2.6	Specimen polishing	43
2.2.7	Surface etching	44
2.2.8	Specimen mounting for scanning electron microscopy	45
2.3	Microstructure measurements	45
2.3.1	Mass density	45
2.3.2	Grain size measurements	46
2.3.3	X-ray diffraction	48
2.4	Hardness and fracture toughness measurements	50

2.5	Thermal expansion	51
2.5.1	Specimen preparation for thermal expansion measurements	51
2.5.2	Thermal expansion measurement	51
2.6	Dielectric measurements	52
2.6.1	Specimen preparation for dielectric measurements	52
2.6.2	Dielectric apparatus and measurements	52
<b>3.0</b>	<b>Results and Discussion</b>	<b>56</b>
3.1	Sintered hydroxyapatite microstructure	56
3.1.1	Sintered density	56
3.1.2	Sintered grain size	56
3.1.3	Etched surface morphology	64
3.1.4	X-ray diffraction	64
3.2	Indentation measurements	76
3.2.1	Vickers hardness	76
3.2.2	Indentation fracture toughness	81
3.2.2	Thermal expansion	
3.3	Hardness and microstructure comparisons with literature data	81
3.4	Fracture toughness and microstructure comparisons with literature data	91
3.5	Further comment on the fracture toughness of sintered hydroxyapatite	98
3.5.1	Indentation toughness model and porosity	99
3.5.1.1	Effect of $E(P_p)$ on the fracture toughness of sintered hydroxyapatite	104

3.5.1.2	Indentation fracture toughness of porous $\text{YBa}_2\text{Ca}_3\text{O}_{7-x}$	106
3.5.1.3	Porosity dependence of the empirical constant $\zeta$	110
3.5.2	Examples of deviations from the MSA model for fracture toughness	114
3.5.3	Possible toughening mechanisms in sintered hydroxyapatite	114
3.6	Thermal expansion	120
3.7	Dielectric measurements	128
3.7.1	Circuit capacitance measurement and correction	128
3.7.2	The relative permittivity of hydroxyapatite	129
4.0	Summary and Conclusions	135
4.1	Further research	137
	Appendix A	139
	Appendix B	147
	References	154

## LIST OF TABLES

Table 1-1	A survey of secondary phase formation in sintered hydroxyapatite under varied sintering conditions for various studies from the literature.	5
Table 1-2	Ceramic oxides in which the bulk thermal expansion coefficient was constant for a variety of grain sizes and porosity.	24
Table 2-1	Specific analysis (Ca percentages) and spectrographic analysis (impurities) of the hydroxyapatite powder received from CERAC Inc., Milwaukee, WI. The data is copied from the Certificate of Analysis attached to material.	27
Table 2-2	Processing parameters for Hydroxyapatite disk specimens. Fired in automatically controlled tube furnace. HAP I is lot number X16907 from CERAC inc. Milwaukee, WI.	31
Table 2-3	Processing parameters for rectangular HAP Specimens, fired in C+M box furnace under manual control. HAP II is from lot number X21949 from CERAC. HAP Ia, HAP IIa- hydroxyapatite powder ball milled with alumina pellets, HAP Iz- hydroxyapatite powder ball milled with zirconia pellets.	32
Table 2-4	Processing parameters for disk Specimens, fired in C+M box furnace under manual control	33
Table 2-5	Processing parameters for disk HAP Specimens fired in a microwave cavity.	34
Table 3-1	Processing parameters, density and grain size data for sintered hydroxyapatite.	57
Table 3-2	Lattice parameter data for the as received hydroxyapatite powder (HAP I) and sintered hydroxyapatite, calculated using the 3 major hydroxyapatite peaks from Figures 3-13 and 3-14 and Equations 2-2 and 2-3. Data from the handbook is included [69].	76

Table 3-3	Density, grain size and the mechanical properties of hardness and toughness, measured by indentation technique, of sintered hydroxyapatite. The standard deviations ( $\sigma$ ), calculated for the multiple indentations per specimen, are included.	78
Table 3-4	The normalization and statistical parameters from the linear regression analysis of the hardness as a function of volume fraction porosity (Equation 3-1: $\ln H = \ln H_0 - bP$ ) for this study, Wang et al. [9], Slosarczyk et al. [11], Best et al. [75], and Lu et al. [74]. Actual hardness data [9,11,74,75] from the literature is included.	88
Table 3-5	The normalization and statistical parameters from the linear regression analysis of toughness as a function of volume fraction porosity (Equation 3-2: $\ln K_{Ic} = \ln K_{0,ic} - bP$ ) for this study, DeWith et al. [54] and Suchanek et al. [56]. Fracture toughness data from DeWith et al. [54] and Suchanek et al. [56] are included.	92
Table 3-6	Porosity dependence of the elastic modulus compared to the porosity dependence of Poisson's ratio for experimental data fit to the MSA model ( $\ln E = \ln E_0 - b_E P$ , $\ln \nu = \ln \nu_0 - b_\nu P$ , Equation 1-8) by Rice [58].	101
Table 3-7	Material dependent coefficients ( $b_H$ and $b_E$ ) from the MSA model [57] for $Al_2O_3$ , $B_4C$ , $AlN$ and $SiO_2$ ceramics calculated by Rice [58]. The HAP (hydroxyapatite) elastic modulus attenuation coefficient was calculated for this study using DeWith et al.'s data [54]. The hardness attenuation coefficient for HAP has been determined previously in this study (Table 3-4).	103
Table 3-8	Experimental data for $YBa_2Cu_3O_{7-x}$ from Tancret et al. [78] and the fit, for this study, to the MSA model $\ln(A) = \ln(A_0) - b_A P_p$ , where A represents the property (E, $H_v$ , etc.), $A_0$ = the property at zero porosity (y-intercept for the linear regression), $b_A$ is the slope of the log-linear relation, and $P_p$ is the volume fraction porosity. Included for comparison are the fracture toughness values calculated, for each porosity, using equation 3-3 $\{K_{Ic} = \zeta(E/H)^{1/2} P c^{-3/2}\}$ , for this study. Column 6 contains the fracture toughness calculated with constant elastic modulus ( $E = 120$ GPa), $\{K_{Ic}(\text{Indent, constant } E)\}$ . Fracture toughness values in column 7 were calculated using the measured specimen elastic modulus [78], in equation 3-3 $\{K_{Ic}(\text{Indent})\}$ .	108
Table 3-9	Comparison of the zero porosity mechanical properties of $YBa_2Cu_3O_{7-x}$ and HAP ( $Ca_{10}(PO_4)_6(OH)_2$ ).	112

Table 3-10	Fracture toughness/porosity trends fit to the MSA model ( $\ln(K_{ic0}) = \ln(K_{ic0}) - b_k P_p$ ) from the literature data for a variety of porous ceramics. The processing method (prc) and fracture toughness test method (meth.) are included.	116
Table 3-11	Thermal expansion data for Alumina, from <i>American Institute of Physics Handbook 2<sup>nd</sup> Edition</i> [76].	120
Table 3-12	The averaged thermal expansion coefficients for sintered hydroxyapatite specimen numbers 4-8, and 10-12 by dilatometry. The delta is the difference between the cooling data and the heating data: $\Delta = \alpha_{cool} - \alpha_{heat}$ .	125
Table 3-13	Dielectric characteristics for Coors ADS 995 alumina substrate. Data from Tech Specs, Thin Film Substrates Technical Specifications 10-3-0897 from Coors Ceramics, Golden, CO [72].	128
Table 3-14	Relative permittivity for sintered hydroxyapatite from this study and Fanovich et al. [78] and the fit parameters for the Maxwell-Garnet equations.	130

## LIST OF FIGURES

Figure 1-1	Vickers indentation impression and the characteristic dimensions used in the hardness calculation and the toughness equation (Equation 1-6), A) top view left and B) side view. A schematic of the side view of representative Palmqvist cracks is given in C) [42].	12
Figure 2-1	Particle size analysis from Cerac, Inc.[66] for hydroxyapatite powder lot numbers X16907T and X21949, used in this study. Mean values were 10.03 and 8.81 microns with standard deviations of 6.94 and 7.05 microns for hydroxyapatite powder lots X16907T and X21949 respectively.	29
Figure 2-2	Pressing die for disk specimens, fabricated from hardened steel by the Michigan State University Physics Department Machine Shop.	35
Figure 2-3	Rectangular die press, fabricated from hardened steel by the Michigan State University Physics Department Machine Shop. Tolerances set to 0.001". Bolted together with 5/16" - 18, hex head bolts before pressing.	36
Figure 2-4	Microwave casket assembly. Hydroxyapatite green bodies were placed on the porous alumina disk. The optical thermometer measured the temperature by from the light emitted through the hole 1 cm above the alumina.	40
Figure 2-5	Microwave furnace power supply, controls and microwave cavity schematic.	42
Figure 2-6	Apparatus for measuring the mass density of the hydroxyapatite specimens using Archimedes method. The sintered specimens were placed into the basket for the suspended mass measurement.	47
Figure 2-7	Electrodes and experimental apparatus for the dielectric measurements. The specimen was placed between the top and bottom electrodes. The electrodes were pressed onto the hydroxyapatite surfaces by a 5.09 cm maximum opening micrometer (not shown).	53
Figure 2-8	Parallel circuit for Q-meter measurements.	55

Figure 3-1	Density as a function of sintering time and different uniaxial die pressures for hydroxyapatite sintered in the conventional furnaces at 1300 °C. The data was taken from a subset of the data presented in Table 3-1.	60
Figure 3-2	Density as a function of die pressure. The data was taken from sintered hydroxyapatite specimens sintered at 1300° C for 15-120 minutes, which are a subset of the data presented in Table 3-1. Linear fit represents the least squares fit of the data to equation 3-1. Fit parameters are slope = 0.27% relative density per 1 MPa die pressure, y-intercept = 91% relative density and the coefficient of determination $r^2 = 0.997$ .	61
Figure 3-3	Density as a function of sintering temperature for hydroxyapatite specimens sintered for 60 minutes. The data was taken from a subset of the data presented in Table 3-1.	62
Figure 3-4	Average grain size of sintered hydroxyapatite as a function of sintering temperature and time for both conventional and microwave sintering. The data was taken from a subset of the data presented in Table 3-1.	63
Figure 3-5	Grain size as a function of percent relative density for sintered hydroxyapatite. The data was taken from a subset of the data presented in Table 3-1.	65
Figure 3-6	Micrographs of polished and thermally etched surface of sintered hydroxyapatite specimen number 15 sintered at 1300° C for 45 minutes, average grain size = 3.60 microns.	66
Figure 3-7	Micrograph of polished and thermally etched surface of sintered hydroxyapatite specimen number 45 sintered at 1350° C for 60 minutes, average grain size = 4.59 microns.	67
Figure 3-8	Micrographs of polished and acid etched surface of sintered hydroxyapatite (0.1 M HCl for 1 minute), (a) specimen number 3 sintered at 1300° C for 45 minutes, grain size =1.98 microns, (b) specimen number 8 sintered at 1400° C degrees for 240 minutes, grain size = 7.44 microns.	68
Figure 3-9	Polished and thermally etched surfaces of cold isostatically pressed (250 MPa) and sintered hydroxyapatite specimen number 22 sintered at 1200° C for 15 minutes. Average grain size = 1.99 μm.	69

Figure 3-10	Polished and thermally etched surfaces of cold isostatically pressed (250 MPa) and sintered hydroxyapatite specimen number 23 sintered at 1250 <sup>0</sup> C for 30 minutes. Average grain size = 2.06 μm.	70
Figure 3-11	Polished and thermally etched surfaces of cold isostatically pressed (250 MPa) and sintered hydroxyapatite specimen number 20 sintered at 1300 <sup>0</sup> C for 15 minutes. Average grain size = 2.30 μm.	71
Figure 3-12	Polished and thermally etched surfaces of cold isostatically pressed (250 MPa) and sintered hydroxyapatite specimen number 21 sintered at 1300 <sup>0</sup> C for 120 minutes., Average grain size = 2.60 μm.	72
Figure 3-13	X-ray diffraction pattern (Cu K <sub>α1</sub> radiation) for the as-received powder and sintered hydroxyapatite (HAP) specimens numbers 6 thru 9.	74
Figure 3-14	Additional x-ray diffraction patterns (Cu K <sub>α1</sub> radiation) for sintered hydroxyapatite specimens numbers 11 and 12.	75
Figure 3-15	Vickers indentation Hardness values for sintered hydroxyapatite as a function of density. The data was taken from Table 3-3.	79
Figure 3-16	Vickers Hardness plotted against the average grain size of the sintered hydroxyapatite. The data was taken from Table 3-3.	80
Figure 3-17	Statistical standard deviation of the Vickers hardness of sintered hydroxyapatite plotted against the average grain size. The data was taken from Table 3-3.	82
Figure 3-18	Vickers indentation toughness as a function of density for sintered hydroxyapatite. The data was taken from Table 3-3.	83
Figure 3-19	Fracture toughness as a function of average grain size of sintered hydroxyapatite. The data was taken from Table 3-3.	84
Figure 3-20	Standard deviation of the fracture toughness plotted against the average grain size of the sintered hydroxyapatite. The data was taken from Table 3-3.	85
Figure 3-21	Ratio of the Vickers indentation crack length and Vickers indentation diagonal plotted against the % relative density, for all 410 indents on the specimens with known density measured in this study.	86

- Figure 3-22 Log relative indentation Hardness values for sintered hydroxyapatite plotted against the volume fraction porosity along with the solutions for the linear log relative hardness as a function of volume fraction porosity (Equation 1- 8, Section 1.6). Data was taken from Table 3-3 for the present study and Table 3-4 for the literature data. 90
- Figure 3-23 Fracture toughness values for sintered hydroxyapatite plotted against the volume fraction porosity. Fracture toughness values were taken from Table 3-3 (present study) and Table 3-5 for the data from Suchanek et al. [56] and DeWith et al. [54]. 94
- Figure 3-24 Relative fracture toughness values for sintered hydroxyapatite as a function of volume fraction porosity and the calculated linear fit. Linear fit parameters taken from Table 3-5 for the data from Table 3-3 (present study) and the fracture toughness data in Table 3-5 from Suchanek et al. [56] and DeWith et al. [54]. 96
- Figure 3-25 A section of lower volume fraction porosity of the relative fracture toughness values for sintered hydroxyapatite as a function of volume fraction porosity and the calculated linear fit. Linear fit parameters taken from Table 3-5 for the data from Table 3-3 (present study) and the fracture toughness data in Table 3-5 from Suchanek et al. [56] and DeWith et al. [54] . 97
- Figure 3-26  $(E/H)^{1/2}$  as a function of the volume fraction porosities normalize by  $(E_0/H_0)^{1/2}$ , the fully dense values of the elastic modulus and hardness respectively. The decay constants  $b_H$  and  $b_E$  are compiled by Rice [58] for  $Al_2O_3$ ,  $AlN$ ,  $B_4C$ , and  $SiO_2$  (Table 3-6). The  $b_H$  for HAP was determined in this study, while  $b_E$  for HAP was calculated in this study using the MSA model and DeWith et al.'s data [54] (Table 3-6). 105
- Figure 3-27 Calculated fracture toughness of the hydroxyapatite specimens in this study using the elastic modulus as function of volume fraction porosity  $\{K_{Ic}(E(P))\}$  (Equation 3-6, material dependent constant  $b_E = 2.93$  [54]). 107
- Figure 3-28 Crack parameter  $P/c^{3/2}$  as a function of the volume fraction porosity for hydroxyapatite from this study and for  $YBa_2Cu_3O_{7-x}$  from Tancret et al. [78]. The line through the  $YBa_2Cu_3O_{7-x}$  data is from the MSA fit ( $\ln P/c^{3/2} = \ln(P/c^{3/2}_0) - b_p P_p$ ) of the crack parameter  $P/c^{3/2}$  [78]. 109

Figure 3-29	Fracture toughness $\text{YBa}_2\text{Cu}_3\text{O}_{7-x}$ of as a function of the volume fraction porosity determined by SENB [78] (Table 3-7), Indentation method $K_{ic} = \zeta (E/H)^{1/2} P/c^{3/2}$ (Equation 3-3) with the data from Table 3-7, and the indentation method (Equation 3-3) with constant elastic modulus ( $E = 114 \text{ GPa}$ ) from Tancret et al. [78].	111
Figure 3-30	The fracture toughness of the sintered hydroxyapatite specimens in this study calculated with $\zeta(P_p)$ (Equation 3-8).	115
Figure 3-31	Normalized fracture toughness parameters (fracture toughness for Ricote [48], and fracture energy for Case et al. [81]) studies in which the fracture toughness parameters increased or decreased slightly, over a significant volume fraction porosity range. Normalization is done by dividing the fracture toughness by the zero porosity fracture toughness as determined by the intercept of the linear fit. The linear fit (included in plot) calculated for the entire range of Ricote et al's data [48]. The linear fit calculated for the Case et al. [81] data was done for specimens with $< 0.30$ volume fraction porosity. The ceramics in question are calcium modified lead titanate for Ricote [48] and gadolinia for Case et al. [81].	117
Figure 3-32	Normalized fracture toughness for sintered hydroxyapatite specimens in this study. Normalization is done by dividing the fracture toughness by the zero porosity fracture toughness as determined by the intercept of the linear fit. The linear fit (included in plot) was calculated for hydroxyapatite specimens $< 0.20$ volume fraction porosity.	118
Figure 3-33	Thermal expansion coefficient for high purity alumina determined by dilatometry, as a function of temperature and compared with the American Institute of Physics Handbook Value [76] (Table 3-6). Dilatometry data taken from Appendix A.	121
Figure 3-34	Thermal expansion coefficients, measured by dilatometry on heating, for sintered hydroxyapatite specimens numbers 4-8 and 10-12. Data taken from Appendix A.	123
Figure 3-35	Thermal expansion coefficient data for sintered hydroxyapatite, from cooling dilatometry. The data taken from Appendix A.	124
Figure 3-36	Average thermal expansion coefficient for sintered hydroxyapatite specimens numbers 4-8 and 10-12 (heating to $600^{\circ} \text{C}$ ) as a function of the average grain size. The data was taken from Appendix A.	126

Figure 3-37	Difference in the thermal expansion coefficient for sintered hydroxyapatite, $\Delta = \alpha_{\text{cooling}} - \alpha_{\text{heating}}$ , as a function of temperature. Dilatometry data taken from Appendix A.	127
Figure 3-38	Relative permittivity data from sintered hydroxyapatite and the fitted Maxwell-Garnet equations MGT1 (Equation 1-9) and MGT2 Equation (1-10). The data was taken from Table 3-9.	131
Figure 3-39	Relative permittivity for the sintered hydroxyapatite specimen numbers 14, 16, 33, 41, 42 and the alumina reference material ADS995 as a function of frequency. The data was taken from Appendix B.	132
Figure 3-40	Relative permittivity for sintered hydroxyapatite specimen numbers 43-46, 49 and 50 as a function of frequency. The data was taken from Appendix B.	133

## **1.0 Introduction**

Natural bone is a nano composite of ceramic apatites, principally hydroxyapatite and carbonate apatite, and polymeric collagen fibrils [1]. Interest in the material properties of sintered hydroxyapatite is fueled by hydroxyapatite's applications in structural bio-implants to replace damaged bone. Natural bone, has strength and resilience that is difficult to match artificially. Hydroxyapatite is analogous to the natural ceramic in bone and is bio-active in that hydroxyapatite is non-toxic and an interfacial bond will form between implanted hydroxyapatite and living tissue [1]. Use of this bio-activity in processing mechanically functional components, with hydroxyapatite to interface with the living tissue, requires the study of the material properties of processed hydroxyapatite. The strict requirements for the material properties and quality of bio-implants are due to the high cost of replacement in terms of physical suffering and the medical care resulting from the invasive implant procedure.

### **1.1 Goals of research**

The primary goal of this study is to determine the effect of the microstructure of sintered hydroxyapatite on the mechanical properties of hardness, fracture toughness, and thermal expansion. The effect of the microstructure of sintered hydroxyapatite on the dielectric permittivity is also investigated. An additional goal is to catalog the microstructures of sintered hydroxyapatite produced by compacting and sintering powdered hydroxyapatite.

## 1.2 Chemistry of sintering

Sintering of hydroxyapatite allows formation of dense solid shapes, useful in engineering applications, to be formed from hydroxyapatite powder. Sintering requires mechanical compaction of powder, and firing until diffusion combines individual particles. The compaction and firing process, along with the chemistry and morphology of the starting powder, determines the microstructure of the solid material.

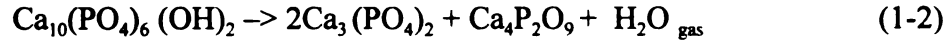
### 1.2.1 Dehydroxylation and decomposition

High temperature sintering of hydroxyapatite (HAP) powders, in air will, depending on the sintering conditions, lead to the thermal decomposition of hydroxyapatite to tricalcium phosphate (TCP) and tetracalcium phosphate (Tet-CP). Thermal decomposition of hydroxyapatite is accomplished in two steps, dehydroxylation and decomposition [2, 3, 4]. The first step, dehydroxylation to oxyhydroxyapatite (OHA) (equation 1-1) is significant at temperatures greater than 800<sup>0</sup> C in air [2, 4, 5, 6].



Dehydroxylation is fully reversible in the presence of water vapor and elevated temperatures as shown by x-ray diffraction [4], thermogravimetric analysis [7], and by proton electrical conductivity [8]. Other experiments have shown that dehydrated hydroxyapatite, a hexagonal apatite called oxyapatite (OAP)  $\text{Ca}_{10}(\text{PO}_4)_6\text{O}\square$  (where  $\square$  denotes a vacancy), undergoes little or no rehydroxylation of oxyapatite at room temperature [4,5,6].

Decomposition to tricalcium phosphate and tetracalcium phosphate occurs at temperatures  $> 1000\text{ }^{\circ}\text{C}$  (equation 1-2) after significant loss of hydroxyl groups [2,3,4].



Decomposition temperature of hydroxyapatite can be lowered significantly by reduction of the water partial pressure in the sintering atmosphere [2,3,4,9,10], lowering the calcium phosphate ratio [2,11,12], and by sintering with particulate additives [10,13].

At temperatures above  $1120^{\circ}\text{C}$ , dehydrated hydroxyapatite decomposes into the  $\alpha$ -form of tricalcium phosphate and tetracalcium phosphate [14].  $\beta$ -tricalcium phosphate formed at lower temperatures will also transform into  $\alpha$ -tricalcium phosphate at temperatures above  $1120^{\circ}\text{C}$ . The  $\alpha$ -form of tricalcium phosphate is metastable at room temperature, the low-temperature  $\beta$ -form of tricalcium phosphate is the stable phase below  $1120^{\circ}\text{C}$  [14].

### **1.2.2 Process control of phase purity during sintering**

Both the dehydroxylation and decomposition reactions, 1-1 and 1-2, have  $\text{H}_2\text{O}$  as a product. The driving force for reactions 1-1 and 1-2 depends, in part, on the partial pressure of  $\text{H}_2\text{O}$  in the furnace. The starting temperatures of the decomposition reaction as a function of water partial pressure are;  $1325^{\circ}\text{C}$ ,  $1426^{\circ}\text{C}$ ,  $1477^{\circ}\text{C}$ ,  $1485^{\circ}\text{C}$ ,  $1520^{\circ}\text{C}$  and  $1565^{\circ}\text{C}$  at water partial pressures of 0.61 kPa, 4.25 kPa, 9.81 kPa, 12.3 kPa, 33.3 kPa and 101.3 kPa, respectively [3].

The Ca/P ratio of a hydroxyapatite powder is an indicator of the high temperature

stability of hydroxyapatite. A thermogravimetric study of stoichiometric hydroxyapatite (Ca/P ratio = 1.67) determined that the hexagonal structure of hydroxyapatite is stable after losing up to 75% of the hydroxyl ions in the form of water [2]. Hydroxyapatite powders, with low Ca/P ratios, show higher rates of decomposition under the same high temperature conditions than do hydroxyapatite powders with Ca/P ratios 1.67 or greater [11]. Experimental data from the literature gives a wide range of secondary phase composition of sintered hydroxyapatite, for a variety of starting powders and sintering conditions (Table 1-1).

### **1.3 Relevant crystal structures**

Crystalline phases of hydroxyapatite (HAP) and HAP decomposition products; tricalcium phosphate and tetra calcium phosphate frequently coexist in the microstructure of the sintered solid body. Interactions between phases effect the material properties of sintered hydroxyapatite solid.

#### **1.3.1 Hydroxyapatite**

Hydroxyapatite is a member of a class of minerals known as apatites, the general apatite formula is  $\text{Ca}_5(\text{PO}_4)_3\text{X}$  where X denotes  $(\text{OH})_2$ ,  $\text{F}_2$ , or  $\text{Cl}$  [15]. Apatites have a hexagonal crystal structure with space group  $\text{P6}_3/\text{m}$  [15,16,17,18]. Hydroxyapatite in the hexagonal (apatitic) structure,  $\text{P6}_3/\text{m}$  has room temperature lattice parameters  $a_0 = 0.9423$  nm, and  $c_0 = 0.6875$  nm [18]. The theoretical density of hydroxyapatite is  $3.156$  g/cm<sup>3</sup> [15].

Under a strict calcium phosphate ratio of Ca/P = 1.67, high purity hydroxyapatite

Table 1-1 A survey of secondary phase formation in sintered hydroxyapatite, under varied sintering conditions from the literature.

Starting Powder	Temperature (°C)	Time (min)	Atmosphere	$\alpha$ - TCP	$\beta$ - TCP	Tetra-TCP	Reference
Solution grown	1050-1350	180	Air	0	0	0	[19]
Solution grown	1450	180	Air	Trace	0	0	[19]
Filter Cake	1150-1300	180	Air	0	0	0	[20]
Filter Cake	800-1000	120	HIP in Air	0	0	0	[21]
Comm.*	1200	60	Air	0	0	0	[10]
Comm.*	120	60	Moisture	0	0	0	[10]
ppt.**	1200	600	Air	0	0	0	[22]
HAP whiskers	1150	1	Microwave in air	Trace	0	0	[23]
HAP	1200	1	Microwave in air	0	0	0	[23]
ppt.**	1100	240	air	0	Trace	0	[9]
ppt.**	1300	240	air	0	Trace	Trace	[9]
ppt.**	1350	240	air	Trace	Trace	Trace	[9]
ppt.**	1100-1300	240	Vacuum	Trace	-----	Trace	[9]
Ca/P =1.55	1250	120	air	10%	75%	n/a	[11]
Ca/P =1.61	1250	120	air	5%	35%	n/a	[11]
Ca/P =1.64	1250	120	air	3%	0	n/a	[11]
Ca/P =1.67	1250	120	air	0	0	0	[11]
Ca/P =1.73	1250	120	air	0	0	0	[11]

\*- Commercial powder

\*\* - Precipitate from solution.

precipitates into a monoclinic structure with space group  $P2_1/b$  [24,25,26]. Room temperature hydroxyapatite monoclinic ( $P2_1/b$ ) lattice parameters are;  $a_0 = 0.94214$  nm,  $b_0 = 2a_0$ ,  $c_0 = 0.68814$  nm and  $\gamma = 120^\circ$  [24]. Monoclinic hydroxyapatite has been prepared hydrothermally [25], by a dry method [27], and by heating a single crystal of chloroapatite to  $1200^\circ\text{C}$  in steam [24].

A fully reversible phase change from the monoclinic structure to the hexagonal structure has been shown by disappearance of birefringence at  $211.5^\circ\text{C}$  [25], dielectric measurements at  $207^\circ\text{C}$  [26], x-ray diffraction analysis and differential scanning calorimetry, with transition temperature between  $200^\circ\text{C}$  and  $210^\circ\text{C}$  [27]. The subsequent discussion of hydroxyapatite, in this thesis, assumes the hexagonal crystalline structure, unless specifically noted otherwise.

Thermal expansion coefficients along the crystallographic axes, of hydroxyapatite, reported in the literature include:  $\alpha(a_0) = 13.6 \times 10^{-6} /^\circ\text{C}$ ,  $\alpha(c_0) = 12.6 \times 10^{-6} /^\circ\text{C}$ , varying linearly with temperature from room temperature to  $850^\circ\text{C}$  Trombe et al. [4];  $\alpha(a_0) = 13.1 \times 10^{-6} /^\circ\text{C}$ ,  $\alpha(c_0) = 21.7 \times 10^{-6} /^\circ\text{C}$ , from  $22^\circ\text{C}$  to  $1002^\circ\text{C}$  Fischer et al. [28]; and  $\alpha(a_0) = 12.2 \times 10^{-6} /^\circ\text{C}$ , and  $\alpha(c_0) = 11.5 \times 10^{-6} /^\circ\text{C}$  from  $20^\circ\text{C}$  to  $576^\circ\text{C}$  Perdok et al. [29]. The difference ( $\Delta\alpha$ ) in the coefficient of thermal expansion along the crystallographic axes  $a_0$  and  $c_0$ , from the three studies are varied:  $\Delta\alpha = 1.0 \times 10^{-6} /^\circ\text{C}$  [4],  $7.4 \times 10^{-6} /^\circ\text{C}$  [28],  $0.7 \times 10^{-6} /^\circ\text{C}$  [29].

Room temperature x-ray diffraction studies of sintered hydroxyapatite reveal the shrinking of the lattice parameter  $a_0$  as a function of sintering temperature. Lattice parameter  $a_0$  decreases from  $0.9416$  nm, for sintering at  $900^\circ\text{C}$ , to  $0.9411$  nm, for sintering at  $1450^\circ\text{C}$  [19], and  $a_0 = 0.9428$  nm, for sintering at  $1050^\circ\text{C}$  and  $a_0$  decreases to

below 0.9425 nm for sintering at 1250° C [7]. The lattice parameter  $a_0$  reduction is due to the loss of (OH<sup>-</sup>) [7,19].

The hydroxyapatite used by Trombe et al. [4] for crystallographic thermal expansion measurements was synthesized from tricalcium phosphate and calcium carbonate by heating for approximately one month at 1000° C-1100° C in a nitrogen/water vapor atmosphere. The hydroxyapatite material used in the study by Fischer et al.[28] was extensively heat treated at 1200° C for 4 hours before x-ray analysis of the crystallographic thermal expansion coefficients. Perdok et al. [29] prepared stoichiometric (Ca/P ratio =  $1.659 \pm 0.03$ ) hydroxyapatite crystals at 70° C. The differences in the concentration of thermal vacancies between the hydroxyapatite formed in the three studies may explain the variance in the thermal expansion along the crystallographic axes [29].

For a hexagonal crystal structure equation 1-3 is used to calculate the average linear thermal expansion coefficient ( $\alpha$ ) from the measured crystallographic thermal expansion coefficients.

$$\alpha = [2\alpha(a_0) + \alpha(c_0)] / 3 \quad (1-3)$$

The average linear thermal expansion coefficient for polycrystalline hydroxyapatite calculated from the above lattice thermal expansion data are:  $13.24 \times 10^{-6} / ^\circ\text{C}$  [4],  $15.97 \times 10^{-6} / ^\circ\text{C}$  [28], and  $11.95 \times 10^{-6} / ^\circ\text{C}$  [29].

Jarcho et al. recorded  $11 \times 10^{-6} / ^\circ\text{C}$  for the average linear thermal expansion coefficient for hydroxyapatite, at temperatures between 25° C to 225° C [30], the average linear thermal expansion coefficient for hydroxyapatite measured by dilatometry, by Choi et al. equals  $16.9 \times 10^{-6} / ^\circ\text{C}$  [31].

### 1.3.2 Tricalcium phosphate

The high temperature  $\alpha$ -tricalcium phosphate crystallizes in a monoclinic structure with space group  $P2_1/a$ , and room temperature lattice parameters  $a_o = 1.2887$  nm, and  $b_o = 2.7280$ ,  $c_o = 1.5219$  nm, with  $\beta = 126.20^\circ$ [32]. The theoretical density for  $\alpha$  -tricalcium phosphate is  $2.863$  g/cm<sup>3</sup>[32].

The  $\beta$ -form of tricalcium phosphate is a rhombohedral with space group  $R3c$ , room temperature lattice parameters  $a_o = 1.0439$  nm, and  $c_o = 3.7375$  nm [33]. The theoretical density for  $\beta$  -tricalcium phosphate is  $3.067$  g/cm<sup>3</sup> [33].

### 1.3.3 Tetracalcium phosphate

Tetracalcium phosphate has a monoclinic crystal structure with space group  $P2_1$ . Room temperature lattice parameters are  $a_o = 0.7023$  nm, and  $b_o = 1.1986$ ,  $c_o = 0.9473$  nm, with  $\beta = 90.90^\circ$ [34]. Theoretical density for tetracalcium phosphate is  $3.051$  g/cm<sup>3</sup> [34].

## 1.4 Microstructure of sintered hydroxyapatite

The microstructure of sintered hydroxyapatite consists, in part, of directly measurable characteristics as porosity, grain size, impurity levels, and the presence of secondary phases. The porosity, grain size, impurity levels, and secondary phase relationships are controlled to engineer the processing of hydroxyapatite. Other microstructural features that can only be measured indirectly include residual stress levels in grains and microcracking between the grains. Interactions between different solid phases and pores are also integral to the description of the sintered microstructure of a

solid body.

#### 1.4.1 Residual strain energy and microcracking

Thermal expansion mismatch between phases and thermal expansion anisotropy among individual grains create microstresses in sintered ceramics during cooling from the sintering temperature [35]. Stresses induced by thermal expansion mismatch and thermal expansion anisotropy may generate internal microcracks between grains in brittle materials [35]. A microcrack is a separation between grains with a large aspect ratio (length to width ratio). Anisotropic crystals exhibit thermal expansion anisotropy in which the thermal expansion varies along different crystallographic axes [35]. Thermal expansion anisotropy of hydroxyapatite has been measured directly with varying results (section 1.3.1). The decomposition products of hydroxyapatite are all noncubic and exhibit some degree of thermal expansion anisotropy (TEA).

The maximum elastic strain energy  $U_{st}$  stored in a single grain in a material subject to thermal expansion mismatch or TEA may be expressed as equation 1-4 [36].

$$U_{st} = 1/8( E \Delta T^2 \Delta\alpha_{max}^2 ) \quad (1-4)$$

where the maximum thermal expansion difference between two adjacent grains is  $\Delta\alpha_{max}$ , the modulus of elasticity is E, and the temperature change is  $\Delta T$ .

Equation 1-5 is an energy criterion for microcracking which relates grain size, grain geometries, material properties, and thermal history and is written in terms of the maximum strain energy, equation 1-4, and a critical grain size,  $g_{cr}$  [36]:

$$g_{cr} = k \gamma_f / E(\Delta T^2 \Delta \alpha_{max}^2) \quad (1-5)$$

where  $k$  is a constant based on the grain's geometry and  $\gamma_f$  is the fracture surface energy.

The quantities  $E$ ,  $\Delta T$ , and  $\Delta \alpha$  are as defined following equation 1-4.

The  $\alpha$  to  $\beta$  tricalcium phosphate transformation results in a 6.7% volume decrease which contributes strain energy to the sintered solid body [32,33]. The magnitude of the strain energy for  $\beta$  tricalcium phosphate grains transformed in a hydroxyapatite matrix is a function of grain volume and the quantity and distribution of  $\beta$  tricalcium phosphate crystals [7,9].

## **1.5 Microstructure and mechanical properties**

### **1.5.1 Indentation hardness**

Vickers indentation hardness is measured by the size of the permanent deformation of the surface of the tested material and the load required to produce the impression (Figure 1-1). Vickers indentation hardness can qualitatively measure the relationships between plastic deformation mechanisms, such as slip and twinning found in alumina at room temperature [37], and microstructure.

### **1.5.2 Indentation method to determine fracture toughness**

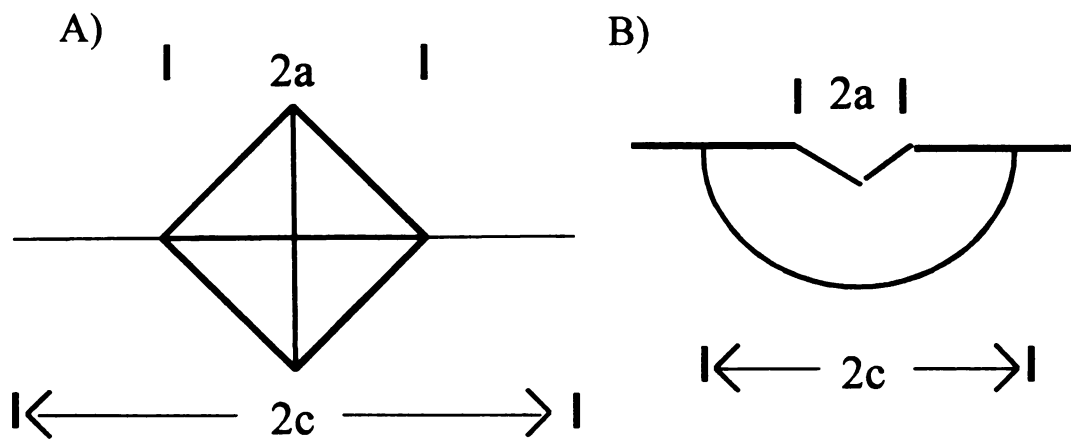
Fracture toughness is a measure of a materials resistance to crack growth [35]. Lawn and Wilshaw [38] reviewed the principles of indentation fracture and considered the applications to fracture toughness evaluation. Due to the complex indentation stress field considerable uncertainties exist in the absolute fracture parameters. However,

determinations of the relative fracture toughness for a material can be determined with an accuracy that is comparable to most other fracture techniques [38].

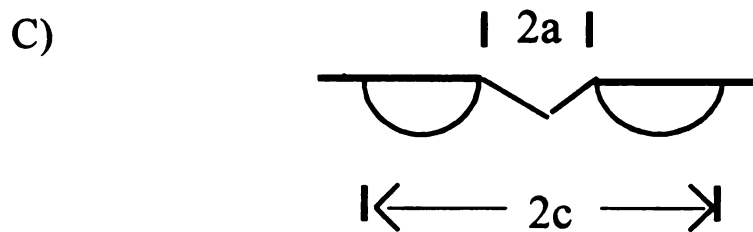
For indentation fracture toughness measurements sharp indenters create an intense elastic stress field about the point of indentation [38]. Shear and hydrostatic compression near the indenter point account for the residual impression and microfracture initiation [38]. Subsequent cracking is caused by tensile stress acting on the initial microfracture [38]. Toughness is measured by the extent of the subsequent cracking[38].

Evans and Charles [39] did a pioneering study of ceramic materials with a large range of hardness, toughness and Poisson's ratios. Evans and Charles compared fracture toughness values ( $K_{Ic}$ ) determined by the double torsion technique with the Vickers indentation parameter ( $c/a$ ), where  $c$  is the indentation crack length and  $a$  is the Vickers indent diagonal[39]. A relationship between  $(K_{Ic} \Phi) / (H \sqrt{a} [H/\Phi E]^{0.4})$  and  $(c/a)$  was found for well behaved half penny cracks created by Vickers indentation, (Figure 1-1), where  $\Phi$  is a constraint factor,  $H$  is Vickers Hardness (Pa), and  $E$  is the elastic modulus (Pa).

Anstis et al. [40] further quantified the indentation toughness technique using fracture toughness data from traditional techniques (double torsion and double cantilever bend) compiled from a variety of ceramics with a large range of hardness, toughness and elastic modulus. Comparing toughness data measured by double torsion and double cantilever bend methods to Vickers indentation parameters leads to an equation for the fracture toughness as a function of the Vickers indentation crack length in which accuracy better than 30-40% is readily attainable (Equation 1-6) [40].



Vickers Indentation and fully developed half penny cracks



Vickers Indentation and Palmqvist cracks

Figure 1-1 Vickers indentation impression and the characteristic dimensions used in the hardness calculation and the toughness equation (Equation 1-6), A) top view left and B) side view. A schematic of the side view of representative Palmqvist cracks is given in C) [42].

$$K_c = \zeta \left( \frac{E}{H_v} \right)^{1/2} \frac{P}{c^{3/2}} \quad (1-6)$$

where  $H_v$  is Vickers Hardness,  $E$  is the elastic modulus,  $P$  is the indentation load and indentation crack length is  $c$ . The value of the non-dimensional empirically determined constant  $\zeta$  is equal to  $0.016 \pm 0.004$  [40]. Other researchers [41,42] have successfully extended the Evans and Charles/Anstis model to the low load regime where Palmqvist cracks (Figure 1-1) are encountered.

### 1.5.3 Hardness and fracture toughness studies

Hardness and fracture toughness measurements of sintered ceramics have been used to determine the influence of microstructural features such as grain size, porosity, crystallographic phase changes, grain morphology, degree of crystallinity in glass ceramics, and the elastic and plastic anisotropy.

The inverse trend of hardness as a function of grain size (g.s) ( $H_v \propto [\text{g.s}]^{-1/2}$ ) for a variety of dense oxide and non-oxide materials has been studied by Rice et al. [43]. Several ceramic materials show a distinct Vickers hardness ( $H_v$ ) dependence on grain size[43]. A 10 fold increase in grain sizes produces; ~70% decrease in Vickers hardness ( $H_v$ ) for MgO, ~30% decrease in  $H_v$  for BeO, ~10% decrease in  $H_v$  for  $\text{Al}_2\text{O}_3$ , and a ~5% decrease in  $H_v$  for  $\text{MgAl}_2\text{O}_4$  and  $\text{B}_4\text{C}$ [43].  $\text{ZrO}_2$  shows very little grain size dependence on  $H_v$  over the grain size range  $0.5 \mu\text{m}$  to  $50 \mu\text{m}$ [43]. Other materials such as  $\text{TiB}_2$ , SiC, TiC and  $\text{Si}_3\text{N}_4$  show little effect of a grain size hardness relationship over the grain size ranges studied ( $10 \mu\text{m}$ - $140 \mu\text{m}$  for  $\text{TiB}_2$  and SiC,  $20 \mu\text{m}$ - $140 \mu\text{m}$  for TiC and  $\text{Si}_3\text{N}_4$ )[43].

Krell et al. [44] investigated the hardness versus grain size relationships of high purity sintered alumina of 99.2% relative density. High purity submicron alumina powder (Taimicron-DAR) was used to sinter six specimens, with grain sizes ranging from 0.4  $\mu\text{m}$  to 4  $\mu\text{m}$ , to 99.2%  $\pm$ 0.4% relative density [44]. Vickers hardness testing (10 N load) measured a continuous decrease in Vickers hardness as the grain size increased ( $H_v = 22$  GPa at grain size = 0.4  $\mu\text{m}$  to  $H_v = 15$  GPa at grain size = 4  $\mu\text{m}$ [44]). The increase in hardness as the grain size decreased for sintered alumina was attributed to the reduction of dislocation mobility as the grain size decreases [44].

Hardness and toughness measurements of sintered  $\text{Y}_2\text{O}_3$ , processed by either hot isostatic pressing (HIP) or vacuum sintering (VS), were compared using indentation hardness techniques with indentation loads ranging from 25-200 N [45]. Microstructural comparison showed that HIPed  $\text{Y}_2\text{O}_3$  was denser than vacuum sintered  $\text{Y}_2\text{O}_3$  (99.7% versus 98.8% theoretical density) with HIPed  $\text{Y}_2\text{O}_3$  having much smaller average grain size than vacuum sintered  $\text{Y}_2\text{O}_3$  (0.7  $\mu\text{m}$  --HIP versus 15  $\mu\text{m}$  --vacuum sintered) [45]. HIP  $\text{Y}_2\text{O}_3$  was ~16% harder than vacuum sintered  $\text{Y}_2\text{O}_3$  ( $H_v = 7-7.5$  GPa --HIPed  $\text{Y}_2\text{O}_3$  versus 6-6.5 GPa --vacuum sintered  $\text{Y}_2\text{O}_3$  [45]). Direct crack measurements of the Vickers indentation cracks (indentation toughness technique) of HIP and vacuum sintered  $\text{Y}_2\text{O}_3$  were used to calculate fracture toughness. The calculated fracture toughness of HIPed  $\text{Y}_2\text{O}_3$  was ~9% greater than vacuum sintered  $\text{Y}_2\text{O}_3$  [45].

Nano indentation of nano crystalline ZnO and nano phase  $\text{TiO}_2$  shows a decrease in hardness as the porosity of the specimen increases [46,47]. Nano-crystalline ZnO and nano-phase  $\text{TiO}_2$  exhibited an almost linear increase in hardness as a function of sintering temperature, regardless of the grain sizes[46,47]. The average grain sizes for nanophase

TiO<sub>2</sub> were estimated from previous sintering studies of nanophase TiO<sub>2</sub> from 12 nm as compacted (no sintering) to 243 nm for TiO<sub>2</sub> sintered at 900° C [47]. The average grain sizes for ZnO is 7.4 nm (unsintered) to 140 nm for ZnO sintered at 700° C, determined by dark field TEM [46]. Relative densities of TiO<sub>2</sub> were estimated from previous sintering studies of nanophase TiO<sub>2</sub> and increase with increasing sintering temperatures. Relative density equals ~ 75% for the as compacted TiO<sub>2</sub> and reaches a maximum of ~ 90% at 900° C [47]. The relative density of nanocrystalline ZnO, estimated from elastic modulus measurements, increased as the sintering temperature increased, for specimens sintered at the maximum temperature of 900° C the relative density was estimated to be 90-95% [46]. Hardness decreases as porosity increases from 1.8 GPa at 15% relative porosity to 4.0 GPa at 5 - 10% relative porosity for ZnO [46] and from 1.3 GPa at 25% relative porosity to 9.0 GPa at 10% relative porosity for TiO<sub>2</sub> [47].

Indentation hardness and indentation toughness measurements of calcium-modified lead titanate ceramics show the influence of porosity, grain size and tetragonal distortion [48]. Calcium-modified lead titanate specimens were sintered with relative porosities ranging 2% to 30%, grain sizes between 2.4 μm to 6.0 μm, and three Ca/Pb ratios; 24/76, 26/74, and 35/65. Hardness decreased as porosity increased, from 3.3 GPa at 4-7% relative porosity to 2.3 GPa at 17.5% relative porosity for specimens with Ca/Pb ratio of 26/74, regardless of grain size (2.99-5.95 μm) [48]. The slopes of the hardness versus porosity curves were significantly different for the different Pb/Ca ratios signifying the effect of tetragonal distortion [48].

The quantity, morphology and distribution of fluorine containing mica embedded in a glass matrix influenced the hardness of a glass ceramic composite, due to the weakly

bonded cleavage planes of the mica [49]. Vickers hardness decreased as the mica crystals increased in number and the aspect ratio increases [49]. A precipitous decline in hardness is measured as the growth of mica crystals caused them to interlock [49].

Elastic and plastic anisotropy of highly textured  $(\text{Bi, Pb})_2\text{Sr}_2\text{Ca}_2\text{Cu}_3\text{O}_x$  superconductor has been studied by indentation hardness measurements as a function of the relative orientation of the indent [50]. Maximum hardness ( $H_v = 45\text{-}50\text{ MPa}$ ) is measured when the Vickers indent diagonal is parallel to the grain texture and a minimum hardness ( $H_v = 35\text{-}40\text{ MPa}$ ) is measured when the indent diagonal is 45 degrees off of the grain texture [50].

The fracture toughness of dense  $\beta\text{ Si}_2\text{N}_4$  ( $98.9\% \pm 0.2\%$  relative density) measured by the single-edge precracked beam (SEPB) method, is a function of the grain size and morphology [51]. Intermediate sintering times (4 hours at  $2000^\circ\text{C}$ ) for  $\beta\text{ Si}_2\text{N}_4$  produces an optimal number and distribution of large grains (2-20  $\mu\text{m}$  diameter and 10-300  $\mu\text{m}$  in length), in a matrix of small grains (0.2-2  $\mu\text{m}$  diameter and 1-5  $\mu\text{m}$  long) to produce the greatest fracture toughness ( $K_{\text{IC}} = 10.3\text{ MPa m}^{1/2}$ )[51]. Specimens sintered for 2 hours at  $2000^\circ\text{C}$  had a microstructure with fewer large grains distributed evenly in the matrix of small grains and measured the lowest fracture toughness ( $K_{\text{IC}} = 8.5\text{ MPa m}^{1/2}$ )[51]. Specimens sintered for 8 hours at  $2000^\circ\text{C}$  exhibited an increase in the number and clustering of large grains which decreased the measured fracture toughness to  $K_{\text{IC}} = 8.8\text{ MPa m}^{1/2}$  possibly due to an increase in microcrack density [51].

#### **1.5.4 Fracture energy and microstructure**

In studying the apparent fracture energy  $\gamma$  as a function of flaw size Rice et al [52]

found that ceramics with microstresses exhibit a significant decrease in the apparent fracture energy as the flaw sizes decrease to the scale of the intergranular microstresses (i.e. grain size) [52]. Microstresses are defined to be stresses between neighboring grains and are due to thermal expansion anisotropy (TEA), volumetric phase changes and thermal expansion mismatch between phases. As the grain size increases the critical flaw size increases and the apparent fracture energy decreases. Since the fracture energy  $\gamma$  is related to fracture toughness by  $K_{Ic} = (E \gamma)^{1/2}$  [53] the fracture toughness decreases for materials with microstresses between grains as the grain size increases [52,53].

A review of fracture energy data for several dense ceramics [53] showed a pronounced maxima in the fracture energy versus grain size relationship with a subsequent substantial decrease in fracture energy as the grain size increased further. The maxima in fracture energy at a particular grain size, were most pronounced in non-cubic materials such as  $Al_2O_3$  at  $\sim 80 \mu m$ ,  $TiO_2$  at  $\sim 16 \mu m$  and  $Nb_2O_5$  at  $\sim 6 \mu m$  [53]. The maxima in the fracture energy and the continued decrease in fracture energy as the grain size increased beyond the critical values has been correlated with the onset of microcracking by other measurements, including the elastic modulus as a function of grain size [53].

### **1.5.5 Indentation studies of sintered hydroxyapatite**

Vickers hardness values, from Kijima et al. [19] (indentation load 0.98 N), for monophase, dehydrated hydroxyapatite (OHAP) ranged between 6.3 GPa and 6.5 GPa for specimens with grain sizes between 1.6  $\mu m$  and 6.5  $\mu m$  and a narrow range of density (99.0-99.4% theoretical density).

A steady increase in the fracture toughness, measured by three point bend test, as a

function of density is recorded for sintered hydroxyapatite made from a commercial powder (Merck A.G.) [54]. The fracture toughness values ranged from  $K_{IC} = 0.6 \text{ MPa m}^{1/2}$  at ~73% theoretical density to  $K_{IC} = 1.0 \text{ MPa m}^{1/2}$  at ~97% theoretical density [54]. As the sintering temperature increased the density, grain size and amount of HAP decomposition increased [54]. Tricalcium phosphate was detected, by x-ray diffraction, for the four densest specimens sintered at temperatures greater than  $1150^\circ \text{C}$  (out of six total specimens) [54]. The average grain size of the sintered hydroxyapatite ranges from  $1.7 \mu\text{m}$  to  $4 \mu\text{m}$  [54].

The Knoop Hardness (1.96 N load) of pure and partially decomposed HAP increased as the density increased for all specimens [9]. The polyphase material (partially decomposed to  $\alpha$ -tricalcium phosphate and tetra-calcium phosphate) exhibited significantly greater hardness as a function of density [9]. HAP sintered to 78% relative density yielded a Knoop hardness of  $H_k = 2.04 \text{ GPa}$  for decomposed HAP versus  $H_k = 1.03 \text{ GPa}$  for monophase HAP [9]. HAP sintered to 76% relative density exhibited a Knoop hardness of  $H_k = 1.63 \text{ GPa}$  for the decomposed HAP versus  $H_k = 0.93 \text{ GPa}$  for monophase HAP [9]. The grain size was  $90 \mu\text{m}$  for the HAP specimen sintered in air at  $1200^\circ \text{C}$  to 77.6% relative density [9].

The effect of decomposition on the hardness of the sintered hydroxyapatite specimens shown by Wang et al. [9] was explored further by Slosarczyk et al. [11]. The phase composition and Knoop hardness (indentation load not reported) of sintered hydroxyapatite prepared from powders with different Ca/P ratios (Table 1-1) was measured [11]. Hydroxyapatite specimens (of similar density  $3.06 \text{ g/cm}^3$  to  $3.11 \text{ g/cm}^3$ , and a grain size range of  $6\text{-}8 \mu\text{m}$ ) exhibited Knoop hardness values of  $H_k = 4.9 \text{ GPa}$  (40%

TCP, 60% OHAP),  $H_k$  4.6 GPa (85% TCP, 15% OHAP) and finally  $H_k = 4.2$  GPa for hydroxyapatite specimens composed of 3% TCP, 97% OHAP [11]. Monophase dehydrated hydroxyapatite specimens gave a Knoop hardness of  $H_k = 2.7$  GPa (2.89 g/cm<sup>3</sup>),  $H_k = 4.0$  GPa (3.10 g/cm<sup>3</sup>) with a maximum Knoop hardness  $H_k = 4.6$  GPa at a density of 3.12 g/cm<sup>3</sup> [11]. The theoretical densities of the decomposition phases ( $\alpha$  TCP = 2.863 g/cm<sup>3</sup> and  $\beta$  TCP = 3.067 g/cm<sup>3</sup>) are 3-9% lower than monophase hydroxyapatite (HAP = 3.156 g/cm<sup>3</sup>). The actual relative density of the polyphase sintered specimen will depend on the percentage of decomposition phases present.

Fracture toughness, measured by the single edge notched bend technique (SENB), was shown to be a function of grain size for submicron hot pressed hydroxyapatite specimens [55]. HAP was hot pressed in an argon atmosphere from 1100 C to 1250<sup>o</sup> C to 98.8% to 99.5% relative density and with grain sizes from 0.2  $\mu$ m (hot pressed at 1100<sup>o</sup> C for 30 minutes) to 1.2  $\mu$ m (hot pressed at 1250<sup>o</sup> C for 600 minutes) [55]. Fracture toughness as a function of grain size peaked at 0.4  $\mu$ m average grain size  $K_{IC} = 1.2$  MPa m<sup>1/2</sup> dropping to  $K_{IC} < 1.0$  MPa m<sup>1/2</sup> at 1.2  $\mu$ m average grain size [55].

Three-point bend fracture strength measurements on the hot pressed HAP, by Halouni et al. [55] displayed a more significant peak of the fracture strength as a function of grain size compared to the fracture toughness peak. The fracture toughness and fracture strength peaks were at the same grain size [55]. The fracture strength  $\sigma_f = 137$  MPa, at 0.4  $\mu$ m average grain size, decreased to  $\sigma_f = 99$  MPa at 1.2  $\mu$ m average grain size [55]. Maximums in fracture toughness and fracture strength as a function of grain size were attributed to the start of microcracking at the critical grain size, due to thermal expansion anisotropy [55]. There was no attempt to determine the presence of

decomposition phases in the hot pressed hydroxyapatite [55].

The fracture toughness as a function of processing methods and reinforcing whisker content was determined by Suchanek et al. [56], for hydroxyapatite whiskers in a hydroxyapatite matrix. Fine grained elongated hydroxyapatite powder (grain size 20-50 nm diameter 100-300 nm in length) were reinforced with 0-30% hydroxyapatite whiskers (whiskers of 1-4  $\mu\text{m}$  diameter with aspect ratio of 5-35, average aspect ratio = 15). The HAP powder and HAP whiskers were mixed, pressed into pellets and sintered via three methods; pressure-less sintering, hot pressed sintering and HIP sintering. Hot pressing and HIP sintering were done in an argon atmosphere and lead to traces (< 5%) of decomposition product  $\beta$ -TCP [56]. The fracture toughness of HAP/(HAP 0-30% whisker) composites, decreased exponentially as the porosity increased regardless of the processing method and whisker content [56]. Maximum fracture toughness values ( $K_{\text{IC}} = 1.4\text{-}2.0 \text{ MPa m}^{1/2}$ ) were achieved by hot isostatic pressed HAP/(HAP whisker) composites with maximum densities (97% to 99.9% relative density) and whisker contents between 20% and 30% [56]. Hot pressed HAP/(HAP whisker) composites exhibited fracture toughness of  $K_{\text{IC}} = 1.35\text{-}1.41 \text{ MPa m}^{1/2}$  for HAP/(HAP10-30% whisker) composites with 92.5-97% relative density [56]. HAP/(HAP 10% whisker) composites were pressure-less sintered to 71% to 90% relative density and the resultant fracture toughness values ranged from  $K_{\text{IC}} = 0.8 \text{ MPa m}^{1/2}$  (71% relative density) to  $K_{\text{IC}} = 1.1 \text{ MPa m}^{1/2}$  (90% relative density) [56].

HAP/(HAP whisker) composites, produced by Suchanek et al [56], had higher fracture toughness values, as a function of density, than unreinforced (0% whiskers) HAP. Hot pressed unreinforced HAP (0%whiskers) exhibited fracture toughness of  $K_{\text{IC}} = 1.04$

MPa m<sup>1/2</sup> at 97% relative density, which increased to  $K_{IC} = 1.35-1.41$  MPa m<sup>1/2</sup> for HAP/(HAP 10-30% whisker) composites (92.5-97% relative density) [56].

## **1.5.6 Summary of hardness and toughness studies**

### **1.5.6.1 Hardness**

Hardness increases as the grain size decreases, for many sintered ceramics [43,44,45]. The hardness of sintered hydroxyapatite is typically unaffected over a grain size range of 1.6-6.5  $\mu\text{m}$  [19] and obscured by porosity and the presence of decomposition phases [9,11].

Secondary phases in a sintered ceramic have been shown to significantly influence the hardness. A large decrease in hardness was measured as the amount of mica increased in a glass ceramic, a further decrease in hardness can be attributed to the morphology of mica [49]. Decomposition phases in sintered hydroxyapatite increased the hardness significantly [9,11].

Porosity is the most significant factor in determining the hardness of sintered ceramics. Hardness decreases as porosity increases in ZnO and TiO<sub>2</sub> [46,47], calcium modified lead titanate [48] and hydroxyapatite [9,11].

### **1.5.6.2 Fracture toughness**

There is a complex relationship between the grain size and the fracture toughness of sintered ceramics. As the grain size increases for sintered ceramics the fracture toughness decreases slightly [48] or increases slightly [45]. For other ceramics the

fracture toughness reaches a maxima at a critical grain size then decreases significantly at larger grain sizes [53,55]. The grain size versus toughness relationship, with a maxima at the critical grain size, is related to microstresses between grains and microcracking [53,55]. For Halouni et al. [55], however, no effort was made to detect the presence of the decomposition of hydroxyapatite when the specimens were sintered in a moisture free atmosphere. The fracture toughness was compared to grain size and as the grain size increases, due to the increasing sintering temperature, the likelihood of the decomposition of hydroxyapatite, in an argon environment, increases [55].

The presence of secondary phases does not seem to influence the fracture toughness of sintered hydroxyapatite compared to the microstructural features of porosity and grain size [54], or porosity and whisker reinforcement [56].

Porosity influences the fracture toughness of sintered ceramics various ways. Fracture toughness increased as porosity increased for calcium modified lead titanate ceramics [48]. Decreasing fracture toughness with increasing porosity was determined for hydroxyapatite regardless of secondary phase composition [54] and regardless of the whisker reinforcement and the presence of secondary phases [56].

## **1.6 Material properties and porosity and the minimum solid area model**

For a wide variety of materials the porosity dependence of hardness, fracture toughness, elastic modulus, flexural strength, compressive strength and electrical and thermal conductivity have been successfully modeled by a minimum solid area model (MSA) [57,58] derived from the minimum solid area ratios. The minimum solid area ratios were calculated from (1) the idealized stacking of solid spheres, (2) idealized

stacking of cylindrical or spherical pores in a solid matrix, and (3) combinations of (1) and (2), as a function of volume fraction porosity[57]. The minimum solid area model relates the material property value of a porous material in relation to the fully dense property value [57] (Equation 1-7).

$$A = A_0 e^{-bP} \quad (1-7)$$

where A is the material property of the porous material,  $A_0$  is the material property of the fully dense material, b is a constant derived from the stacking arrangements. Equation 1-7 can be linearized (Equation 1-8).

$$\ln(A) = \ln(A_0) - bP \quad (1-8)$$

where b is the slope of the plot of the logarithm of material property (A) versus the volume fraction porosity (P).

For all possible stacking arrangements of particle and pore used in the MSA model, there exists a critical volume fraction porosity ( $P_c$ ) at which the bond area between pores goes to zero. Hence physical properties drop precipitously to zero for volume fraction porosities greater than the critical volume fraction porosity ( $P_c$ ) and Equation 1-7 no longer holds [57].  $P_c$  lies between 0.2 and 0.7 [57]. The minimum solid area model predicts continuous decreases in the physical properties of hardness, and fracture toughness as porosity increases for materials.

Fracture toughness depends less on porosity than do hardness and elastic modulus

[53]. In some cases an increase in fracture toughness with increasing porosity at low porosity (< 15 volume percent) occurs or there is little or no change in fracture toughness at low and moderate porosity ranges (up to 15 volume percent porosity respectively) [53]. In contrast, strength and elastic modulus decrease continuously as in porosity increases [53]. Fracture toughness is less sensitive to changes in porosity than is hardness, which appears to be associated with either crack bridging between pores or with the interaction between porosity and the test method [53].

### 1.7 Thermal expansion and microstructure

A study of several ceramic oxides by Nielson and Leipold [59] found the bulk coefficient of thermal expansion, measured up to 2200° C in air, was unaffected by the microstructural features of porosity and grain size (Table 1-2). Coble and Kingery [60] studied the physical properties of single grain size sintered alumina with variable porosity. The bulk thermal expansion coefficient, from 25° C to 1200° C, of sintered alumina was found to be independent of porosity over a wide range of porosity (Table 1-2) [60].

Table 1-2 Ceramic oxides in which the bulk thermal expansion coefficient was constant for a variety of grain sizes and porosity.

Oxide	Porosity (%)	Grain Size Range (μm)	Reference
Al <sub>2</sub> O <sub>3</sub>	4-49%	23 μm*	[60]
Al <sub>2</sub> O <sub>3</sub>	2-8%	3-66 μm	[59]
MgO·Al <sub>2</sub> O <sub>3</sub>	2-9%	36-53 μm	[59]
MgO	2-9%	4-161 μm	[59]
CaO	2-4%	12-111 μm	[59]

\* Single grain size for the entire porosity range.

### **1.7.1 Thermal expansion and microcracking**

A polycrystalline solid that contains microcracks exhibits two characteristic features in thermal expansion analysis; (1) near room temperature, the thermal expansion of microcracked materials is lower than the thermal expansion of non-microcracked material, and (2) a large hysteresis in the thermal expansion versus temperature curve between the heating data and the cooling data from a microcracked specimen [61,62,63]. Both features (1) and (2) have been experimentally documented using dilatometry for  $\text{Nb}_2\text{O}_5$  [61],  $\text{MgTi}_2\text{O}_5$  [62] and aluminum titanate materials [63].

Thermal expansion hysteresis between the heating and cooling curves in dilatometry studies of sintered ceramics results from microcrack healing at elevated temperatures as the temperature increases [64]. The microcracks re-open as the temperature decreases, due to thermal expansion anisotropy and/or thermal expansion mismatch [64]. The low values of expansion at room temperature are due to expansion of grains into the microcracks, limiting overall specimen dilation [61].

### **1.8 Dielectric properties and microstructure**

The relative dielectric permittivity of a polycrystalline polyphase ceramic is dependent on the porosity and phase mixture of the solid [35]. The Maxwell-Garnet theory (MGT) is a commonly used mixing rule derived for spherical inclusions within a host matrix [65]. The MGT, included in a study by Calame et al. [65], can be written as equation 1-9 (MGT1). Equation 1-9 gives the relative dielectric permittivity of a mixture of spherical pores in a ceramic host matrix as a function of the relative volume density of the ceramic. When air is considered to be the host matrix with additions of spherical

ceramic inclusions, the MGT results in equation MGT2 (Equation 1-10).

$$k_m = \frac{k_{cer} [3 - 2R + 2Rk_{cer}]}{[R + k_{cer} (3 - R)]} \quad \text{MGT1} \quad (1-9)$$

$$k_m = \frac{[k_{cer} (1 + 2R) + 2(1 - R)]}{[k_{cer} (1 - R) + (2 + R)]} \quad \text{MGT2} \quad (1-10)$$

where  $k_m$  and  $k_{cer}$  are the relative dielectric permittivity of the mixture and the ceramic respectively.  $R$  is the relative volume density of the ceramic.

## 2.0 Experimental Procedure

### 2.1 Starting material

The hydroxyapatite specimens for this study were made from 99% pure calcium hydroxyapatite (HAP) powder from Cerac Inc., Speciality Inorganics, Milwaukee, WI. Item number C-2071-1, Lot numbers X16907 (designated as HAP I) and X21949 (HAP II). The certificate of analysis, from Cerac Inc., is reproduced in Table 2-1.

Table 2-1 Specific analysis (Ca percentages) and spectrographic analysis (impurities) of the hydroxyapatite powder received from CERAC Inc., Milwaukee, WI. The data is copied from the Certificate of Analysis attached to material.

Element	Lot number X16907T (HAP I)			Lot number X21949 (HAP II)		
	***	**Found %	**Theoretical %	***	**Found %	**Theoretical %
Ca		37.28	37.00		36.24	39.90
Al	< 0.01			<0.01		
Cr	< 0.01			<0.01		
Fe	< 0.01			<0.01		
Mg	0.08			0.1		
Mn	< 0.01			N/A		
Na	< 0.01			N/A		
Si	0.08			0.1		
Sr	<0.01			<0.01		

\* Spectrographic assay

\*\* Specific analysis or property

#### 2.1.1 Particle size analysis

Particle size analysis of the hydroxyapatite powder was performed by Cerac inc. [66] on powder from both lot number X16907T and lot number X21949. The supplied data entered in a spreadsheet and plotted as the percent change in the amount of particles

passed as a function of particle size (Figure 2-1).

### **2.1.2 Ball Milling**

Approximately 120 grams of hydroxyapatite powder was dry ball milled in an attempt to lower the initial powder particle size before forming and sintering. Rectangular specimens R1-R5 and disk specimens numbers 13-17 were made from ball milled HAP powder. Two 250 ml nalgene bottles were each loaded with 40 g of hydroxyapatite (either HAP I or HAP II) and 130 g of alumina grinding media (HDAL 025). Another 250 ml nalgene bottle was loaded with 220 g of zirconia grinding media (Zircon 025C) with 60 g of HAP II. The nalgene bottles were tightly sealed with nalgene screw tops. The nalgene screw tops were secured to the bottle with duct tape. All three nalgene bottles, loaded with HAP and grinding media, were tumbled at 20-40 rpm in a large rock tumbler (Thumlers, Tumbler, Model B, Tru-Square Metal Products, Auburn, WA) for 293 hours. The HAP powder in the bottles adhered to the side and formed a solid mass during tumbling. Squeezing the sides of the bottle and shaking for several seconds freed up most of the powder from the walls. The milling media was filtered from the powder using a small kitchen sieve (~2 mm sieve). The ball milled powders are denoted as HAP Ia, HAP IIa and HAP Iz. The “a” suffix denotes alumina ball milling and the “z” suffix denotes zirconia ball milling. All other specimens were made from as received hydroxyapatite powder.

## **2.2 Specimen preparation**

Thin, dense hydroxyapatite disks (specimen numbers 1-50) and rectangular bars

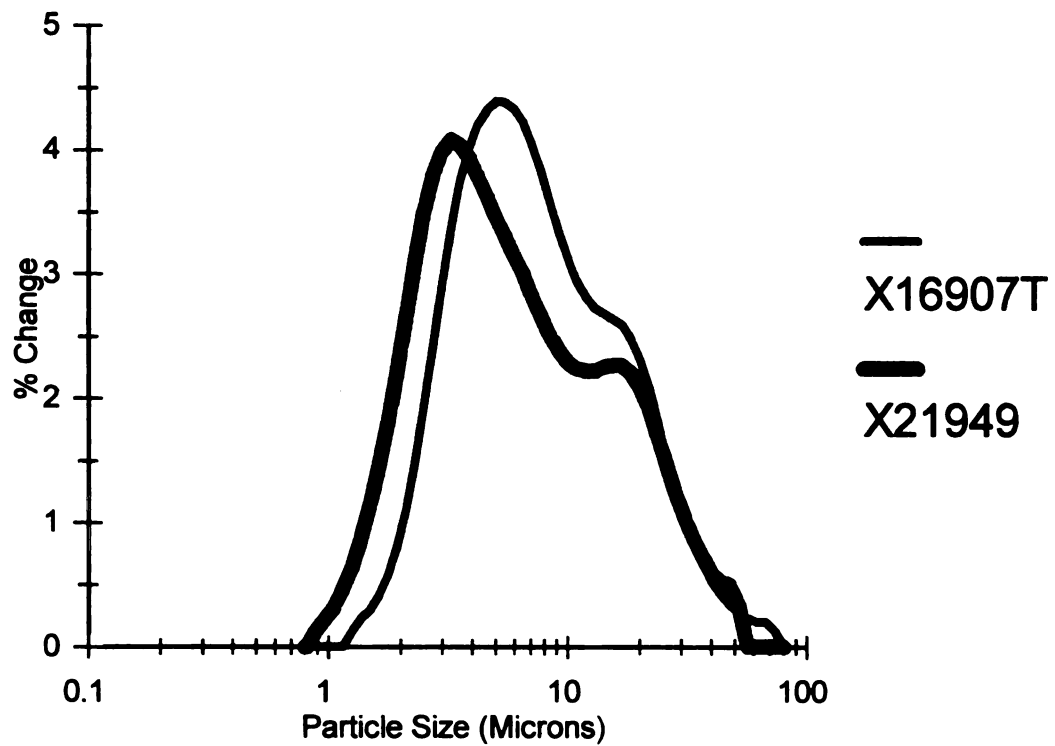


**Figure 2-1** Particle size analysis from Cerac, Inc.[66] for hydroxyapatite powder lot numbers X16907T and X21949, used in this study. Mean values were 10.03 and 8.81 microns with standard deviations of 6.94 and 7.05 microns for hydroxyapatite powder lots X16907T and X21949 respectively.

(specimens R1-R10) were produced from powder, by die pressing and firing (Table 2-2, Table 2-3, Table 2-4, and Table 2-5). Specimens were polished and sectioned to prepare them for further measurements.

### **2.2.1 Die forming**

Hydroxyapatite powder, with no added binder, was uniaxially pressed (Carver Laboratory press, Model C, Fred S. Carver Inc., Menominee Falls, WI) in a cylindrical or rectangular hardened steel die. Applied pressures varied from 6.55 MPa to 24.0 MPa. The disk and rectangular dies were constructed by the Michigan State University Physics Department machine shop (Figures 2-2 and 2-3 respectively). The cylindrical steel die produced disks 5.095 cm in diameter. The rectangular die formed bar specimens 8.89 cm long and 1.27 cm wide. After uniaxial pressing, the steel die was cleaned with acetone and lint free paper towels (Kimwipes EX-L, Kimberly Clark, Roswell, GA). No lubrication was used on the steel dies.

### **2.2.2 Cold isostatic pressing**

Disk specimens numbers 20-23, 31-35 and r8-r11 rectangular bars were cold isostatically pressed (CIP) in a room temperature isostatic press (Iso Spectrum Inc., Columbus, Ohio) after initial uniaxial die pressing (6.55 MPa disk specimens and 7.88 MPa for rectangular specimens). The die pressed hydroxyapatite green bodies were placed in latex condoms to keep them from being contaminated by the water medium in the isostatic press. The air in the loaded condoms was removed using a 30 cc syringe and a blunt needle to withdraw the air. Cotton thread, tied around the opening of the condom

**Table 2-2 Processing parameters for Hydroxyapatite disk specimens. Fired in automatically controlled tube furnace. HAP I is lot number X16907 from CERAC inc. Milwaukee, WI.**

<b>Specimen label</b>	<b>Material</b>	<b>Start mass (g)</b>	<b>Pressure (MPa)</b>	<b>Sintering temperature (°C)</b>	<b>Sintering time (min.)</b>
1	HAP I	8	6.55	1300	60
2	HAP I	8	6.55	1300	75
3	HAP I	8	6.55	1300	45
4	HAP I	8	6.55	1300	90
5	HAP I	12	6.55	1300	105
6	HAP I	12	6.55	1300	240
7	HAP I	12	6.55	1400	120
8	HAP I	12	6.55	1400	240
9	HAP I	12	6.55	1300	300
10	HAP I	12	6.55	1300	420
11	HAP I	12	6.55	1300	540
12	HAP I	12	6.55	1300	660

**Table 2-3 Processing parameters for rectangular HAP Specimens, fired in C+M box furnace under manual control. HAP II is from lot number X21949 from CERAC. HAP Ia, HAP IIa- hydroxyapatite powder ball milled with alumina pellets, HAP Iz- hydroxyapatite powder ball milled with zirconia pellets.**

Specimen label	Material	Start mass (g)	Pressure (MPa)	Sintering temperature (°C)	Sintering time (min.)
R1	HAP Ia	6	23.64	1300	60
R2	HAP Iz	6	23.64	1300	45
R3	HAP IIa	6	23.64	1300	45
R4	HAP IIa	6	19.70	1300	15
R5	HAP IIa	6	19.70	1250	15
R6	HAP II	6	19.70	1300	15
R7	HAP I	5	19.70	1250	15
R8	HAP II	5	250 (CIP)*	1300	15
R9	HAP II	5	250 (CIP)*	1300	120
R10	HAP II	5	250 (CIP)*	1200	15

\* Cold Isostatic Press, Iso Spectrum, Columbus OH.

Table 2-4 Processing parameters for disk HAP Specimens, fired in C+M box furnace under manual control.

Specimen label	Material	Start mass (g)	Pressure (MPa)	Sintering temperature ( $^{\circ}$ C)	Sintering time (min.)
13	HAP IIa	10	24.00	1300	45
14	HAP Iz	10	24.00	1300	60
15	HAP Iz	10	24.00	1300	45
16	HAP IIa	10	17.46	1300	15
17	HAP Ia	10	17.46	1250	15
18	HAP II	10	17.46	1300	15
19	HAP I	10	17.46	1250	15
20	HAP II	9	250 (CIP)*	1300	15
21	HAP II	9	250 (CIP)*	1300	120
22	HAP II	9	250 (CIP)*	1200	15
23	HAP II	9	250 (CIP)*	1250	30
24	HAP II	9	6.55	1200	15
31	HAP I	6	80 (CIP)**	1200	60
32	HAP I	6	80 (CIP)**	1350	60
33	HAP II	6	80 (CIP)**	1100	60
34	HAP II	6	80 (CIP)**	1250	60‡
35	HAP II	6	80 (CIP)**	1150/1300†	60/60†
36	HAP I	6	13.09	1100	60
37	HAP I	6	19.64	1100	60
38	HAP II	6	6.55	1100	60
39	HAP II	6	26.18	1200	60
40	HAP II	6	13.09	1200	60

\* Cold Isostatic Press, Iso Spectrum, Columbus OH.

\*\* Cold Isostatic Press run to 80 MPa three times.

‡ Furnace run interrupted at  $\sim 970^{\circ}$  C, restarted at  $\sim 440^{\circ}$  C.

† Specimens were cupped after first furnace run at  $1150^{\circ}$  C. Specimens re-fired at  $1300^{\circ}$  C for 60 mor minutes.

Table 2-4 Continued

Specimen label	Material	Start mass (g)	Pressure (MPa)	Sintering temperature ( $^{\circ}$ C)	Sintering time (min.)
41	HAP II	6	6.55	1200	60
42	HAP II	6	13.09	1250	60‡
43	HAP II	6	19.64	1250	60‡
44	HAP II	6	26.18	1250	60‡
45	HAP II	6	6.55	1350	60
46	HAP II	6	13.09	1350	60
47	HAP II	6	26.18	1350	60
48	HAP II	6	13.09	1150/1300†	60/60†
49	HAP II	6	19.64	1150/1300†	60/60†
50	HAP II	6	26.18	1150/1300†	60/60†

‡ Furnace run interrupted at  $\sim 970^{\circ}$ C, restarted at  $\sim 440^{\circ}$ C.

† Specimens were cupped after first furnace run at  $1150^{\circ}$ C. Specimens re-fired at  $1300^{\circ}$ C for 60 mor minutes.

Table 2-5 Processing parameters for disk HAP Specimens fired in microwave cavity

Specimen label	Material	Start mass (g)	Pressure (MPa)	Sintering temperature ( $^{\circ}$ C )	Sintering time (min.)
25	HAP II	9	6.545	1050	30
26	HAP II	9	6.545	1100	30
27	HAP II	9	6.545	1150	30
28	HAP I	8	6.545	1200	30

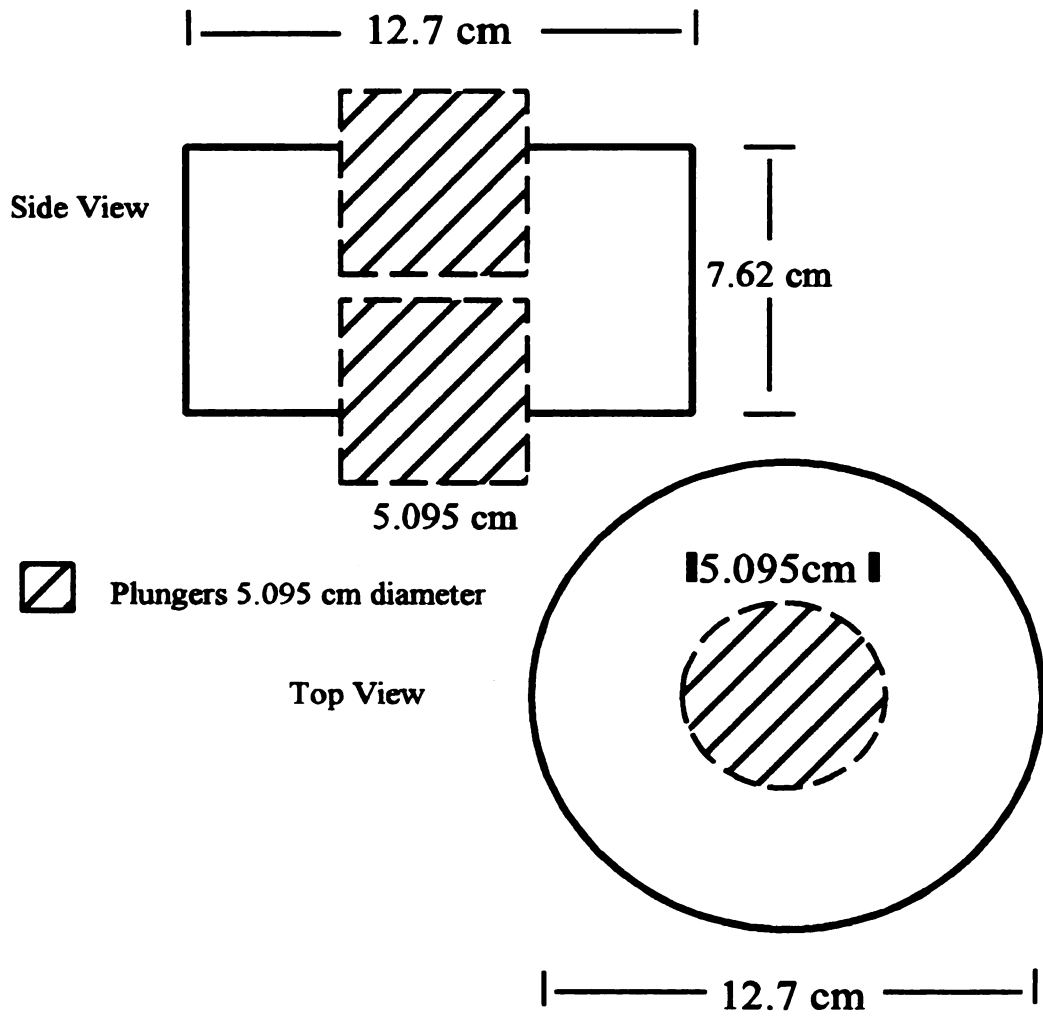
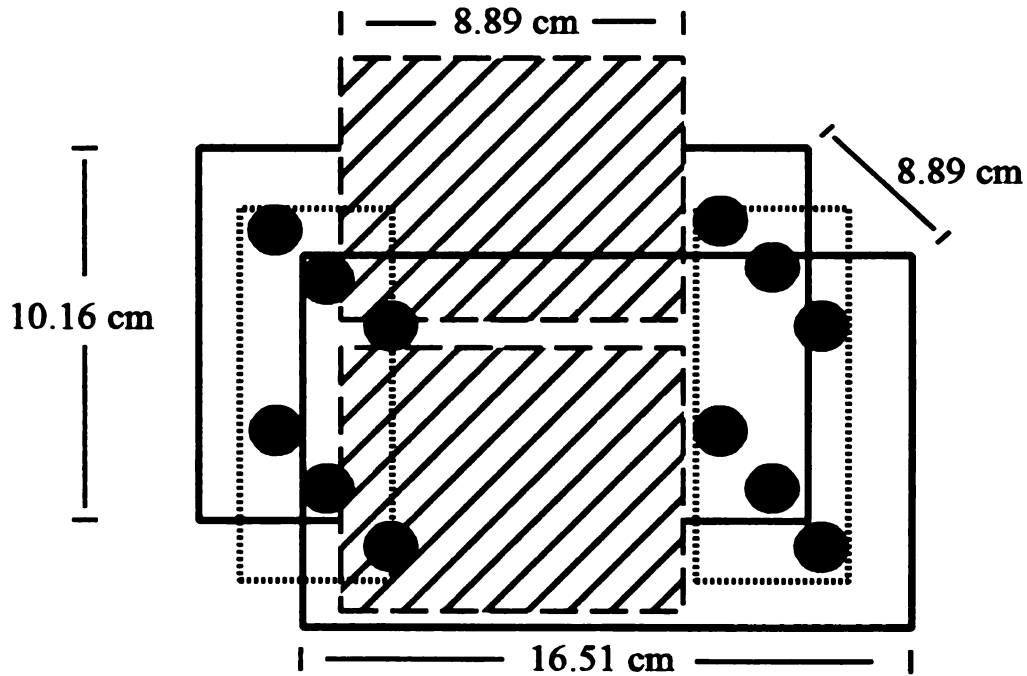


Figure 2-2 Pressing die for disk specimens, fabricated from hardened steel by the Michigan State University Physics Department Machine Shop.



**Exploded View**

- Side Plates 16.51 cm x 10.16 cm x 3.81 cm
- ▨ Plungers 8.89 cm x 6.35 cm x 1.27 cm
- ..... Spacer Plates 10.16 cm x 3.81 cm x 1.27 cm
- Bolt Holes for 5/16"-18 hex head bolts

**Figure 2-3** Rectangular die press, fabricated from hardened steel by the Michigan State University Physics Department Machine Shop. Tolerances set to 0.001". Bolted together with 5/16" - 18, hex head bolts before pressing.

and the needle, was pulled tight as the plunger, on the syringe, was pulled back and the needle was removed from the condom. A second condom was pulled over the material in the first condom and again the air was removed by the syringe and needle. The outside condom was sealed with cotton thread. The double sealed specimens were then secured in the middle of a steel mesh (~3-5 mm mesh) cylinder (10 cm diameter and ~ 30 cm long), which was closed at one end, to keep them from being sucked in to the relief valve when the pressure was released. The mesh cylinder, with the HAP specimens tied with cotton thread to the inside, was placed in the bore of the cold isostatic press, and the specimens were isostatically pressed at room temperature. The specimens pressed at 250 MPa were brought up at 50 MPa/minute and the pressure was slowly released after a minute 250 MPa. The specimens pressed at 80 MPa were brought up and down from atmospheric pressure to 80 MPa three times due to equipment failure (the CIP was set to go to 250 MPa but failed). After removing the specimens from the isostatic press the condoms were cut with scissors and peeled off the ceramic bodies. The cold isostatically pressed green bodies were cleaned with acetone and Kimwipes, to remove latex and lubricant from the HAP specimens, before firing.

### **2.2.3 Conventional furnace sintering**

Specimens numbers 1-12 were fired in a conventional electric tube furnace (Thermtec, Lenton Thermal Designs). The green bodies were placed on a 30 cm long alumina semicircular hollow platen which fit into the 8 cm diameter horizontally aligned alumina furnace tube. A light dusting (100-200 mg) of alumina powder (AKP-50, Sumitoma, Chemical America Inc, New York, NY) was spread beneath the green bodies

on the alumina platen. The alumina powder was used to prevent the bonding of the hydroxyapatite specimen to the alumina platen at high temperatures. The alumina platen and HAP specimens were centered horizontally in the furnace tube near the furnace control thermocouple. The maximum temperature, dwell and ramp rate were input into the process control unit (Model BS4937, type R Eurotherm). Heating and cooling rates were programmed for 10°C/minute to and from room temperature.

Additional HAP specimens (numbers 13-20, and numbers 26-50) were fired in a box furnace C + M Inc., High Temperature Furnaces, Bloomfield, NJ). Pressed hydroxyapatite specimens were set upon a 10 cm diameter alumina platens (3 mm thick) and placed in the center of the floor in the box furnace. A light dusting (100-200 mg) of alumina powder (AKP-50, Sumitoma) was spread between the HAP specimens and the platen. The box furnace temperature was controlled manually by adjusting the element current and using a type R (platinum/platinum-13% rhodium, Omega Engineering, Stamford CT) thermocouple for feedback. The thermocouple bead was placed in the center of the interior of the box furnace at floor level. Ceramic bead insulators, 80% mullite 20% glass from, Omega Engineering (Omegatite 200), insulated the thermocouple wire to the cold junction compensator box (Type R, Omega Engineering). The thermocouple leads and insulation exited the furnace interior through grooves ground into the refractory at the furnace door. The heating rate averaged 10-20°C/minute from room temperature. The cooling rates were manually controlled to less than 20 °C/minute down to 500 °C. Below 500 °C, the furnace interior was convectively cooled to room temperature. A Fluke 77 multimeter was used to read the voltage from the cold junction compensator box output, on the millivolt scale. Millivolt to temperature conversion was

achieved using the “Revised Thermocouple Reference Tables” for type R (N.I.S.T. Monograph 175 Revised to ITS-90), published by Omega Engineering [67].

#### **2.2.4 Microwave sintering**

Microwave sintered specimens (numbers 25-28) were placed on 5 mm thick porous alumino-silicate refractory disk 7.4 cm in diameter (Zircar Fibrous Ceramics, Zircar Products, Florida, NY). The specimen and alumina disk were then placed on the bottom of a cylindrical microwave sintering casket, Figure 2-4. The ends of the cylindrical casket were made up of 2 cm thick top and bottom alumino-silicate insulating board, SALI type (Zircar Fibrous Ceramics), cut into disks 10.5-11 cm in diameter. The body of the refractory casket was made from 1.25 cm thick x 3 cm tall cylinder of low density yttria stabilized zirconia (ZYC, Zircar Fibrous Ceramics). A 5 mm diameter circular view hole was bored through the zirconia cylinder body centered 8 mm from the bottom edge of the low density stabilized zirconia cylinder. The cylindrical casket was centered in the microwave cavity (model CMP-250, Wavemate Inc., Plymouth, MI), with the view hole facing the center of the microwave cavity viewport.

The microwave cavity was powered by a 2kW, 2.45GHz power supply (Sairem, microwave power supply, Vaux-en-Velin, France), in the resonant mode. Microwave power was controlled manually, with a ramp rate of 20-100 watts every 3 minutes. The temperature of the specimen was unknown below 500 °C. The temperature of the specimen was measured by an optical thermometer (Accufiber Model 10 Optical Fiber Temperature Control System, Accufiber Division, Luxtron Corporation, Beaverton, OR) when the temperature was greater than 500 °C.

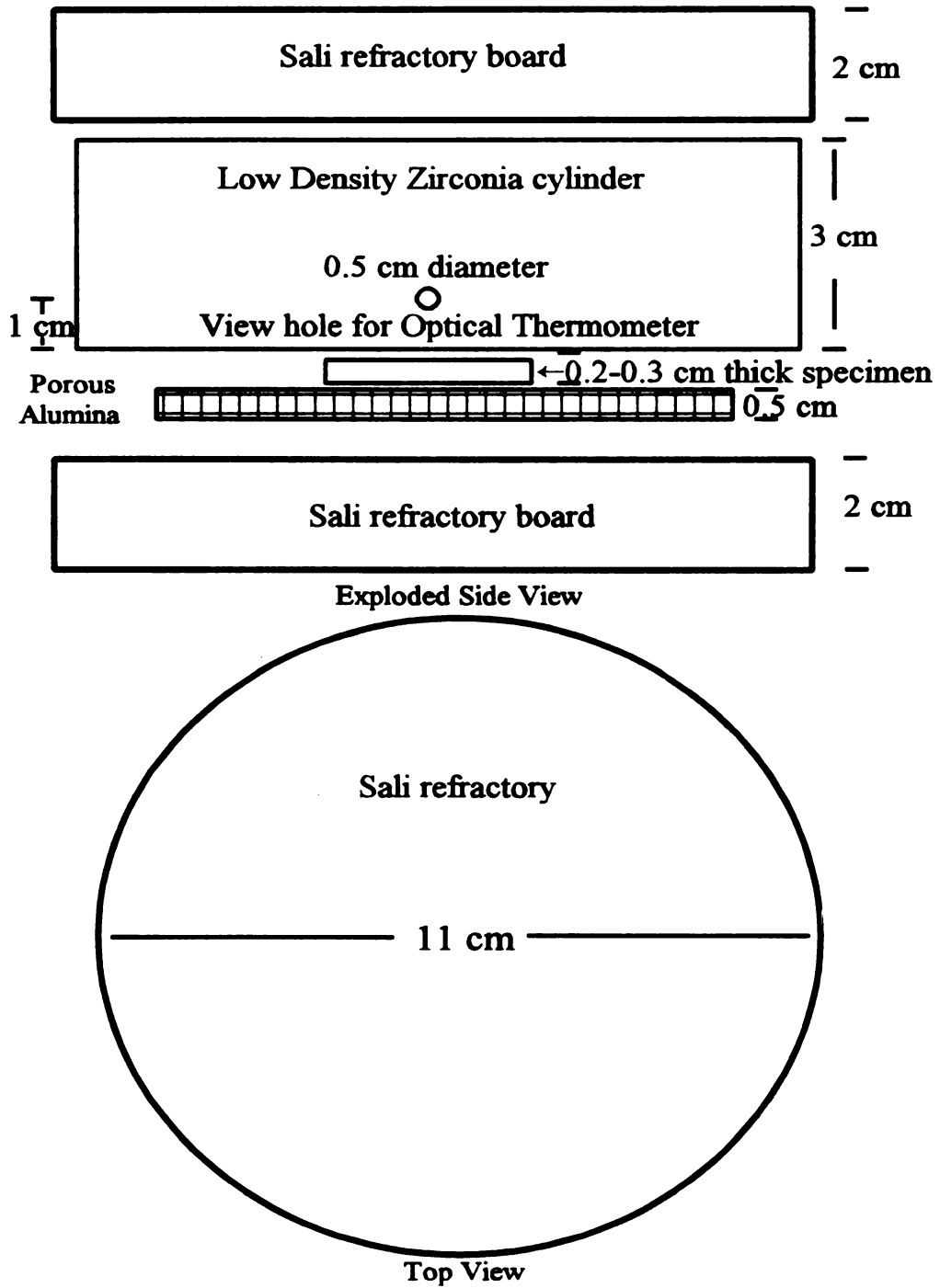


Figure 2-4 Microwave casket assembly. Hydroxyapatite green bodies were placed on the porous alumina disk. The optical thermometer measured the temperature by from the light emitted through the hole 1 cm above the alumina.

Microwave forward power was adjusted and tuned to bring the specimen to the desired temperature (between 1050-1200 °C). The microwave cavity was manually tuned by minimizing the reflected power, accomplished by adjusting the locations of the cavity short and launch probe in the microwave cavity (Figure 2-5). Tuning the cavity short and the launch probe was done when the reflected power increased more than 20% of the previous value. The reflected power was measured at the directional coupler in the microwave transmission line (Microlab/FXR) by a power meter (Model 432A, Hewlett-Packard, Palo Alto, CA). Stepper motors controlled by an IBM XT computer moved the launch probe and the cavity short. Temperature measurements were made using the optical pyrometer measuring the light radiating from the heated specimen through the view hole bored in the side of the microwave casket and passing through the microwave cavity viewport. After sintering, cool down was achieved manually at 10°C/minute to 500°C by manipulating the microwave power. Below 500°C cooling was convective. Tables 2-2, 2-3, 2-4, 2-5 and 2-6 list the forming and sintering data for all the specimens included in this study.

#### **2.2.5 Sectioning the sintered specimens**

Sintered HAP and alumina specimens were sectioned with a slow speed cutting saw (Leco Corporation, St. Joseph, MI) using a 10.16 cm diameter 0.3 mm thick diamond saw (Superabrasive grinding wheel-M4D220-N75M, Norton Company, Worcester, MA), with an oil based lubricant (VC-50, Leco Corporation). The HAP and alumina specimens were then cleaned, by hand, with a liquid detergent (Liquinox, Liquinox Co., Orange, CA) diluted ~10:1 with tap water, then rinsed with copious amounts of tap water. All HAP

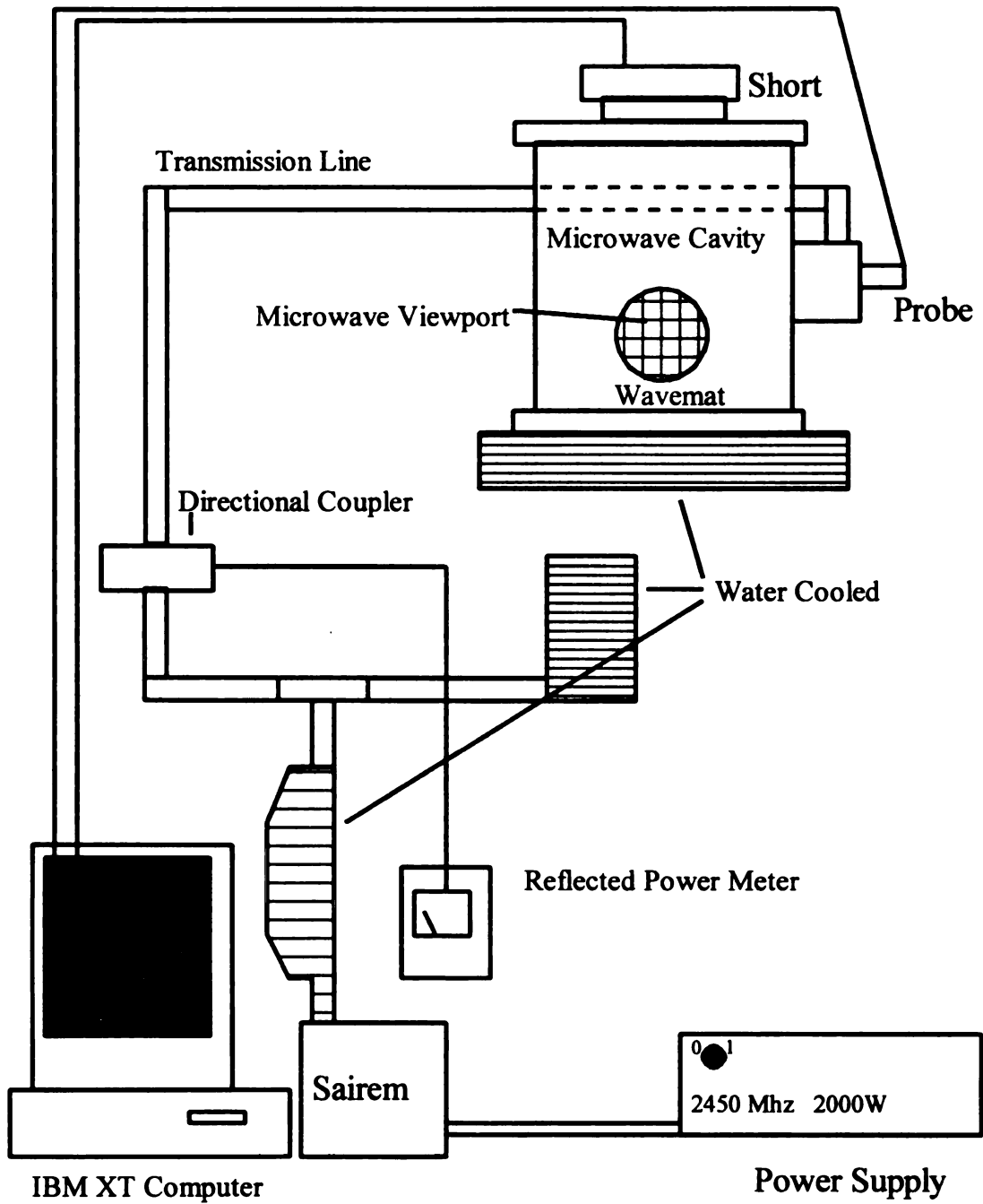


Figure 2-5 Microwave furnace power supply, controls and microwave cavity schematic.

sintered sections were further cleaned with Kimwipes and acetone.

### **2.2.6 Specimen polishing**

Hydroxyapatite specimens and parts of specimens were polished in batches that included 3-10 specimens or parts of specimens of similar thickness (within 20%). The specimens were glued to a flat 1.91 cm thick 19.2 cm diameter aluminum disk with thermoplastic (thermoplastic cement, number 40-8100, Buehler LTD, Lake Bluff IL). The aluminum disk was placed on a hot plate (Cole-Parmer Model number 4658) and heated to melt a 1-3 mm thick layer of thermoplastic. Next the specimens were placed on the liquid plastic and the assembly removed from the heat. An identical aluminum disk was placed on top of the specimens, to press the specimens against the lower aluminum plate until the thermoplastic set.

The polishing machine (Vari-Pol VP-50, LECO Corporation, St. Joseph, MI), used two rotations and a swinging motion (random orbit) to polish the specimens. Size graded diamond grit (Warren Diamond powder company, Olyphant, PA) was applied to grit size specific polishing cloth (LECO Corporation) affixed to a rigid metal disk. The cloth covered disk and the aluminum disk, with which the specimens were glued, were loaded into the polishing machine. The polishing cloth was lubricated with 10-20ml of Ethylene Glycol solution (Microid diamond compound extender, LECO Corporation). The pressure applied on the hydroxyapatite specimens, set by an allen wrench, was set by 1/4 turn tightening of the wrench.

The cloth covered metal disk rotation rate was set to 150 rpm. Seven or eight diamond grit sizes on separate cloth covered metal disks were used, sequentially from the

largest grit to the smallest grit, to polish the specimens. Polishing paste containing diamond grit was graded for 67, 35, 25, 17, 15, 10, 6, and 1 micron sizes.

Initial polishing at grit sizes of 67 or 35 micron polishing evens the surfaces, and for hydroxyapatite specimens required 40-120 minutes. For the intermediate grit sizes (25, 17, 15, and 10 micron) polishing took 15-30 minutes for each size grit. Final polishing of the hydroxyapatite specimen surface was done for 20-30 minutes with 6 micron diamond grit and 30-40 minutes with 1 micron diamond grit. Between grit size changes and after final polishing the aluminum disk with the affixed specimens was removed from the polishing machine, and the specimen surfaces were cleaned with liquinox soap and a soft bristle brush. The disk and the specimens were then rinsed thoroughly with tap water and dried with paper towels.

### **2.2.7 Surface etching**

Thermal etching, in order to measure the average grain size, was performed on hydroxyapatite specimens (numbers 6 - 10 and 12 - 23). Small sections (approximately 3mm x 3mm) of polished hydroxyapatite were arranged on the alumina platen with a light dusting of alumina powder (AKP-50, Sumitoma), to keep the specimens from bonding to the alumina plate at high temperature. The specimens were placed in the box furnace and brought to 1300<sup>o</sup>C for 1 hour. Heating and cooling rates were approximately 10<sup>o</sup>C/minute to and from 1300<sup>o</sup>C. Sketches of the specimen shapes and arrangements on the plate were made for specimen identification upon retrieval from the furnace.

Acid etching, for grain size measurements, was done on hydroxyapatite specimens (numbers 1-5, and 11), using 0.1 M hydrochloric acid at room temperature. Small

polished sections (approximately 3mm x 3mm) were set in a 50 ml glass beaker containing 15-20 ml of 0.1 M HCl, with nalgene tweezers, for 1 minute. The specimens were removed from the acid with nalgene tweezers, placed in a 100 ml nalgene beaker full of tap water and rinsed with a large volume of tap water.

### **2.2.8 Specimen mounting for scanning electron microscopy**

Prepared hydroxyapatite specimens (sectioned and polished and either etched or indented) were attached to an aluminum disk (SEM specimen mount) with carbon tape (Structure Probe Inc., West Chester, PA) with the specimen surface of interest facing upwards. The surface of interest of the specimens was coated with ~ 21 nm of gold by a plasma coating machine (Emscope, SC500). Coating parameters set for the Emscope plasma coating machine were 3 minutes coating time (plasma on), with a current of 20 mA. The deposition rate was 7 nm/minute, at 20 mA, according to the manufacturer's specifications [68].

## **2.3 Microstructure measurements**

The sintered specimens were initially characterized for density, grain size, and crystalline structure, which are grouped as process variables. Further measurements of hardness, toughness, thermal expansion, and dielectric properties were made on the specimens and related to the process variables.

### **2.3.1 Mass density**

Density measurements were made by Archimedes method on whole or sectioned

sintered hydroxyapatite specimens. The mass of the specimen dry, wet (by distilled water), and suspended in distilled water were measured three times, and these measurements are averaged. Dry specimens were measured, to 0.1 mg precision, on an electronic laboratory scale (Accutron, Denver Instrument Co. Arvada, CO). Suspended measurements were made by measuring the mass of the specimen minus the weight of the distilled water displaced by the specimen (Figure 2-6). The wet specimens were measured after the suspended measurement, the surface water was wiped off with damp Kimwipes before measuring. The difference in the mass of the wet specimen and the suspended specimen is the mass of the displaced distilled water and can be converted into a volume using  $1 \text{ g} = 1 \text{ cm}^3$ . The dry mass was then divided by the volume of the displaced water to determine the specimen density (Equation 2-1).

$$\text{density} = (\text{dry mass}) / [(\text{wet mass} - \text{suspended mass}) / (1 \text{ g/cm}^3)] \quad (2-1)$$

The specimen density was then divided by the theoretical density of the hydroxyapatite (theoretical density of hydroxyapatite =  $3.156 \text{ g/cm}^3$ ), then multiplied by 100 to obtain the relative density as a percent of theoretical density.

### **2.3.2 Grain size measurements**

Grain sizes were calculated from scanning electron microscope (Hitachi S-2500C) micrographs of polished, etched and gold plated surfaces of sintered hydroxyapatite specimens. One or more images were taken at magnifications of 2000X or greater with Polaroid 55 film (Polaroid Corporation, Cambridge, MA). Twenty to thirty more lines of

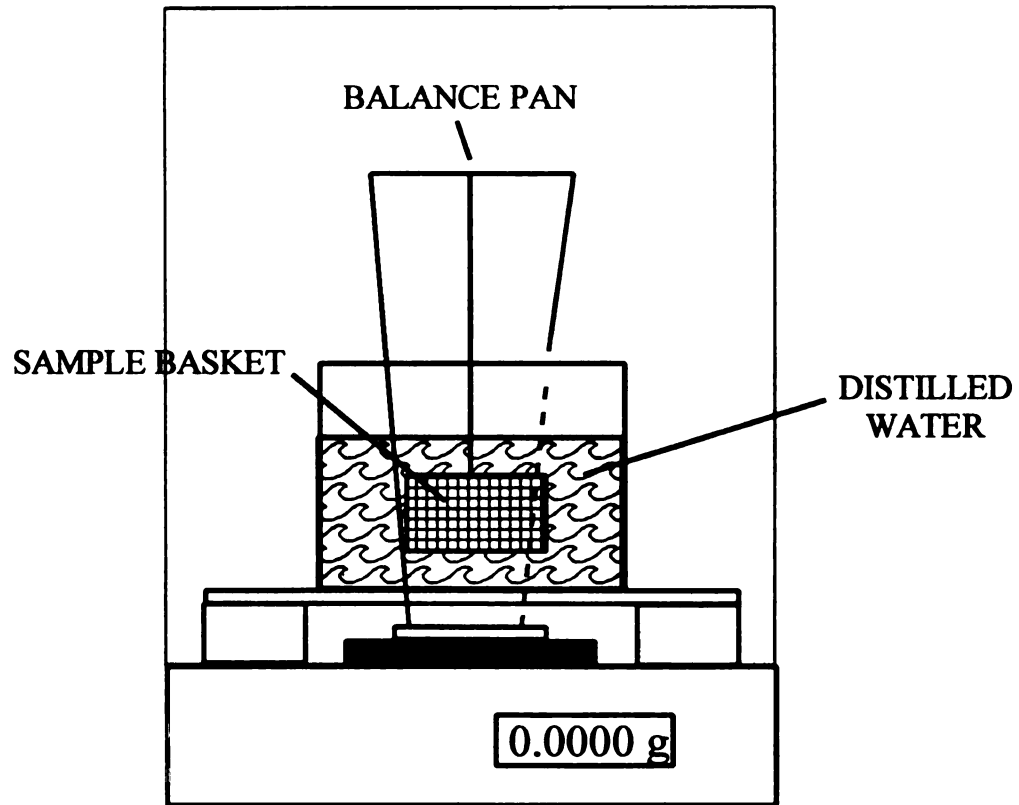


**Figure 2-6** Apparatus for measuring the mass density of the hydroxyapatite specimens using Archimedes method. The sintered specimens were placed into the basket for the suspended mass measurement.

5 cm were superimposed on the micrographs and the grain boundary intercepts along these lines were counted. The total length of the superimposed lines was divided by the number of intercepts multiplied by the magnification in order to determine the average grain size of the specimen (Equation 2-2).

$$g.s. = \frac{L_u}{N_i \cdot M} \cdot X \quad (2-2)$$

where g.s. = Grain size (meters),  $L_u$  = Total length of the drawn test line(s) (meters),  $N_i$  = Total number of grain boundary intercepts,  $M$  = Magnification of image,  $X$  = Geometric constant (1.0 was used for HAP). An excess of 200 intercepts/image were used in the calculations.

### 2.3.3 X-ray diffraction

Unsintered hydroxyapatite powder (HAP I from Cerac Inc.) and sintered hydroxyapatite powder were pressed into a  $\sim 3/16$  " diameter ground out depression in a glass microscope slide. The glass microscope slide was ground out with a coarse SiC grit impregnated 1/4" diameter brass ball on the end of a 5 - 3000 rpm variable speed rotary tool (Sears and Roebuck and Co., Hoffman Estates, IL) . The sintered powder was obtained from the sintered specimens numbers 6-9, 11 and 12 by crushing and grinding a small (approximately 4 mm x 4 mm) section using a Coors porcelain mortar and pestle (mortar number 60316, pestle number 522-4, Coors Ceramics Company, Golden, CO). The grinding was done until the powder was very fine and adhered to the side of the mortar. About 10-20 turns of the pestle were required to produce appropriate powders

once the specimen was broken up. The glass slide with the hydroxyapatite powder sample was installed into the target holder in the SCINTAG 2000 x-ray machine (Model number XDS 008, serial number 091, Scintag USA inc.). The powder sample was then irradiated with a parallel beam of  $\text{CuK}\alpha_1$  radiation ( $\lambda = 15.405\text{nm}$ ) collimated from the x-ray source by 2mm and 2mm slits (40 mm apart) and then a nosepiece 54 mm long with a 1.5 mm diameter hole. The x-rays were collimated after the sample by 0.5mm and 0.3mm slits 40 mm apart before the x-ray detector. A step scan program was run at 0.2 min/degree with a step of 0.02 degrees. The counts versus diffraction data were stored in the controlling computer (various PC's, with proprietary software from Scintag). A Scintag program converted the binary data into ASCII which was then downloaded into a spreadsheet (Quattro Pro 8, Corel Corporation, Ottawa, Ontario, Canada) for analysis and plotting.

The plane spacings for each specimen were calculated using the wavelength from  $\text{CuK}\alpha_1$ , the  $2\theta$  peak from the three major diffraction peaks on the diffraction curve, and the Bragg law (Equation 2-3).

$$\lambda = 2 d \sin\theta \quad (2-3)$$

From the plane spacing the lattice parameters (a and c) were calculated using the plane index for the three major diffraction peaks, from the ASTM powder diffraction files for inorganic phases [69], and the plane spacing equation for the hexagonal lattice from appendix 3 in Cullity [70] (Equation 2-4).

$$\frac{1}{d^2} = \frac{4}{3} \left( \frac{h^2 + hk + k^2}{a^2} \right) + \frac{l^2}{c^2} \quad (2-4)$$

## 2.4 Hardness and fracture toughness measurements

Hardness and toughness measurements were made by measuring Vickers indentations on the polished faces of the hydroxyapatite specimens (Vickers micro hardness tester, Buehler LTD, Lake Bluff IL). Loads of 2.94 N, 4.90 N, and 9.81 N were used with a 10 second loading time and a head speed of 70  $\mu\text{m/s}$ . To guarantee 7 to 10 recordable indents, 10 to 20 indentations per specimen were made. Indentations with surface spalling were rejected. For the hardness calculation the diagonal lengths of the indent (2a), in meters, were recorded (Figure 2-7). The total length of the radial cracks plus the diagonal lengths of the indent, (2c), were measured and recorded for the toughness calculation.

The hardness and toughness of the sintered HAP specimens were calculated using Equations (2-5) and (2-6) and the Vickers indentation measurements. These equations and the empirical constant  $\zeta$  were from Antsis et al. [40] presented by Wachtman [71]. The hardness H is calculated in GPa by Equation 2-5.

$$H = P / 2a^2 \quad (2-5)$$

where P is the load in Newtons, a is 1/2 the length of the indent diagonal in meters.

Fracture toughness  $K_{IC}$  was calculated using Equation 2-6.

$$K_{IC} = \zeta (E/H)^{1/2} P c^{-3/2} \quad (2-6)$$

where  $\zeta = 0.016$ , E is the elastic modulus (115 Gpa [12]), H is the hardness calculated in

(2-4),  $P$  is the load in Newtons and  $c$  is  $1/2$  the indent crack length in meters.

## **2.5 Thermal expansion**

### **2.5.1 Specimen preparation for thermal expansion measurements**

Thermal expansion measurements used hydroxyapatite specimens numbers 4-8, 10-12 and a sintered alumina reference specimen (starting powder AKP 30-4 Sumitoma) microwave sintered at  $1500^{\circ}\text{C}$  for 30 minutes by KiYong Lee, a colleague in the Material Science Department at Michigan State University. The specimens were cut into rectangles approximately  $10\text{mm} \times 5\text{mm} \times 3\text{mm}$  with the slow speed diamond saw. The long axis opposing faces were ground parallel by hand sanding with wet 320, 400 and 600 grit wet/dry silicon carbide paper (3M corp. Minneapolis MN). Final surface polishing of the opposing faces was done by hand on the Vari-Pol polishing machine at 150 rpm with grit sizes starting at  $17\ \mu\text{m}$ , then  $15\ \mu\text{m}$  and finally  $10\ \mu\text{m}$ , for 2-3 minutes at each grit size. Hydroxyapatite specimens numbers 4-8, 10-12, and the alumina specimen were then annealed at  $900^{\circ}\text{C}$  in a box furnace (Type 59344, Lindbergh Blue, Asheville, NC) for 13 hours.

### **2.5.2 Thermal expansion measurement**

Hydroxyapatite and alumina specimens were placed one at a time in the specimen well of the thermomechanical analyzer (DuPont Instruments, Model 943) so that the measurement was to be made on the long axis. The thermomechanical analyzer was programmed to heat the specimen at  $10^{\circ}\text{C}/\text{minute}$  to  $800^{\circ}\text{C}$ , hold at  $800^{\circ}\text{C}$  for 0, 10, 20,

30, or 60 minutes. Thermal expansion data were recorded continuously during heating to 800° C and the cooling to room temperature. Thermal expansion coefficients were calculated, in  $\mu\text{m}/\text{m}^{\circ}\text{C}$ , at 25° C intervals and the data was inserted into a spreadsheet.

## **2.6 Dielectric measurements**

### **2.6.1 Specimen preparation for dielectric measurements**

Disk specimens with both surfaces parallel and polished to 1 micron (see section 2.2.6) and at least a 2.22 cm diameter continuous surface were used for the dielectric measurements.

### **2.6.2 Dielectric apparatus and measurements**

Quality factor (Q), and parallel capacitance ( $C_p$ ), measurements of sintered hydroxyapatite specimens (numbers 14, 16, 33, 36, 41-46, 49, 50) and an alumina substrate material (ADS 995, Coors Ceramics Company, Golden CO) were made with a Q-Meter (Model 4342A, Hewlett-Packard, Palo Alto, CA). The alumina substrate material (ADS 995) was used as a reference material since the dielectric properties are well documented [72]. A guarded electrode system (similar to the ASTM standard- D 150-95 [73]) was constructed from rigid copper and copper pipe (Figure 2-7). The copper electrodes, copper guard ring and the G10 (Glass fabric and epoxy resin system) were cut on a lathe. The contact surfaces of the copper electrodes and guard ring were polished with 25 $\mu\text{m}$  diamond paste on the Leco random orbit polishing machine, using a specimen holder designed to polish parallel surfaces. The rigid copper electrodes were

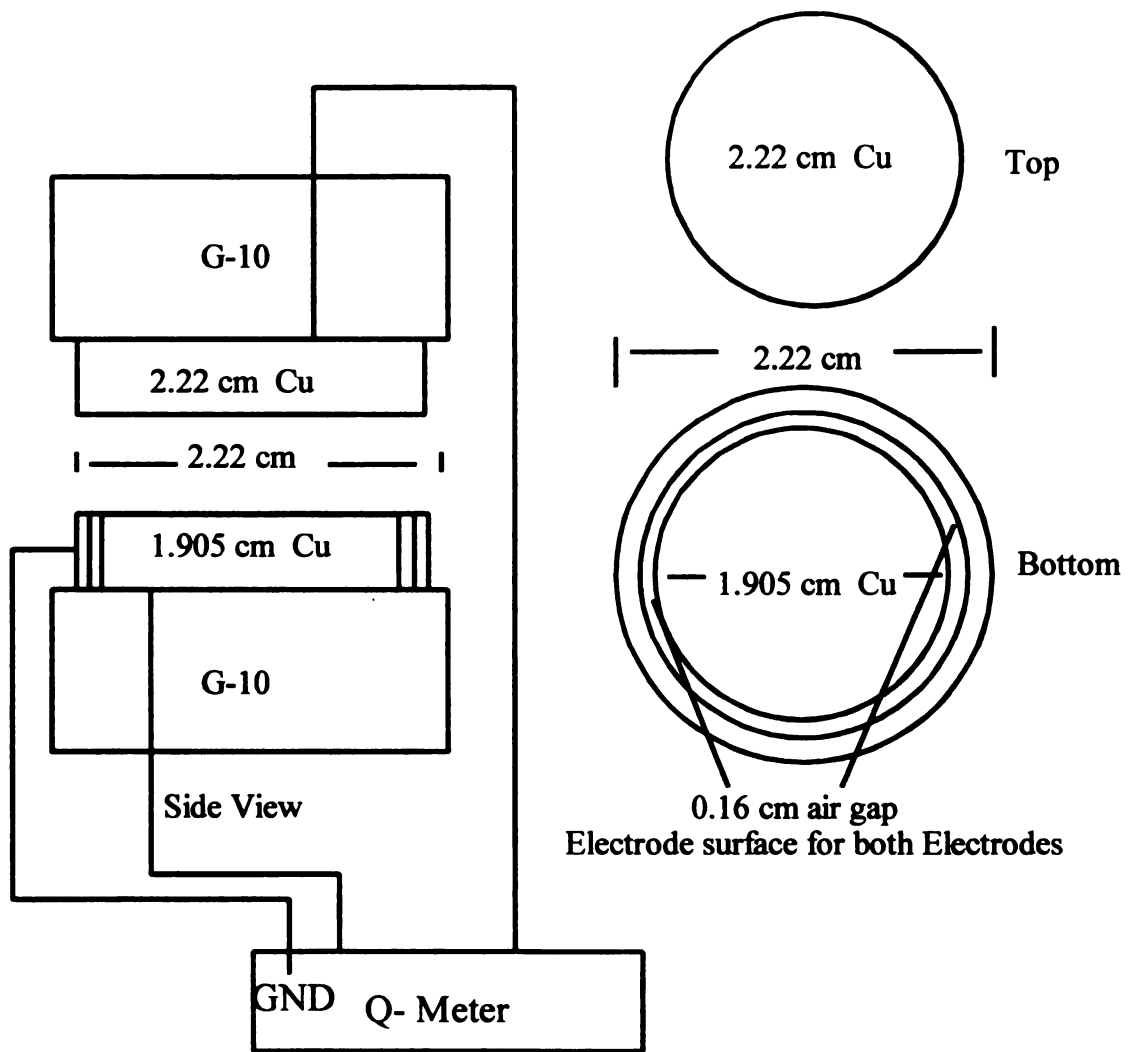


**Figure 2-7** Electrodes and experimental apparatus for the dielectric measurements. The specimen was placed between the top and bottom electrodes. The electrodes were pressed onto the hydroxyapatite surfaces by a 5.09 cm maximum opening micrometer (not shown).

held in place and compressed on the ceramic specimen by a 2 inch micrometer (China).

The dielectric measurements were made using the “Parallel Connection” for high impedance components using reference inductors for each frequency range (reference inductors 16471A through 16490A, Hewlett-Packard). The parallel connection circuit was used (Figure 2-8). Resonance was first established in the circuit without the unknown Z. The Q ( $Q_1$ ) and the capacitance ( $C_1$ ) are recorded. The unknown Z (specimen in the electrode apparatus) is then connected and a new resonance established in the circuit. The new Q ( $Q_2$ ) and capacitance ( $C_2$ ) were recorded. The effective Q, and the effective parallel capacitance  $C_p$  were then calculated (Equations 2-7 and 2-8).

$$Q = Q_1 Q_2 (C_1 - C_2) / (\Delta Q C_1) \quad (2-7)$$

$$C_p = (C_1 - C_2) \quad (2-8)$$

Three capacitance measurements and three Q measurements were taken at 45 kHz for the hydroxyapatite specimens and the ADS995 alumina substrate. The averages of the three capacitance measurements and three Q measurements taken at 45 kHz were then used to correct for the capacitance of the circuit using the calculated capacitance of the ADS995 alumina substrate. Additional measurements were taken at 8 higher frequencies, from 72.2 kHz to 7.3 MHz (one measurement per frequency) at room temperature for the hydroxyapatite specimens and the Coors alumina substrate ADS 995.

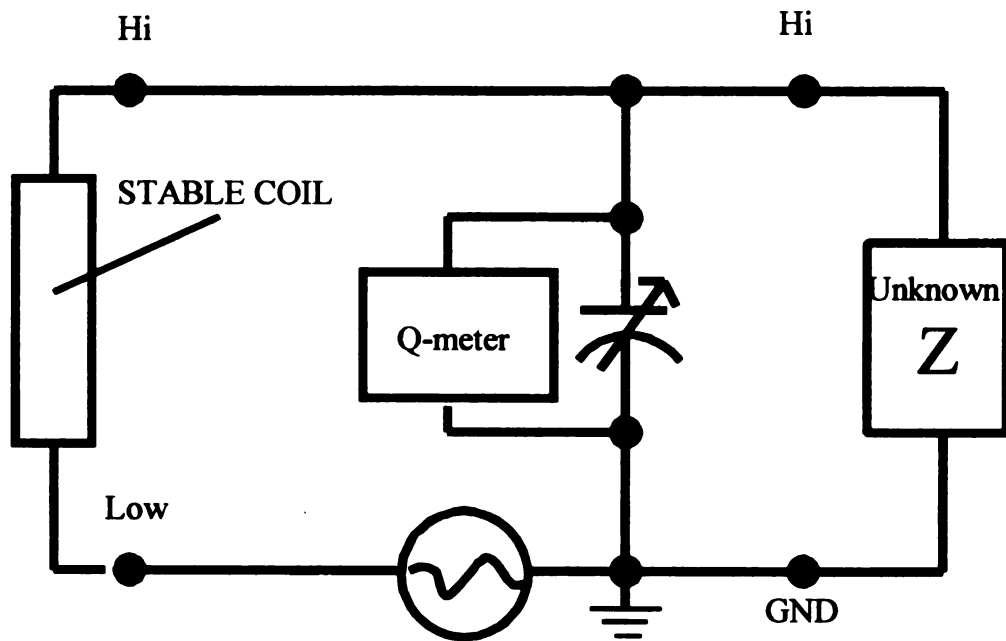


Figure 2-8 Parallel circuit for Q-meter measurements.

### **3 Results and Discussion**

#### **3.1 Sintered hydroxyapatite microstructure**

Processing parameters for sintered hydroxyapatite were varied to allow for a wide range of density and grain size of the sintered microstructure (Table 3-1).

##### **3.1.1 Sintered density**

For the uniaxially die pressed conventionally sintered hydroxyapatite specimens, die pressure has the most significant influence on the final density (Figure 3-1). A linear relation between die pressure and final sintered density was calculated. The relative density for sintered hydroxyapatite specimens sintered at 1300<sup>o</sup> C for less than 120 minutes (numbers 1-5, 13-16 and 18, see Table 3-1) were linear when plotted as a function of the applied uniaxial die pressure (Figure 3-2). Linear regression analysis (Quattro Pro, Corel , Ontario, Canada) determined a slope of 0.27% relative density for every 1 MPa of applied pressure. The coefficient of determination  $r^2 = 0.997$  for the regression analysis.

The densification rate for hydroxyapatite sintered for 60 minutes was significantly enhanced at temperatures greater than 1100<sup>o</sup> C (Figure 3-3).

##### **3.1.2 Sintered grain size**

Average grain size as a function of sintering temperature and sintering time shows significant scattering (Figure 3-4). This is partially due to the differences in the ramping rates and furnace geometries for the two conventional furnaces used in this study. Ramp rates were electronically controlled in the tube furnace to 10<sup>o</sup> C/min and manually controlled in the box furnace to 5-20<sup>o</sup> C/min. The grain size-sintering temperature Table

3-1 Processing parameters, density and grain size data for sintered hydroxyapatite

Specimen label	Pressure (MPa)	Sintering time (min)	Sintering temperature (°C)	Furnace type	Density (g/cm <sup>3</sup> )	Grain size (microns)
1	6.55	60	1300	Tube*	2.88	1.68
2	6.55	75	1300	Tube*	2.88	1.65
3	6.55	45	1300	Tube*	2.88	1.98
4	6.55	90	1300	Tube*	2.89	2.07
5	6.55	105	1300	Tube*	2.88	2.14
6	6.55	240	1300	Tube*	2.92	2.32
7	6.55	120	1400	Tube*	3.05	5.65
8	6.55	240	1400	Tube*	3.06	7.44
9	6.55	300	1300	Tube*	2.97	5.93
10	6.55	420	1300	Tube*	2.95	5.93
11	6.55	540	1300	Tube*	2.98	6.73
12	6.55	660	1300	Tube*	2.79	6.80
13	24.00	45	1300	Box**	3.04	4.37
14	24.00	60	1300	Box**	3.00	3.70
15	24.00	45	1300	Box**	3.05	3.60
16	17.46	15	1300	Box**	2.96	2.74
17	17.46	15	1250	Box**	2.89	4.09
18	17.46	15	1300	Box**	2.98	5.10
19	17.46	15	1250	Box**	2.84	N/A
20	250	15	1300	Box**	3.09	2.30

\* Tube furnace Thermtec, Lenton Thermal Designs

\*\* Box furnace C+M Inc., High Temperature Furnaces Bloomfield NJ

Table 3-1 continued

Specimen label	Pressure (MPa)	Sintering time (min)	Sintering temperature (°C)	Furnace type	Density (g/cm <sup>3</sup> )	Grain size (microns)
21	250	120	1300	Box**	3.09	2.60
22	250	15	1200	Box**	2.92	1.99
23	250	30	1250	Box**	3.07	2.06
24	6.55	15	1200	Box**	2.47	4.44
25	6.55	30	1050	μ-wave*	2.26	2.73
26	6.55	30	1100	μ-wave*	2.65	3.09
27	6.55	30	1150	μ-wave*	2.95	3.85
28	6.55	30	1200	μ-wave*	2.98	4.36
31	80	60	1200	Box**	3.02	5.05
32	80	60	1350	Box**	N/A	4.78
33	80	60	1100	Box**	1.83	1.48
34	80	60	1250	Box**	3.06	2.54
35	80	60,130	1150,1300	Box**	3.02	2.70
36	13.09	60	1100	Box**	2.08	2.87
37	19.64	60	1100	Box**	2.17	3.92
38	6.55	60	1100	Box**	1.54	N/A
39	26.18	60	1200	Box**	2.80	2.54
40	13.09	60	1200	Box**	2.59	2.67
41	6.55	60	1200	Box**	2.43	2.40
42	13.09	60	1250	Box**	2.95	2.80
43	19.64	60	1250	Box**	2.99	3.31

\* Microwave Furnace, Wavemat Cavity, Plymouth, MI; Power Supply, Sairem Vaux-en-Velin, France

\*\* Box furnace C+M Inc., High Temperature Furnaces Bloomfield NJ

Table 3-1 continued

Specimen label	Pressure (MPa)	Sintering time (min)	Sintering temperature (°C)	Furnace type	Density (g/cm <sup>3</sup> )	Grain size (microns)
44	26.18	60	1250	Box**	3.00	2.89
45	6.55	60	1350	Box**	2.96	4.59
46	13.09	60	1350	Box**	2.90	3.33
47	26.18	60	1350	Box**	2.98	N/A
48	13.09	60,130	1150,1300*	Box**	2.89	N/A
49	19.64	60,130	1150,1300*	Box**	2.92	N/A
50	26.18	60,130	1150,1300*	Box**	2.94	4.46

\* First run at 1150° C for 60 minutes and specimens came out badly cupped, second run at 1300° C for 130 minutes.

\*\* Box furnace C+M Inc., High Temperature Furnaces Bloomfield NJ

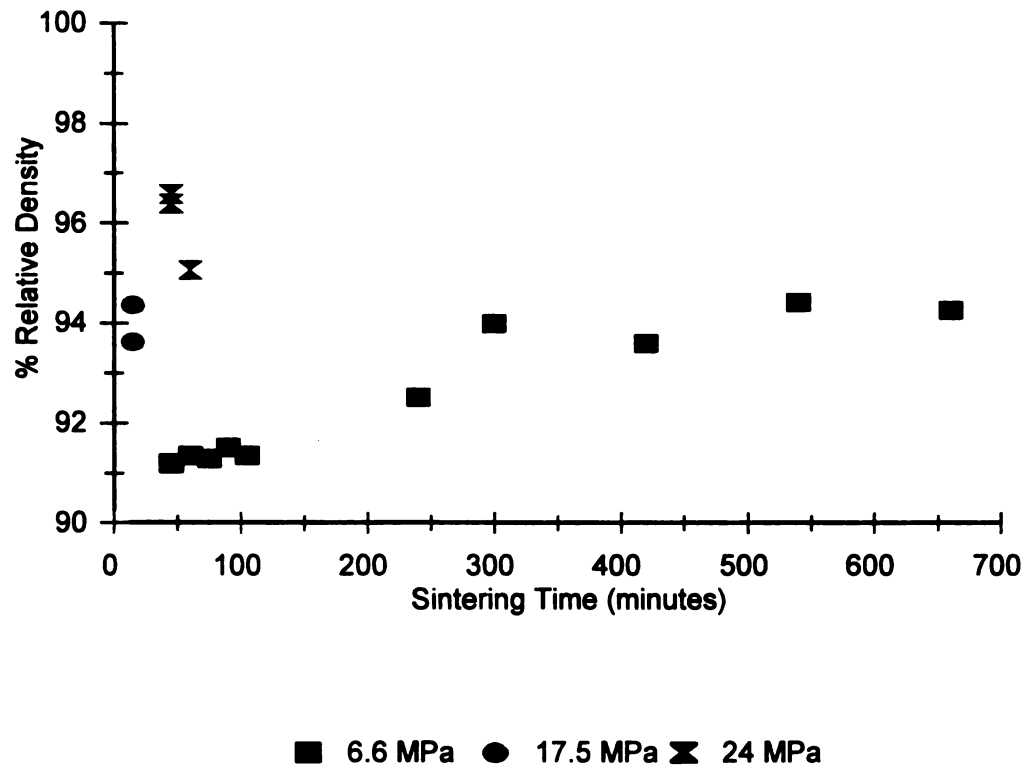


Figure 3-1 Density as a function of sintering time and different uniaxial die pressures for hydroxyapatite sintered in the conventional furnaces at 1300 °C. The data was taken from a subset of the data presented in Table 3-1.

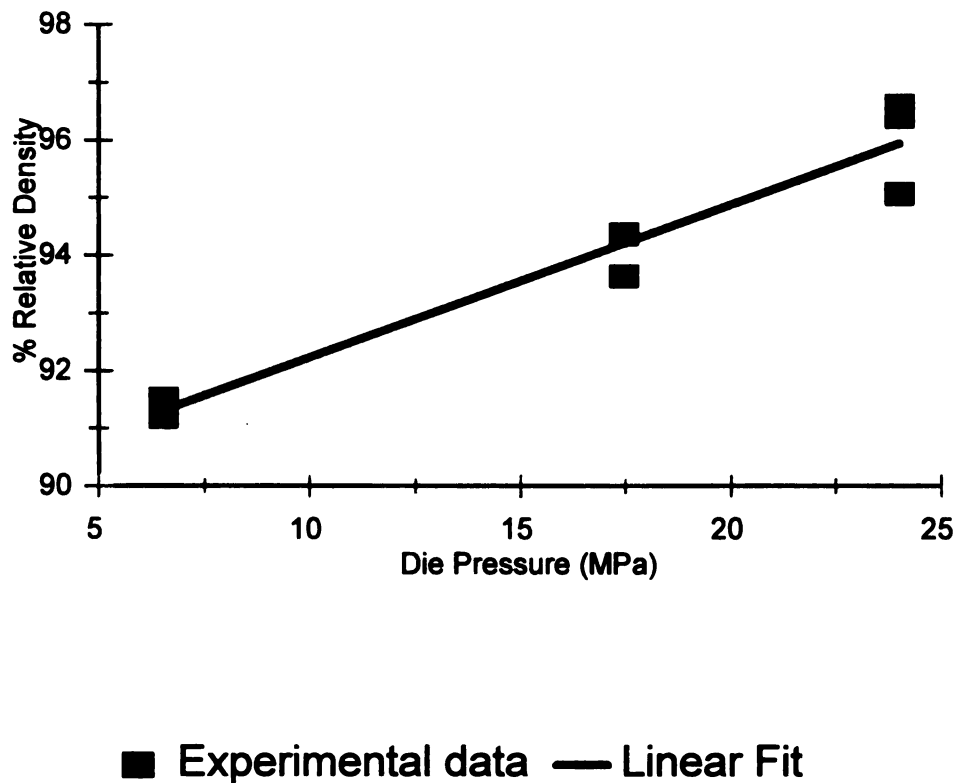


Figure 3-2 Density as a function of die pressure. The data was taken from sintered hydroxyapatite specimens sintered at 1300<sup>o</sup> C for 15-120 minutes, which are a subset of the data presented in Table 3-1. Linear fit represents the least squares fit of the data to equation 3-1. Fit parameters are slope = 0.27% relative density per 1 MPa die pressure, y-intercept = 91% relative density and the coefficient of determination  $r^2 = 0.997$ .

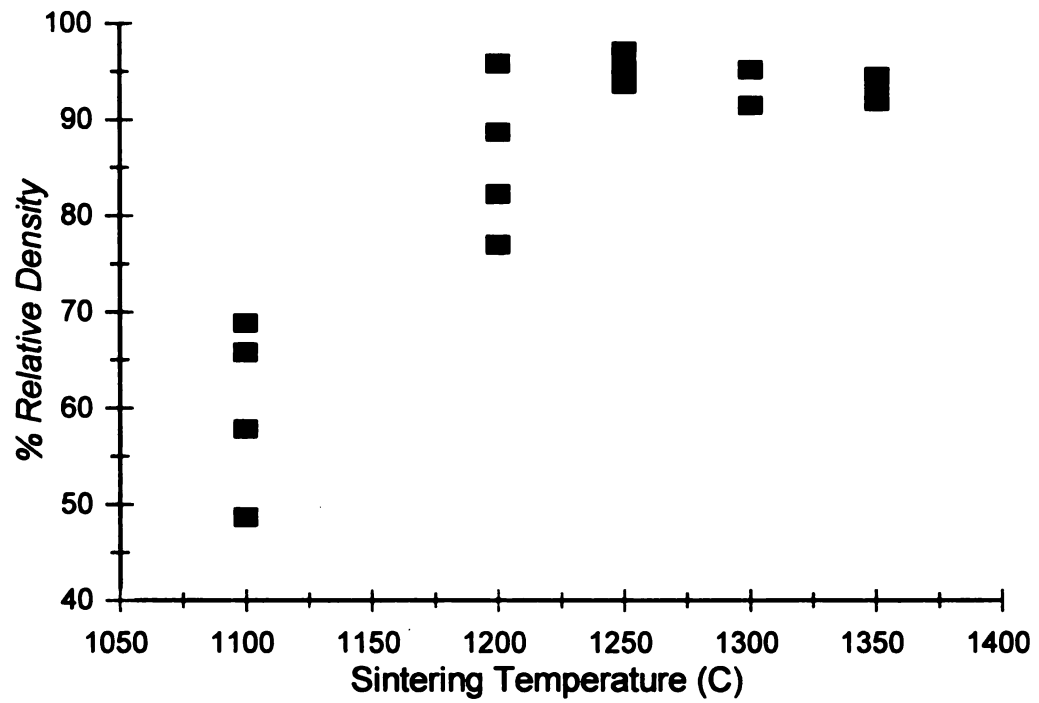
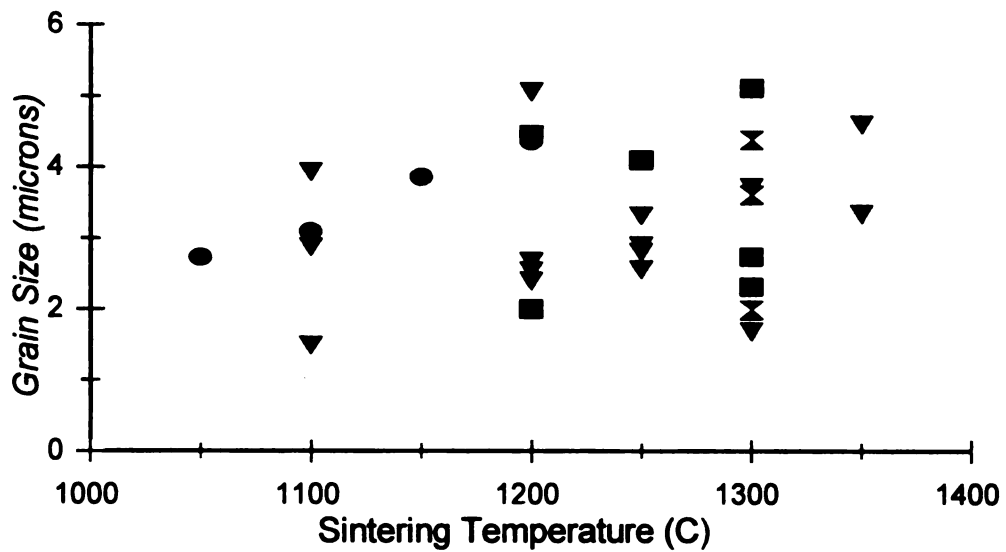


Figure 3-3 Density as a function of sintering temperature for hydroxyapatite specimens sintered for 60 minutes. The data was taken from a subset of the data presented in Table 3-1.



■ 15 min                      ● Microwave 30 min.  
 ⌘ 45 min.                      ▼ 60 min.

Figure 3-4 Average grain size of sintered hydroxyapatite as a function of sintering temperature and time for both conventional and microwave sintering. The data was taken from a subset of the data presented in Table 3-1.

relationship for microwave sintered hydroxyapatite samples is linear for the small sample size of 4 specimens (Figure 3-4). The grain size was decoupled from the density for sintered hydroxyapatite specimens with densities greater than 2.90 g/cm<sup>3</sup> (Figure 3-5).

### **3.1.3 Etched surface morphology**

Uniaxially pressed sintered hydroxyapatite specimens were polished and thermally etched for the grain size measurements. The thermally etched surfaces of the uniaxially pressed sintered HAP specimens were composed of polygonal grain shapes (Figure 3-6 and Figure 3-7). Polished surfaces of the hydroxyapatite surfaces were also acid etched to delineate the grain boundaries and measure the grain size. Acid etching (HAP specimens numbers 1-5, 11) resulted in severe changes in the surface due to over etching (Figure 3-8).

Polished and thermally etched surfaces of the hydroxyapatite specimens cold isostatically pressed to 250 MPa (numbers 20-23) exhibit significantly different etched surface morphology. CIPed specimens sintered for 30 minutes or less at temperatures of 1300<sup>o</sup> C or less had average grain sizes of 1.99 μm , 2.06 μm 2.3 μm (Figure 3-9, Figure 3-10, Figure 3-11 respectively). Specimen number 21, sintered at 1300<sup>o</sup> C for 120 minutes, grew the familiar polygonal shaped grains with an average grain size of 2.60 microns (Figure 3-12).

### **3.1.4 X-ray diffraction**

The diffraction scan, using Cu Kα<sub>1</sub> radiation (λ = 15.406 nm), was from 25 degrees to 36 degrees where the most intense peaks from HAP and the decomposition

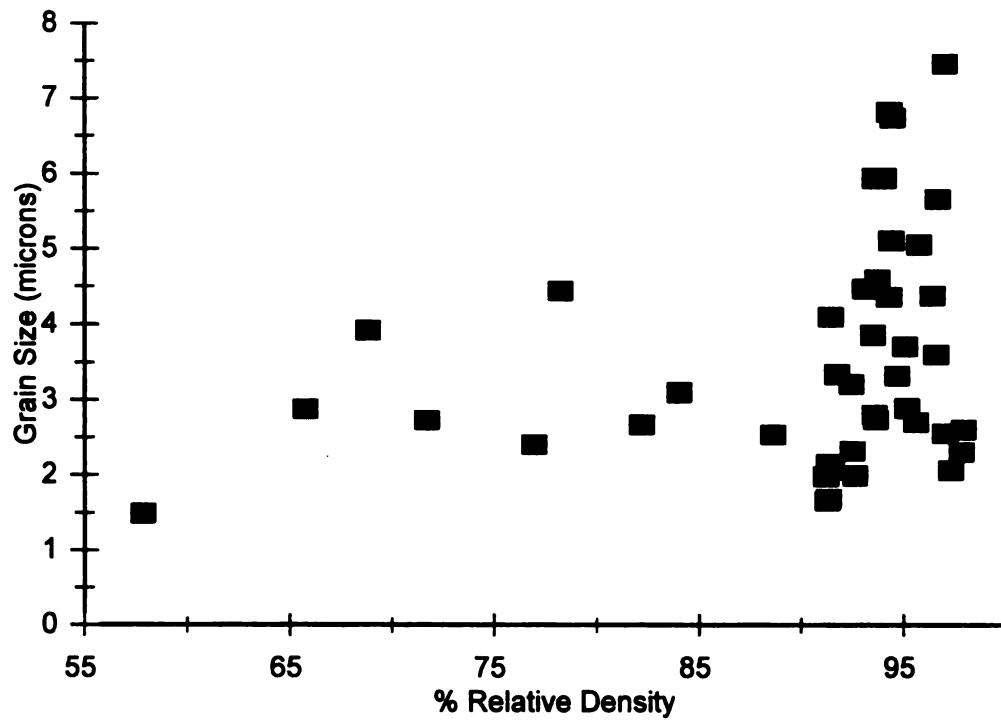


Figure 3-5 Grain size as a function of percent relative density for sintered hydroxyapatite. The data was taken from a subset of the data presented in Table 3-1.

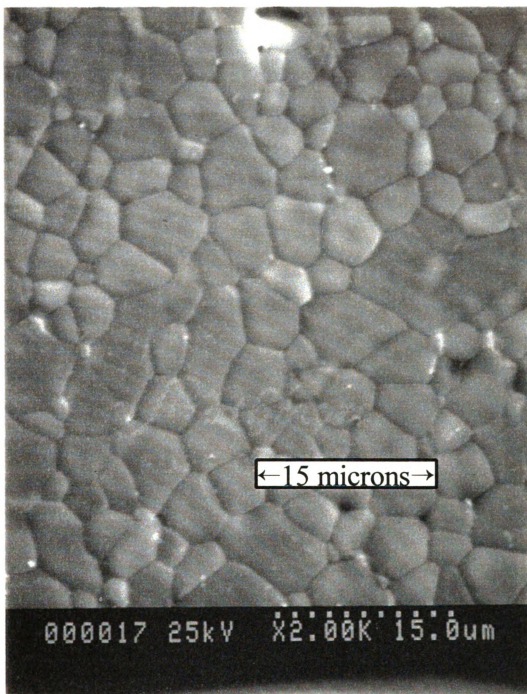


Figure 3-6 Micrographs of polished and thermally etched surface of sintered hydroxyapatite specimen number 15 sintered at 1300°C for 45 minutes, average grain size = 3.60 microns.

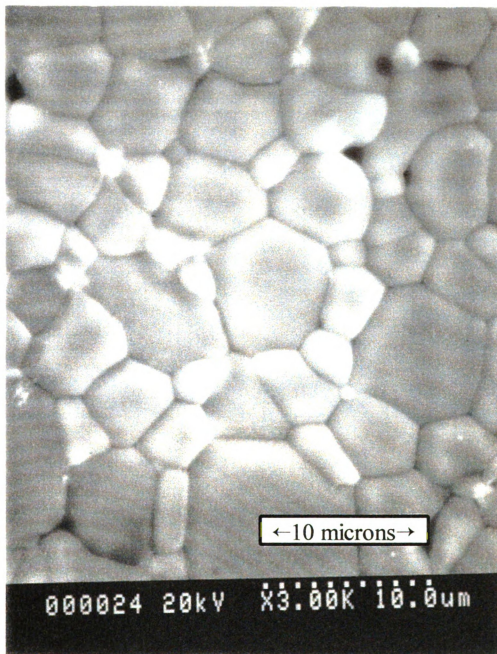


Figure 3-7 Micrograph of polished and thermally etched surface of sintered hydroxyapatite specimen number 45 sintered at 1350° C for 60 minutes, average grain size = 4.59 microns.

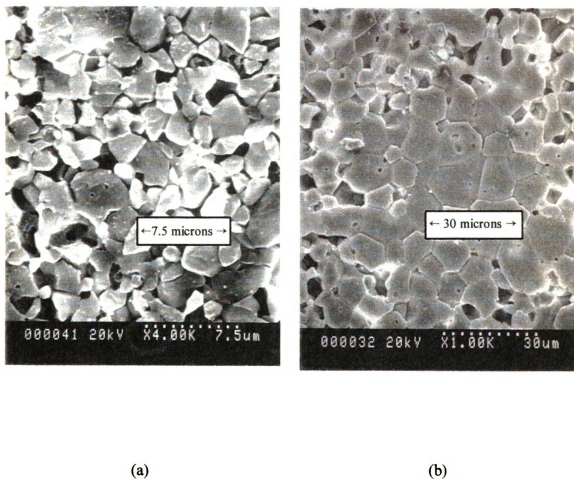


Figure 3-8 Micrographs of polished and acid etched surface of sintered hydroxyapatite (0.1 M HCl for 1 minute), (a) specimen number 3 sintered at 1300° C for 45 minutes, grain size = 1.98 microns, (b) specimen number 8 sintered at 1400° C degrees for 240 minutes, grain size = 7.44 microns.

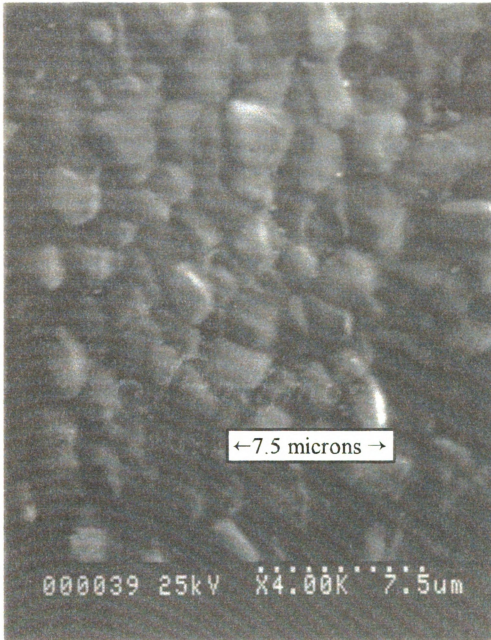


Figure 3-9 Polished and thermally etched surfaces of cold isostatically pressed (250 MPa) and sintered hydroxyapatite specimen number 22 sintered at 1200<sup>o</sup> C for 15 minutes. Average grain size = 1.99  $\mu$ m

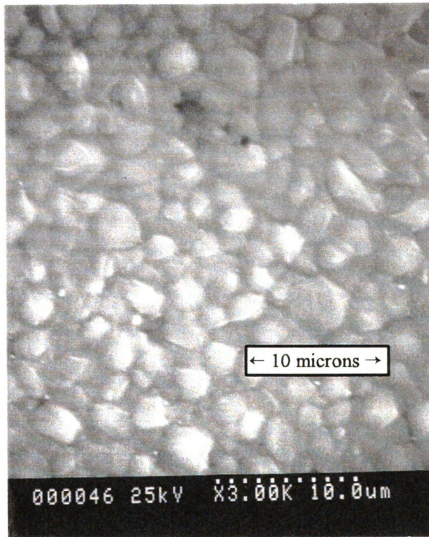


Figure 3-10 Polished and thermally etched surfaces of cold isostatically pressed (250 MPa) and sintered hydroxyapatite specimen number 23 sintered at 1250°C for 30 minutes. Average grain size = 2.06  $\mu\text{m}$

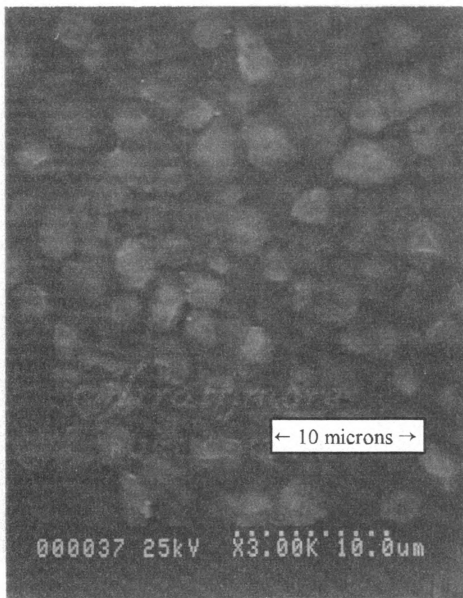


Figure 3-11 Polished and thermally etched surfaces of cold isostatically pressed (250 MPa) and sintered hydroxyapatite specimen #20 sintered at 1300°C for 15 minutes. Average grain size = 2.30  $\mu\text{m}$

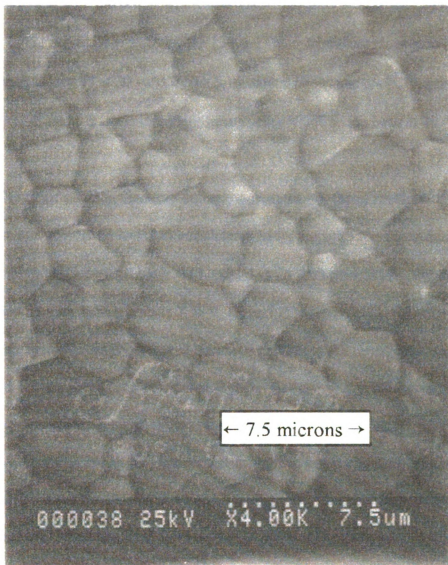


Figure 3-12 Polished and thermally etched surfaces of cold isostatically pressed (250 MPa) and sintered hydroxyapatite specimen number 21 sintered at 1300°C for 120 minutes., Average grain size = 2.60  $\mu\text{m}$ .

products of hydroxyapatite exist. According to the Powder Diffraction File for Inorganic Phases [68] the three main peaks for hydroxyapatite are at  $2\theta = 31.8^\circ$  for  $\{211\}$ ,  $2\theta = 32.2^\circ$  for  $\{112\}$  and at  $2\theta = 33.0^\circ$  for the  $\{300\}$ . The  $\alpha$ -tricalcium phosphate ( $\alpha$ -TCP) primary peak is located at  $2\theta = 30.7^\circ$ , the  $\beta$ -tricalcium phosphate ( $\beta$ -TCP), primary peak is at  $2\theta = 31.0^\circ$  and the tetracalcium phosphate primary diffraction peak at  $2\theta = 28.9^\circ$  [68].

The major peaks in the x-ray diffraction patterns, for the as received hydroxyapatite powder (Raw HAP) and sintered hydroxyapatite specimens numbers 4-12, are those of hydroxyapatite (Figure 3-13 and 3-14). A faint peak at  $2\theta \sim 29^\circ$  for hydroxyapatite specimens (numbers 7, 8, 9, 11, and 12) is associated with tetracalcium phosphate. Tetracalcium phosphate is the minor product of the decomposition reaction by a factor of 1:2 compared to tri-calcium phosphate (Equation 1-2). Tri-calcium phosphate was not detected in the sintered hydroxyapatite specimens by x-ray diffraction.

A decrease of the lattice parameter  $c_0$  is noted in sintered hydroxyapatite specimens as the sintering temperature and sintering time increases (Table 3-2). The lattice parameter were calculated from the angles of the three major x-ray diffraction peaks of the hydroxyapatite specimens (Figures 3-13 and 3-14) using Equation 2-2 and 2-3. The lattice parameter  $c_0$  was determined by averaging the lattice parameter  $c_0$  calculated from the diffraction peak for the  $\{211\}$  plane at  $2\theta = 31.8^\circ$  and the diffraction peak for the  $\{112\}$  plane at  $2\theta = 32.2^\circ$ . The lattice parameter  $a_0$  was calculated using the peak for the  $\{300\}$  plane at  $2\theta = 33.0^\circ$ .

Sintered hydroxyapatite specimens numbers 4-12 are composed of hydroxyapatite with no evidence of decomposition.

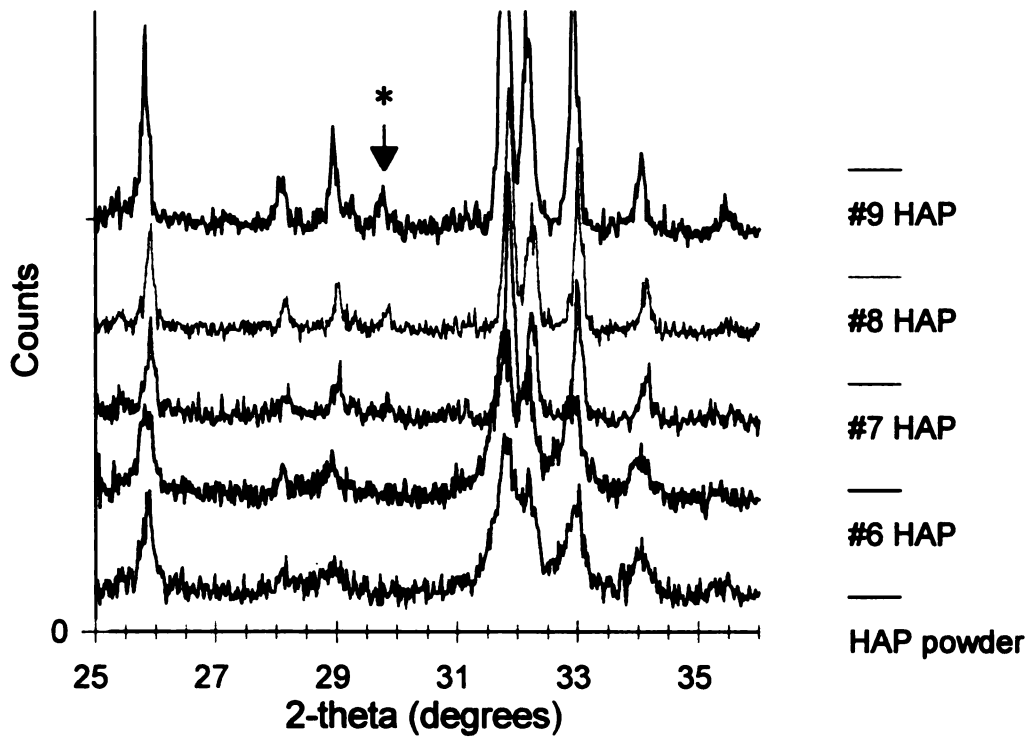


Figure 3-13 X-ray diffraction pattern ( $\text{Cu K}_{\alpha 1}$  radiation) for as received (Raw) and sintered hydroxyapatite (HAP). Specimens number 6 and 9 sintered at  $1300^{\circ}\text{C}$  for 240 and 300 minutes respectively. Specimens number 7 and 8 sintered at  $1400^{\circ}\text{C}$  for 120 and 240 minutes respectively. \* Primary tetra-calcium phosphate diffraction peak.

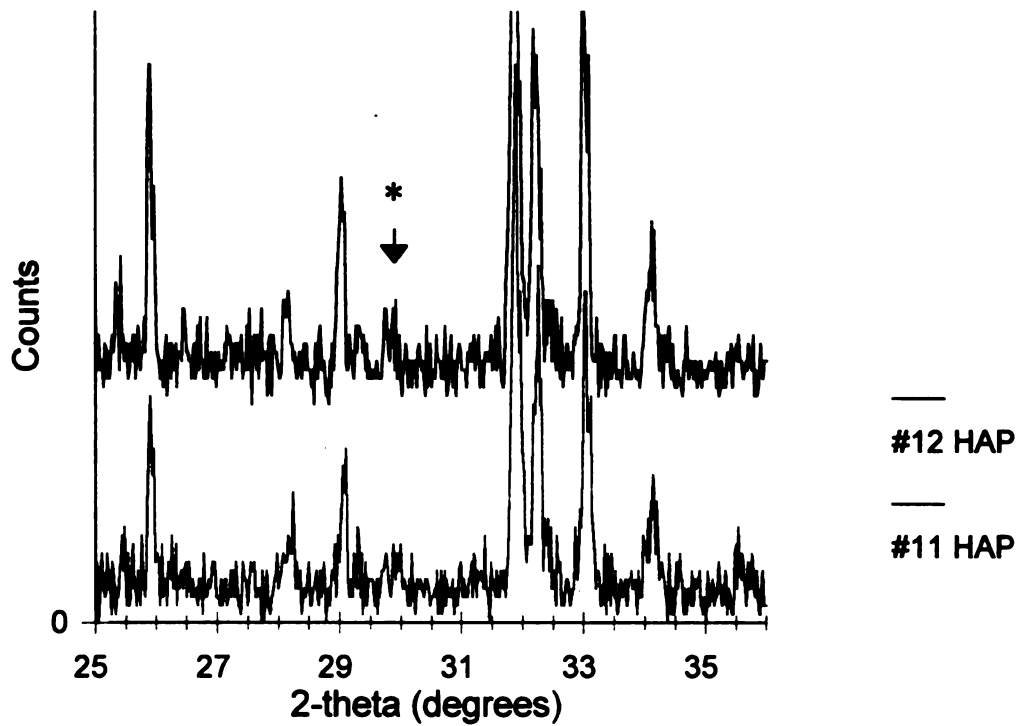


Figure 3-14 Additional x-ray diffraction patterns (Cu  $K_{\alpha 1}$  radiation) for sintered hydroxyapatite. Specimen #11 and #12 sintered at 1300<sup>o</sup> C for 540 and 660 minutes respectively. \* Primary and secondary tetra-calcium phosphate diffraction peaks.

Table 3-2 Lattice parameter data for the as received hydroxyapatite powder (HAP I) and sintered hydroxyapatite, calculated using the 3 major hydroxyapatite peaks from Figures 3-13 and 3-14 and Equations 2-2 and 2-3. Data from the handbook is included [69].

Specimen label	Sintering time (min.)	Sintering temperature (°C)	$a_o$ (nm)	$c_o$ (nm)
HAP I	0	-----	0.9389	06943
6	120	1300	0.9406	0.6892
9	300	1300	0.9411	0.6903
10	420	1300	0.9406	0.6857
11	540	1300	0.9384	0.6877
12	660	1300	0.9400	0.6868
7	120	1400	0.9400	0.6860
8	240	1400	0.9400	0.6859
Average	-----	-----	0.9400	0.6882
PDF [69]	File #9-432	-----	0.9418	0.6884

### 3.2 Indentation measurements

Hardness and fracture toughness of the sintered hydroxyapatite specimens were measured by the Vickers indentation method (Table 3-3).

#### 3.2.1 Vickers hardness

Vickers hardness of the sintered hydroxyapatite specimens prepared in this study are a strong function of the density (Figure 3-15). As a function of the average grain size the hardness values of the sintered hydroxyapatite specimens show no trends indicating that grain size effects on hardness are significantly weaker than the porosity effects on hardness, over the range of grain sizes and porosity values for the specimens in this study (Figure 3-16). There are no discernable patterns in the standard deviation (of the 7-10

Table 3-3 Density, grain size and the mechanical properties of hardness and toughness, measured by indentation technique, of sintered hydroxyapatite. The standard deviations ( $\sigma$ ), calculated for the multiple indentations per specimen, are included.

Specimen label	%Relative density	Grain size $\times 10^{-6}$ m	Hardness GPa	$\sigma$ Hardness GPa	Fracture toughness MPa(m <sup>1/2</sup> )	$\sigma$ Fracture toughness MPa(m <sup>1/2</sup> )
1	91.4	1.68	3.543	0.274	1.125	0.266
2	91.3	1.65	3.333	0.248	1.233	0.238
3	91.2	1.98	2.792	0.234	1.466	0.231
4	91.5	2.07	3.758	0.432	1.017	0.294
5	91.4	2.14	3.774	0.515	1.006	0.187
6	92.5	2.32	3.326	0.281	1.209	0.204
7	96.6	5.65	4.816	0.551	0.794	0.259
8	97.0	7.44	4.840	0.189	0.479	0.037
9	94.0	5.93	4.145	0.245	0.715	0.140
10	93.6	5.93	3.671	0.150	0.833	0.354
11	94.4	6.73	4.197	0.206	0.732	0.104
12	94.2	6.80	4.428	0.351	0.701	0.144
13	96.4	4.37	3.948	0.660	1.017	0.230
14	95.1	3.70	3.935	0.694	1.027	0.290
15	96.6	3.60	4.446	0.421	0.877	0.149
16	93.6	2.74	3.809	0.165	0.928	0.111
17	91.4	4.09	4.154	0.647	0.789	0.275
18	94.4	5.10	4.347	0.427	0.773	0.182
19	90.0	N/A	3.999	0.229	0.803	0.157
20	97.9	2.30	5.52	0.214	0.450	0.050
21	97.9	2.60	5.42	0.179	0.37	0.066
22	92.6	1.99	3.55	0.471	1.05	0.236

Table 3-3 continued

Specimen label	%Relative density	Grain size $\times 10^{-6}\text{m}$	Hardness GPa	$\sigma$ Hardness GPa	Fracture toughness $\text{MPa}(\text{m}^{1/2})$	$\sigma$ Fracture Toughness $\text{MPa}(\text{m}^{1/2})$
23	97.3	2.06	5.21	0.191	0.63	0.160
24	78.2	4.44	1.32	0.323	2.11	0.439
25	71.7	2.73	0.91	0.165	2.49	0.259
26	84.0	3.09	2.46	0.379	2.07	0.397
27	93.5	3.85	4.48	0.451	0.76	0.141
28	94.3	4.36	4.07	0.259	0.73	0.089
31	95.7	5.05	5.24	0.222	0.60	0.083
32	N/A	4.79	5.23	0.266	0.38	0.068
34	97.0	2.54	5.54	0.258	0.59	0.070
35	95.6	2.70	5.33	0.237	0.97	0.119
37	68.8	3.92	1.20	0.136	1.84	0.721
39	88.6	2.54	3.68	0.182	1.50	0.161
40	82.2	2.67	1.61	0.106	2.34	0.309
41	76.9	2.40	1.60	0.063	2.67	0.242
42	93.6	2.80	4.15	0.347	0.872	0.166
43	94.7	3.31	4.44	0.336	1.25	0.369
44	95.2	2.89	5.37	0.262	0.695	0.051
45	93.7	4.59	3.77	0.293	0.996	0.152
48	91.4	N/A	4.20	0.176	0.790	0.062
49	92.4	3.21	4.20	0.309	0.868	0.122
50	93.1	4.46	3.08	0.109	1.45	0.319

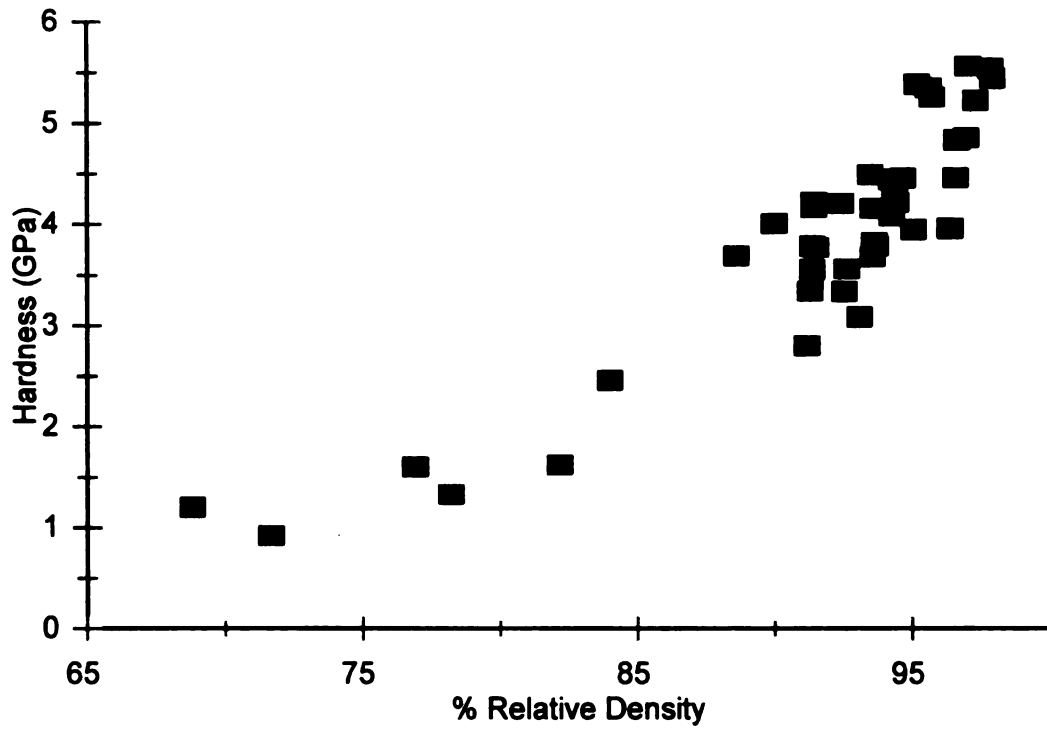


Figure 3-15 Vickers indentation Hardness values for sintered hydroxyapatite as a function of density. The data was taken from Table 3-3.

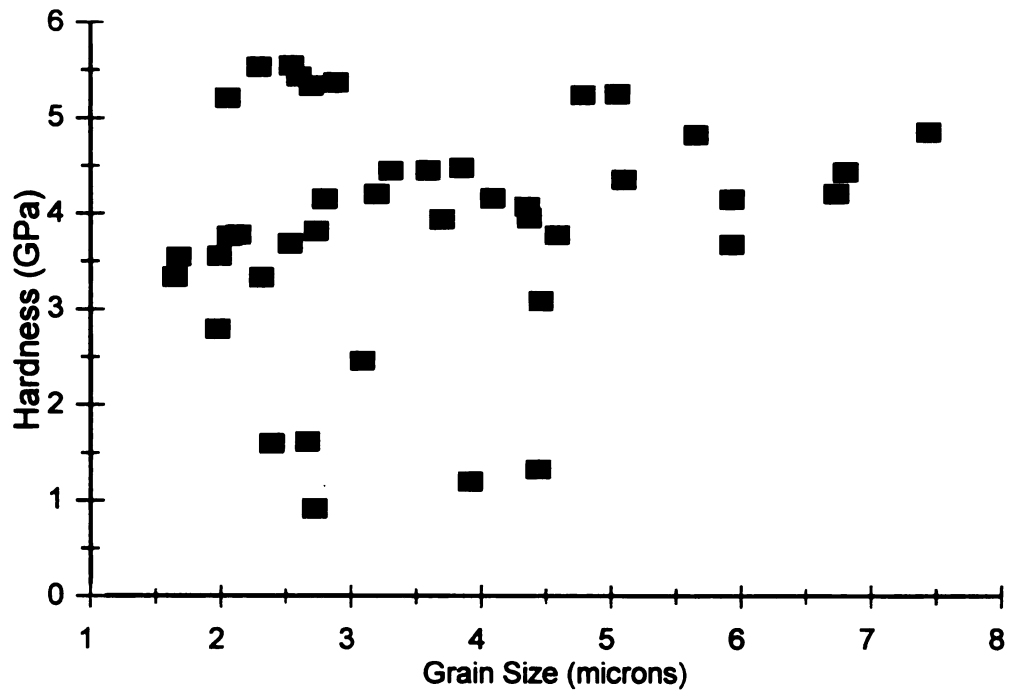


Figure 3-16 Vickers Hardness plotted against the average grain size of the sintered hydroxyapatite. The data was taken from Table 3-3.

hardness measurements per specimen) as a function of grain size (Figures 3-17).

### **3.2.2 Indentation fracture toughness**

Fracture toughness of the sintered hydroxyapatite specimens were measured to be 0.4 - 0.6 MPa m<sup>1/2</sup> at ~ 97% relative density. The fracture toughness of the sintered hydroxyapatite specimens increases markedly, to 2.5-2.7 MPa m<sup>1/2</sup>, as the density decreases to between 72 and 77% relative density (Figure 3-18). A plot of the fracture toughness as a function of the grain size shows no trend over the grain size range of the specimens in this study (Figure 3-19). Standard deviation of the fracture toughness measurements plotted against the specimen's average grain size shows no trend (Figure 3-20).

The ratio between the indentation crack length (c) and the indentation diagonal (a), as a function of relative density, increases as the density increases for the sintered hydroxyapatite specimens in this study (Figure 3-21). The trend for the c/a ratio as a function of relative density shows that the cracks barely extend beyond the indent for percent relative density below 85%.

### **3.3 Hardness and microstructure comparisons with literature data**

All of the Vickers hardness data of the sintered hydroxyapatite specimens from this study (indentation loads of 0.3 kg, 0.5 kg and 1 kg), and selected Vickers hardness data from Lu et al. (indent load 0.05 kg) [74], and Best et al. (indent load 1 kg) [75] along with selected Knoop hardness data from Wang et al. (0.2 kg load) [9] and Slosarczyk (no load specified) [11] all show substantial decreases in hardness as the porosity increases

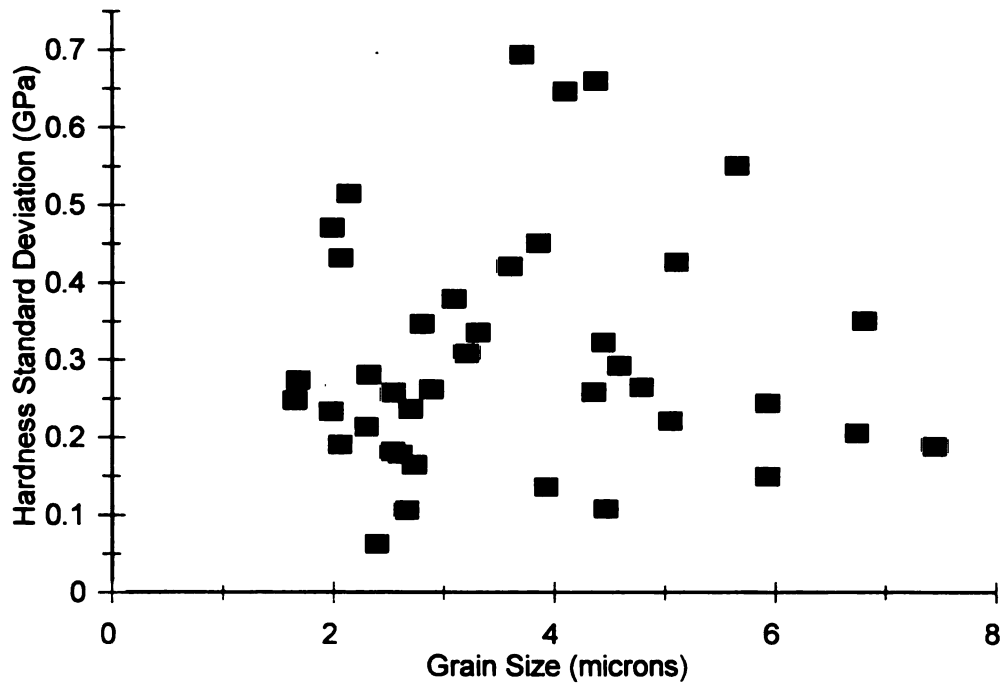


Figure 3-17 Statistical standard deviation of the Vickers hardness of sintered hydroxyapatite plotted against the average grain size. The data was taken from Table 3-3.

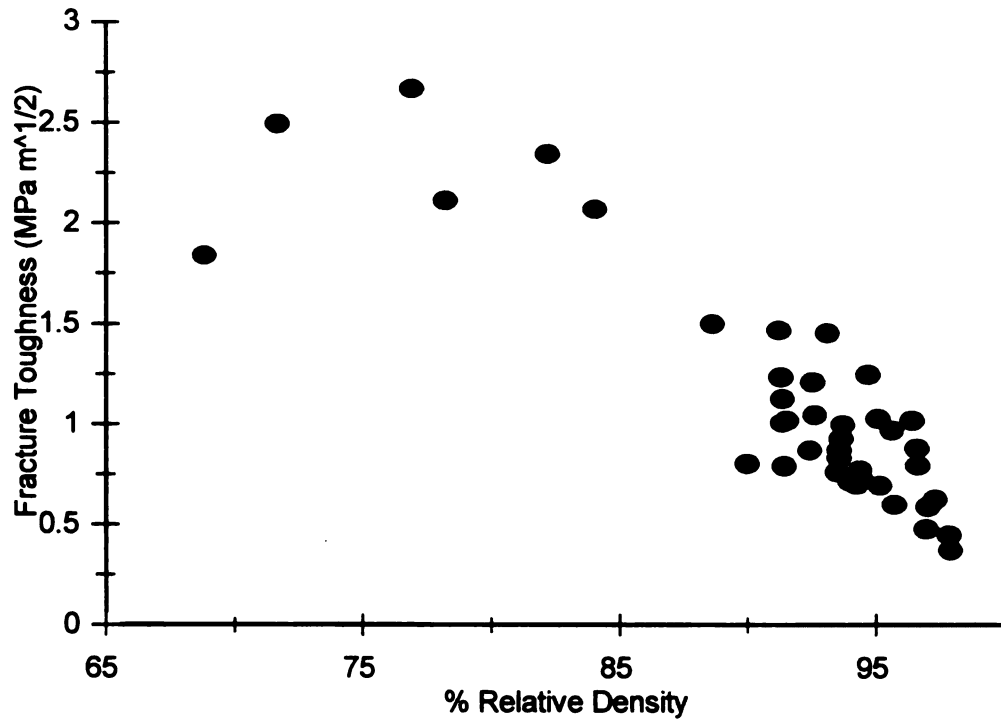


Figure 3-18 Vickers indentation toughness as a function of density for sintered hydroxyapatite. The data was taken from Table 3-3.

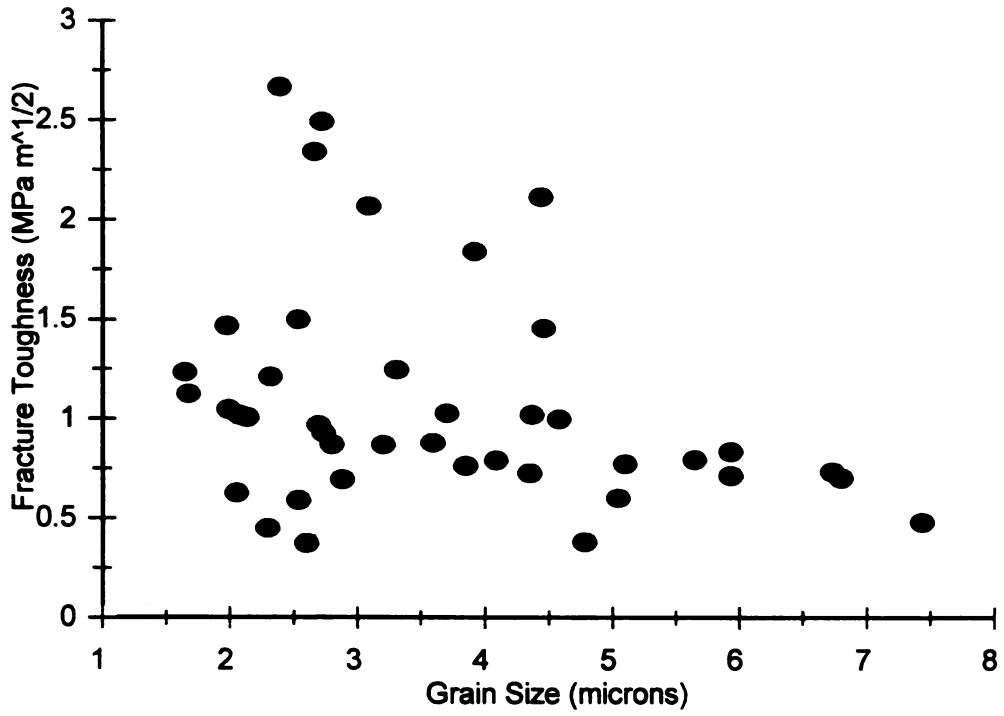


Figure 3-19 Fracture toughness as a function of average grain size of sintered hydroxyapatite. The data was taken from Table 3-3.

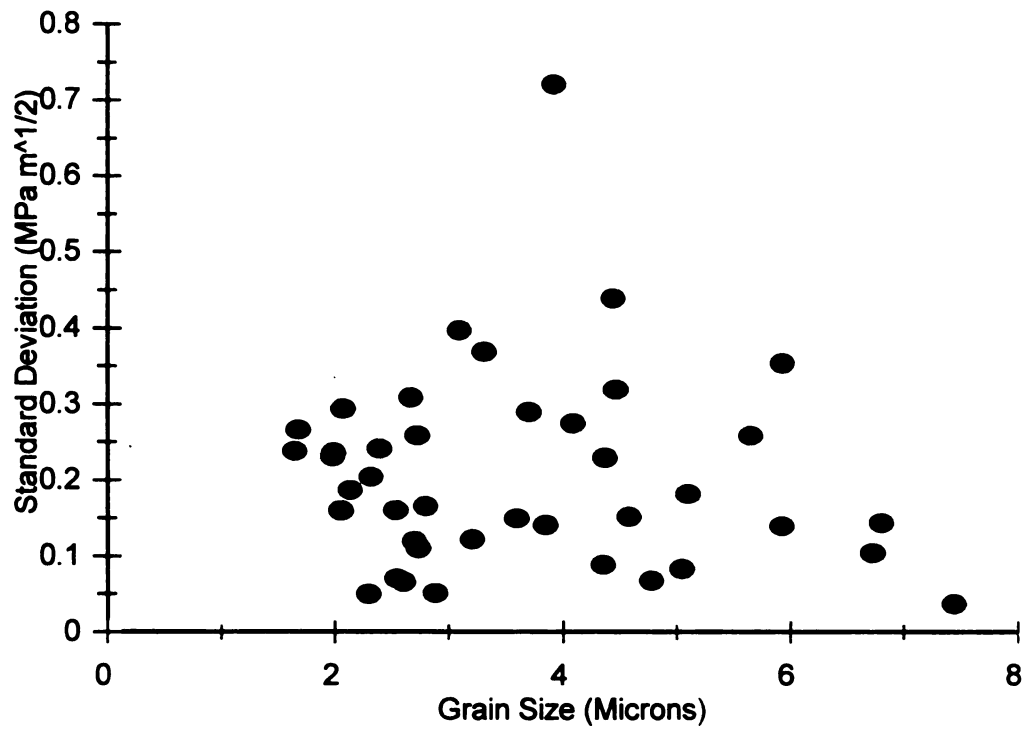


Figure 3-20 Standard deviation of the fracture toughness plotted against the average grain size of the sintered hydroxyapatite. The data was taken from Table 3-3.

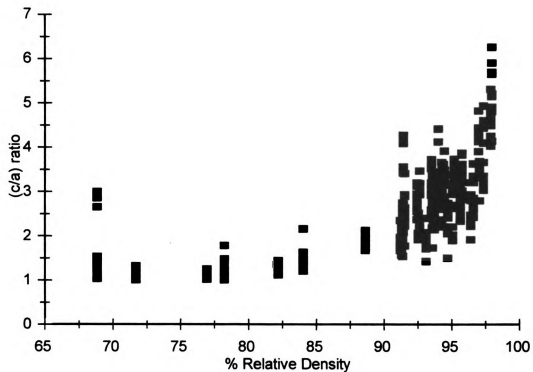


Figure 3-21 Ratio of the Vickers indentation crack length and Vickers indentation diagonal plotted against the % relative density, for all 410 indents on the specimens with known density measured in this study.

(Table 3-4). The selection criteria for the hardness data, from the literature, limited the data to those specimens proved by x-ray diffraction to contain no more than trace amounts of the decomposition phases of hydroxyapatite.

The hardness data of sintered hydroxyapatite, from this study (Table 3-3) and the hardness data from the studies by Wang et al. [9], Slosarczyk et al. [11], Best et al. [75], and Lu et al. [74] (Table 3-4), were linearized using the model proposed by Rice [57] (Equation 3-1)

$$\ln H = \ln H_0 - bP \quad (3-1)$$

where H is the measured hardness,  $H_0$  is the zero porosity hardness, and b is the slope of the plot of the logarithm of hardness (H) versus volume fraction porosity (P) (see Equation 1-8 in section 1.6). Linear regression analysis (Quattro pro) of the linearized data was used to calculate the zero porosity intercept  $H_0$  and the b value (Table 3-4). The hardness data and the linear fit of the hardness data was then normalized by dividing the measured hardness by the zero porosity hardness ( $H_0$ ). The data for Wang et al. and [9] Slosarczyk et al. [11] were linearized and normalized together due to the conformity of the two data sets. The normalized data and the normalized linear fit of the hardness data shows that the data from this study compares favorably to the data from Best et al. [75], and Wang et al. [9] Slosarczyk et al. [11] as a function of the volume fraction porosity (Figure 3-22). The hardness values from Lu et al. [74] decreases at a significantly greater rate as a function of the volume fraction porosity than the rest of the plotted data.

Hydroxyapatite powder used in preparing the specimens for Wang et al. [9], and Slosarczyk et al. [11] was synthesized by a wet chemical-method. Lu et al. [74] prepared two separate hydroxyapatite powders using the wet chemical method by heat drying part

Table 3-4 The normalization and statistical parameters from the linear regression analysis of the hardness as a function of volume fraction porosity (Equation 3-1:  $\ln H = \ln H_0 - bP$ ) for this study, Wang et al. [9], Slosarczyk et al. [11], Best et al. [70], and Lu et al. [69]. Actual hardness data [9,11,69,70] from the literature is included.

Linear fit parameters calculated from the hardness data in this study (Table 3-3)					
b = 6.03					
$r^2 = 0.907$					
Standard error** = 0.131					
Calculated zero porosity hardness $H_0 = 6.00 \pm 0.79$ Gpa					
Wang et al. [9] and Slosarczyk et al. [11] Data from tables		Best et al. [70] Data from graphs		Lu et al. [69] Data from graphs	
b = 7.38		b = 4.89		b = 19.4	
$r^2 = 0.892$		$r^2 = 0.947$		$r^2 = 0.969$	
Standard error** = 0.379		Standard error** = 0.244		Standard error** = 0.125	
$H_0 = 5.18 \pm 1.96$ GPa		$H_0 = 552.9 \pm 135$		$H_0 = 1218.4 \pm 152$	
Volume fraction porosity (P)	Knoop hardness $H_k$ (GPa)	Volume fraction porosity (P)	Vickers hardness $H_v$ Unitless	Volume fraction porosity (P)	Vickers hardness $H_v$ Unitless
0.40	0.449	0.52	50	0.12	125
0.39	0.155	0.50	50	0.11	128
0.38	0.189	0.49	50	0.05	560
0.35	0.298	0.48	51	0.05	580
0.31	0.85	0.18	145	0.04	605
0.31	0.849	0.16	350	0.04	648
0.24	0.928	0.11	205	0.03	660

\*\* Standard error of the normalized hardness (H/H<sub>0</sub>)

Table 3-4 continued

Wang et al. [W] and Slosarczyk et al. [S] Data from tables		Best et al. [B] Data from graphs		Lu et al. [L] Data from graphs	
Volume fraction porosity (P)	Knoop hardness $H_k$ (GPa)	Volume fraction porosity (P)	Vickers hardness $H_v$ Unitless	Volume fraction porosity (P)	Vickers hardness $H_v$ Unitless
0.23	0.963	0.09	370	0.03	680
0.22	1.025	0.06	425	0.02	758
0.08	2.7*	0.05	410	0.01**	805**
0.02	4.0*	0.03	410		
0.01	4.6*	0.03	450		
		0.02	700		
		0.02	670		
		0.01	540		

- \* Hardness data from Slosarczyk et al. [S]
- \*\* Trace of TCP in x-ray diffraction spectra.

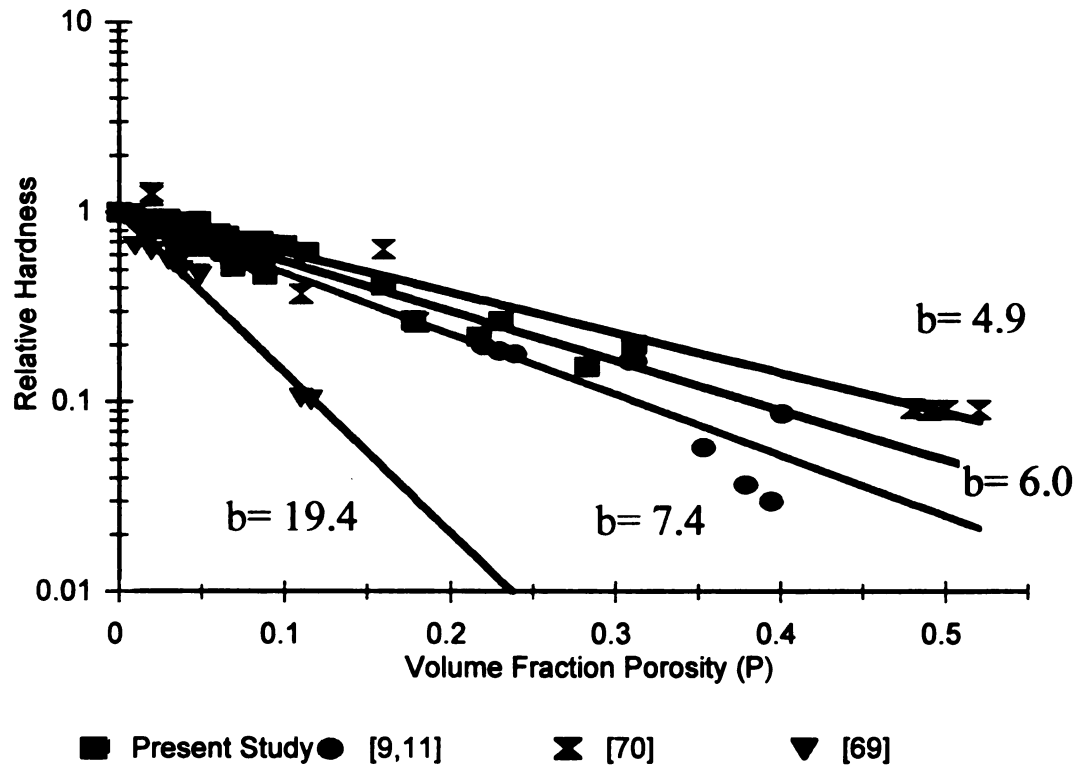


Figure 3-22 Log relative indentation Hardness values for sintered hydroxyapatite plotted against the volume fraction porosity along with the solutions for the linear log relative hardness as a function of volume fraction porosity (Equation 1- 8, Section 1.6). Data was taken from Table 3-3 for the present study and Table 3-4 for the literature data.

of the mixture of HAP and water, and freeze drying the rest. Hardness data from specimens produced from both powders by Lu et al. [74] were lumped together for analysis (Table 3-4). Three commercial hydroxyapatite powders, used by Best et al. [75], were characterized by x-ray diffraction, infrared spectroscopy, inductively coupled plasma spectroscopy, surface area analysis, particle size analysis and scanning electron microscopy, before being sintered. The three commercial powders were found to have significantly different morphologies which influenced the sintered density and grain size of the sintered specimens [75]. Hardness data from specimens sintered from all three commercial powders were included in this analysis (Table 3-4).

The resultant microstructures of the sintered hydroxyapatite specimens compiled in table 3-4 included grain sizes of 2-8  $\mu\text{m}$  this study, 5-10  $\mu\text{m}$  [11,74], to 90  $\mu\text{m}$  [9]. Grain sizes of the final sintered specimens were not specified by Best et al. [75].

The data from this study is in good agreement with the four different studies [9,11,74,75]. Indentation hardness of sintered hydroxyapatite decreases exponentially as porosity increases, as modeled by equation 1-8, regardless of the origin and morphology of the starting powder.

#### **3.4 Fracture toughness and microstructure comparisons with literature data**

Fracture toughness studies of sintered hydroxyapatite show a decrease in the fracture toughness values as the porosity increases when measured by three point bend [54], and the indentation method [56] (Table 3-5). The fracture toughness of sintered hydroxyapatite specimens, in this study, increased in fracture toughness as the porosity increases (Figure 3-23). The fracture toughness of the whisker reinforced sintered

Table 3-5 The normalization and statistical parameters from the linear regression analysis of toughness as a function of volume fraction porosity (Equation 3-2:  $\ln K_{IC} = \ln K_{ICo} - b P$ ) for this study, DeWith et al. [54] and Suchanek et al. [56]. Fracture toughness data from DeWith et al. [54] and Suchanek et al. [56] are included.

Linear fit parameters from the fracture toughness data in this study (Table 3-1)			
b = -5.51			
$r^2 = 0.657$			
Standard error** = 0.270			
Calculated zero porosity fracture toughness $K_{ICo} = 0.61 \pm 0.16 \text{ MPa m}^{1/2}$			
DeWith et al. [54] Data from graph		Suchanek et al. [56] Data from graph	
b = 2.786		b = 2.812	
$r^2 = 0.630$		$r^2 = 0.786$	
Standard error** = 0.202		Standard error** = 0.116	
$K_{ICo} = 1.14 \pm 0.23 \text{ MPa m}^{1/2}$		$K_{ICo} = 1.63 \pm 0.19 \text{ MPa m}^{1/2}$	
Volume fraction porosity (P)	Fracture Toughness (MPa m <sup>1/2</sup> )	Volume fraction porosity (P)	Fracture Toughness (MPa m <sup>1/2</sup> )
0.27	0.65	0.29	0.78
0.27	0.6	0.16	1.00
0.22	0.64	0.11	1.10
0.22	0.35	0.10	1.05
0.18	0.66	0.08	1.36
0.18	0.81	0.08	1.41
0.1	0.93	0.05	1.32
0.1	0.88	0.04	1.54
0.06	0.98	0.03	1.34
0.06	0.93	0.02	2.00

\*\* Standard error of the normalized fracture toughness ( $K_{IC} / K_{ICo}$ )

Table 3-5 continued

DeWith et al. [54] Data from graph		Suchanek et al. [56] Data from graph	
Volume fraction porosity (P)	Fracture Toughness (MPa m <sup>1/2</sup> )	Volume fraction porosity (P)	Fracture Toughness (MPa m <sup>1/2</sup> )
0.03	1.08	0.02	1.45
0.03	1.01	0.02	1.65
		0.01	1.48
		0.01	1.44
		0.01	1.82
		0.01	1.72

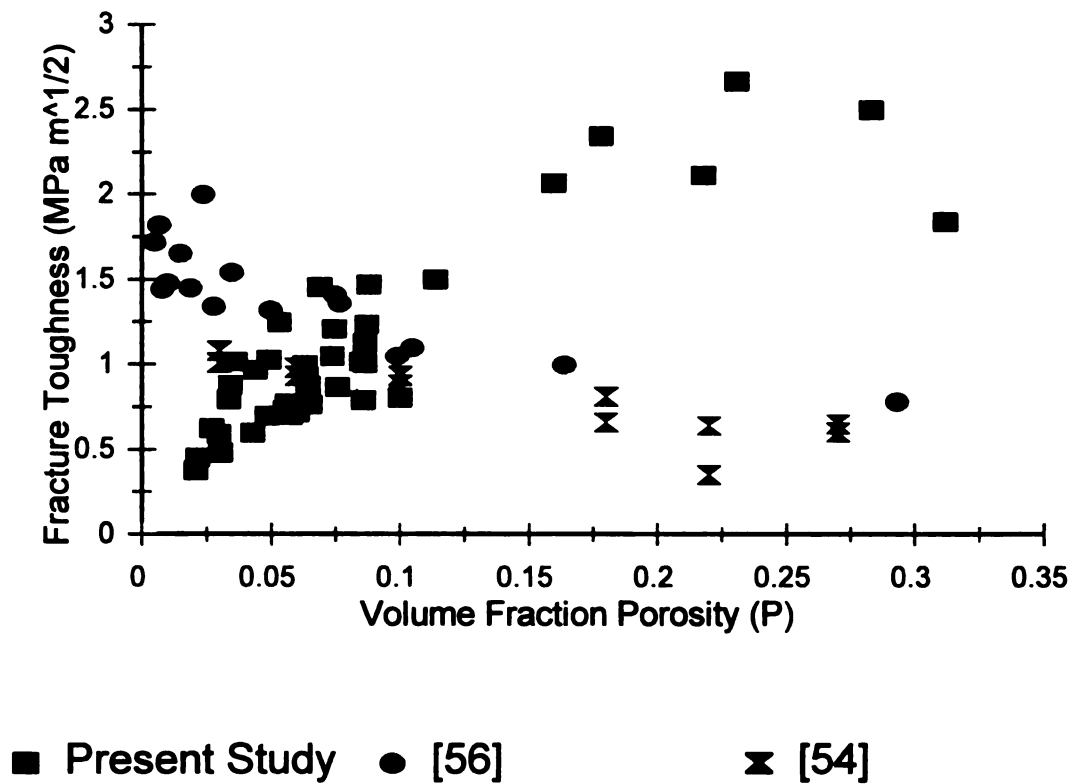


Figure 3-23 Fracture toughness values for sintered hydroxyapatite plotted against the volume fraction porosity. Fracture toughness values were taken from Table 3-3 (present study) and Table 3-5 for the data from Suchanek et al. [56] and DeWith et al. [54].

hydroxyapatite, prepared by Suchanek et al [56] is greater than the fracture toughness, as a function of the porosity, of the over the non-reinforced specimens prepared by DeWith et al. [54] (Figure 3-23).

The fracture toughness data from DeWith et al. [54], Suchanek et al. [56] and this study were linearized and normalized in the same way as the hardness data (section 3.3).

$$\ln K_{\text{ic}} = \ln K_{\text{ic}0} - b P \quad (3-2)$$

where  $K_{\text{ic}}$  is the measured fracture toughness,  $K_{\text{ic}0}$  is the zero porosity fracture toughness, and  $b$  is the slope of the plot of the logarithm of fracture toughness ( $K_{\text{ic}}$ ) versus volume fraction porosity ( $P$ ) (see Equation 1-8 in section 1.6). The data (Table 3-5) from DeWith et al.[54] and Suchanek et al [56] have the same functional relationship to the volume fraction porosity, as determined by the  $b$  value (Figure 3-24, and Figure 3-25). The normalized and linearized data from this study was not linear and the calculated  $b$  value was negative, deviating from the MSA model (Figure 3-24, and Figure 3-25).

This study and the study by DeWith et al. [54] used commercially available powders (CERAC Inc., this study, and Merck A. G. [54]). Both studies have similar microstructures. The sintered grain sizes are 1-6  $\mu\text{m}$  for DeWith [54] and 2-8  $\mu\text{m}$  for this study. Porosity values were up to 0.30 volume fraction porosity for both studies. Traces of decomposition products were detected in specimens sintered at temperatures greater than 1150<sup>o</sup> C (relative densities > 85%) for DeWith et al. [54].

The indentation fracture toughness method used by Suchanek et al. [56], is similar to the fracture toughness measurement technique used for this study, however, the microstructures differ due to the whisker reinforcement in the sintered hydroxyapatite specimens tested by Suchanek et al. [56].

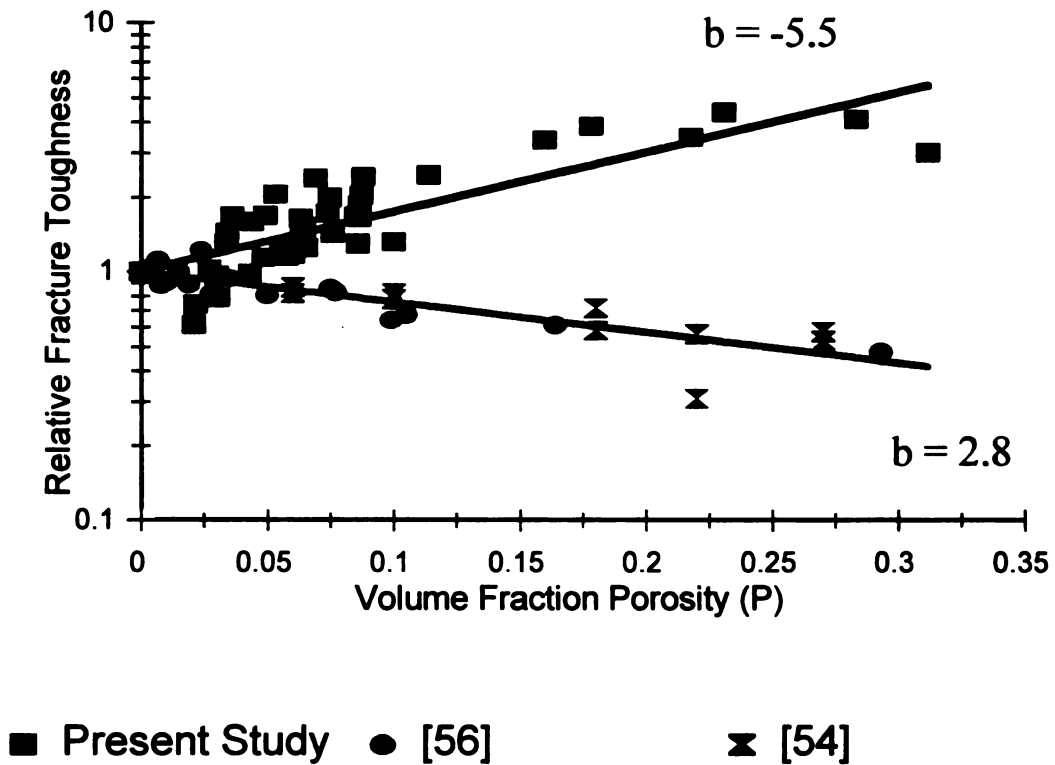
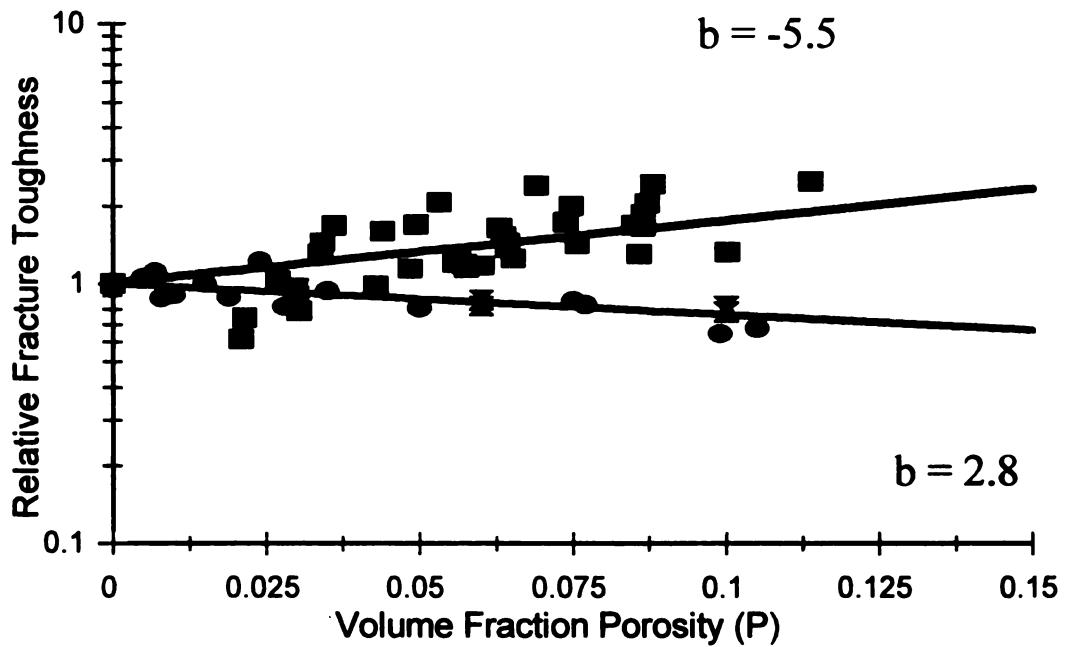


Figure 3-24 Relative fracture toughness values for sintered hydroxyapatite as a function of volume fraction porosity and the calculated linear fit. Linear fit parameters taken from Table 3-5 for the data from Table 3-3 (present study) and the fracture toughness data in Table 3-5 from Suchanek et al. [56] and DeWith et al. [54].



■ Present Study    ● [56]                      ▴ [54]

Figure 3-25 A section of lower volume fraction porosity of the relative fracture toughness values for sintered hydroxyapatite as a function of volume fraction porosity and the calculated linear fit. Linear fit parameters taken from Table 3-5 for the data from Table 3-3 (present study) and the fracture toughness data in Table 3-5 from Suchanek et al. [56] and DeWith et al. [54].

The studies by DeWith et al. [54] and Suchanek [56] are linked by the fact that the fracture toughness measurement techniques and sintered hydroxyapatite microstructure were vastly different yet the functional relationship between fracture toughness and volume fraction porosity is nearly identical.

Comparisons between the three studies leads to a three part argument, in which no conclusion can easily be drawn; 1) the starting HAP powders and sintered HAP microstructure are similar in this study and the study by DeWith et al. [54], yet the nearly fully dense (95-97% relative density) fracture toughness and the functional relationship between fracture toughness and porosity are vastly different. 2) the studies by DeWith et al. [54] and Suchanek et al. [56] are linked by a nearly identical b value calculated from the fracture toughness versus volume fraction porosity data (Equation 3-2) even with very different measurement methods and specimen microstructures. 3) the indentation fracture toughness techniques are shared by this study and Suchanek et al. [56], however the measured functional relationship between fracture toughness and porosity are incongruent.

### **3.5 Further comment on the fracture toughness of porous hydroxyapatite**

The significant and steady increase in the fracture toughness of the sintered hydroxyapatite specimens in this study as the porosity of hydroxyapatite specimens increases (Figure 3-18) requires further comment. The lack of evidence of secondary phase formation, from x-ray diffraction (section 3.1.4), the large sample population (42), and the increase of the fracture toughness as the density decreases, forces a focus on the fracture toughness as a function of porosity for the sintered hydroxyapatite specimens in this study.

The relationship among the microstructure of sintered hydroxyapatite, the indentation fracture toughness measurement and the measured fracture toughness of sintered hydroxyapatite consists of three major elements: 1) Applications of the indentation toughness equation (Equation 1-6) to porous ceramic materials. 2) The formation and growth of indentation cracks in porous hydroxyapatite specimens 3) Toughening mechanisms that are unaffected by the grain size, over the grain size range of the specimens in this study, and are increasingly effective for hydroxyapatite specimens in which the processing parameters produced higher porosities. The fracture toughness of near full density sintered hydroxyapatite, reported in the literature, is between 0.8-1.2 MPa m<sup>1/2</sup> [54,56,76], and is comparable to the average of the +90% dense specimens in this study ( $K_{Ic} = 0.77 \text{ MPa m}^{1/2}$ ).

### **3.5.1 Indentation toughness model and porosity**

The stress field of the test specimen under indentation loading is a function of the elastic modulus and Poisson's ratio of the test specimen, and the load and geometry of the indenter [38]. Indentation fracture toughness is calculated using the indentation stress field and the resultant indentation crack length (Figure 1-1 [42]) of the indented specimen [38]. The indentation toughness model, derived by fracture mechanics from the indentation stress and the indentation cracks [38], has successfully determined the fracture toughness for a wide variety of ceramic materials as a function of the hardness, elastic modulus and the indentation crack length [39,40,41] (Equation 3-3 [40]).

$$K_{Ic} = \zeta \left( \frac{E}{H_v} \right)^{1/2} \frac{P}{c^{3/2}} \quad (3-3)$$

where  $\zeta$  is the empirically determined constant ( $\zeta = 0.016$  [40]),  $E$  is the elastic modulus,  $H_v$  is the Vickers hardness determined from the size of the indent ( $H_v = P/2a^2$ , Equation 2-5),  $P$  is the indentation load, and  $c$  is the indentation crack length (from Figure 1-1, section 1.5.1). Equation 3-3 was used to calculate  $K_{Ic}$  for each indent in this study. The average and standard deviation of the specimen's  $K_{Ic}$  were then determined from the 7-10 indents/specimen.

The elastic modulus of ceramics decreases as the porosity increases [35,54,58,60]. The elastic modulus/porosity data has been fit to the MSA model ( $\ln(E) = \ln(E_0) - b_E P_p$ , Equation 1-8), where  $E_0$  is the fully dense elastic modulus,  $b_E$  is the material dependent constant and  $P_p$  is the volume fraction porosity [57] (Section 1.6). Poisson's ratio for sintered hydroxyapatite also decreases as the porosity increases [53,54]. The porosity dependence of Poisson's ratio is much weaker, as determined by the  $b$  values, than the porosity dependence on elastic modulus, for many ceramics (Table 3-6).

The fracture toughness values of the hydroxyapatite specimens in this study (Tables 3-3, 3-5, Figures 3-18, 3-19, 3-24, and 3-25) were calculated by equation 3-3 with fixed elastic modulus ( $E = 115$  GPa [56]).

The functional dependence of hardness, as measured by the size and load of the indent, on the volume fraction porosity of sintered hydroxyapatite has been measured in this study and fit to the MSA model [57] ( $\ln(H_v) = \ln(H_{v0}) - b_H P_p$  Section 3.3). The relationship between hardness and density indicates deformation processes behave as

Table 3-6 Porosity dependence of the elastic modulus compared to the porosity dependence of Poisson's ratio for experimental data fit to the MSA model ( $\ln E = \ln E_0 - b_E P$ ,  $\ln \nu = \ln \nu_0 - b_\nu P$ , Equation 1-8) by Rice [58].

Ceramic	P range (%)	$b_E$	$b_\nu$	$\nu_0$	Reference
Al <sub>2</sub> O <sub>3</sub>	15-55	2.8	0	0.27	Coble and Kingery from [58]
B <sub>6</sub> O	0-8	4.0	0	0.155	Petrak et al. from [58]
HAP	3-27	2.9	0.7	0.28	[54] fit in this study
AlN	0-20	5.5	0.9	0.24	Hunter et al. from [58]
HfN	5-15	5.2	0.6	0.26	Desmaison-Brut et al. from [58]
TaN	1-15	4.6	0.6	0.25	“ ”
TiN	1-22	3.0	0.2	0.22	“ ”
ZrN	2-8	3.3	0.8	0.26	“ ”
Graphite	13-32	3.5	1	0.31	Cost et al. from [58]

expected by the MSA model [57] for sintered hydroxyapatite.

Inserting the MSA functions (modifications of Equation 1-7) for the elastic modulus and Vickers hardness in equation 3-3 results in equation 3-4.

$$K_{lc}(E(P_p), H(P_p)) = \zeta \left( \frac{E_0 e^{-b_E P_p}}{H_0 e^{-b_H P_p}} \right)^{1/2} \frac{P}{c^{3/2}} \quad (3-4)$$

where  $E_0$  and  $H_{v0}$  are the fully dense values of elastic modulus and hardness,  $b_E$  and  $b_H$  are the material dependent constants (MSA fit [57]) for the elastic modulus and Vickers hardness respectively, and  $P_p$  is the volume fraction porosity. The material dependent constants  $b_E$  and  $b_H$  are obtained by fitting the modulus-porosity and the hardness-porosity data to the MSA model (Equation 1-8). Equation 3-4 is simplified by combining the exponents (Equation 3-5).

$$K_{lc}(E(P_p), H(P_p)) = e^{\frac{(b_H - b_E) P_p}{2}} \zeta \left( \frac{E_0}{H_0} \right)^{1/2} \frac{P}{c^{3/2}} \quad (3-5)$$

The effect of porosity on the elastic modulus/Vickers hardness ratio may be written as  $(E_0/H_{v0})^{1/2} \exp(1/2(b_H - b_E)P_p)$ .

Rice [58], applying existing literature data to the MSA model, compiled decay constants for the elastic modulus and hardness for a large variety of porous ceramics (Table 3-7). The effect of the porosity dependence on the hardness and elastic modulus (as related by  $b_E$  and  $b_H$ ), to Equation 3-5 with  $(P/c^{3/2})$  held constant, ranges from a factor

Table 3-7 Material dependent coefficients ( $b_H$  and  $b_E$ ) from the MSA model [57] for  $Al_2O_3$ ,  $B_4C$ ,  $AlN$  and  $SiO_2$  ceramics calculated by Rice [58]. The HAP (hydroxyapatite) elastic modulus attenuation coefficient was calculated for this study using DeWith et al.'s data [54]. The hardness attenuation coefficient for HAP has been determined previously in this study (Table 3-4).

Coefficient	$Al_2O_3$	$B_4C$	$AlN$	$SiO_2$	HAP
$b_E$	2.6	4.0	5.5	4.3	2.93*
$b_H$	6.3	5.3	7.7	3.2	6.03**
$\Delta b = b_H - b_E$	3.7	1.3	2.2	-1.1	3.1
[Reference]	Wu & Rice from [58]	Wu & Rice from [58]	Boch et al. from [58]	Park & Hench from [58]	*[54] **[this study]

2.10 for alumina ( $\Delta b = 3.7$ ) at 0.4 volume fraction porosity to a factor of 0.80 for  $\text{SiO}_2$  ( $\Delta b = -1.1$ ) at volume fraction porosity of 0.4 (Figure 3-26). The E/H coefficient for hydroxyapatite = 1.86 ( $\Delta b = 3.1$ ) at 0.40 volume percent porosity, was calculated by the hardness decay constant from the data in this study,  $b_H = 6.03$  (Table 3-4), and the elastic modulus decay constant  $b_E = 2.93$  calculated in this study from the sintered hydroxyapatite data from DeWith et al [54] (Table 3-7, Figure 3-26).

### 3.5.1.1 Effect of E(P) on the fracture toughness of sintered hydroxyapatite

A decrease in hardness with increasing porosity was observed for the sintered hydroxyapatite specimens in this study. The change in the Vickers hardness as porosity increases is included in the fracture toughness calculation, due to the hardness and fracture toughness values being calculated for each individual indent by Equation 3-3. Adding the elastic modulus-porosity function ( $E = E_0 e^{-b_E P_p}$ ) with decay constant  $b_E = 2.93$  determined by DeWith et al. [54] to equation 3-3 results in Equation 3-6.

$$K_{Ic}(E(P_p)) = E_0 e^{-\frac{1}{2} b_E P_p} \zeta \left( \frac{1}{H_v} \right)^{1/2} \frac{P}{c^{3/2}} \quad (3-6)$$

Recalculation of the fracture toughness of the sintered hydroxyapatite specimens in this study, using equation 3-6 and  $b_E = 2.93$  [54], decreases the fracture toughness relative to the fracture toughness calculated with equation 3-3. The corrected fracture toughness values, determined by  $K_{Ic}(E(P_p))$  (Equation 3-6), for the sintered hydroxyapatite

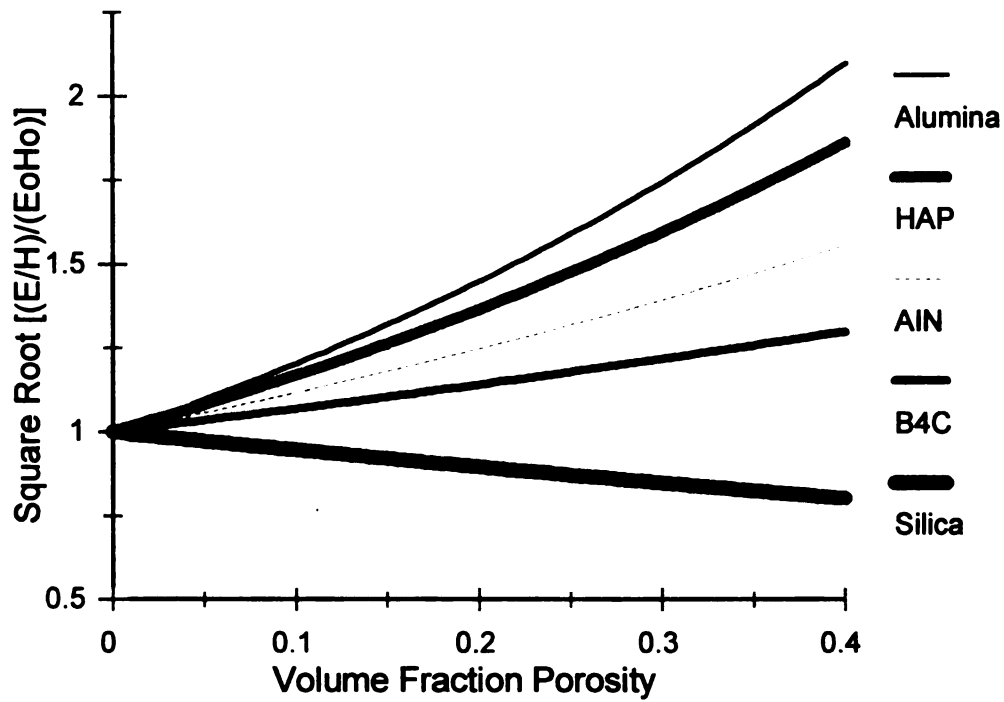


Figure 3-26  $(E/H)^{1/2}$  as a function of the volume fraction porosities normalized by  $(E_0/H_0)^{1/2}$ , the fully dense values of the elastic modulus and hardness respectively. The decay constants  $b_H$  and  $b_E$  are compiled by Rice [58] for  $Al_2O_3$ , AlN,  $B_4C$ , and  $SiO_2$  (Table 3-6). The  $b_H$  for HAP was determined in this study, while  $b_E$  for HAP was calculated in this study using the MSA model and DeWith et al.'s data [54] (Table 3-6).

specimens in this study more than double as the volume fraction porosity increases from 0.05 to 0.20 (Figure 3-27).

In addition to the effect of porosity the elastic modulus can be reduced by microcracking between grains in a polycrystalline ceramic caused by thermal expansion anisotropy [36,64,77]. The interactions between porosity and microcracking, and microcracking and fracture toughness are very complex and will be discussed among the possible toughening mechanisms in section 3.5.3.

### 3.5.1.2 Indentation fracture toughness of porous $\text{YBa}_2\text{Cu}_3\text{O}_{7-x}$

Tancret et al. [78] measured the mechanical properties of porous  $\text{YBa}_2\text{Cu}_3\text{O}_{7-x}$  high temperature superconductors. The high temperature superconducting specimens were prepared by cold isostatic pressing and pressureless sintering of commercial  $\text{YBa}_2\text{Cu}_3\text{O}_{7-x}$  powders [78]. The elastic modulus ( $E$ ), measured by three-point bending under quasi-static conditions, the fracture toughness ( $K_{Ic}$ ), measured by single edged notched beam (SENB), the Vickers hardness ( $H_V$ ), and the Vickers indentation crack parameter ( $P/c^{3/2}$ ) were recorded for specimen porosities between 5 and 31% (0.05-0.31 volume fraction porosity) and average grain sizes between 3 and 10  $\mu\text{m}$  (Table 3-8) [78].

The indentation crack parameter ( $P/c^{3/2}$ ) decreases as porosity increases for the  $\text{YBa}_2\text{Cu}_3\text{O}_{7-x}$  [78] (Figure 3-28). The indentation crack parameter ( $P/c^{3/2}$ ) for the sintered hydroxyapatite in this study is parabolic in shape peaking at  $\sim 1.7 \text{ MPa m}^{1/2}$  at 0.18 volume fraction porosity and falling at volume fraction porosities  $> 0.25$  (Figure 3-28). In this study, using Tancret et al.'s  $\text{YBa}_2\text{Cu}_3\text{O}_{7-x}$  data [78], the porosity dependence of the mechanical properties  $E$ ,  $K_{Ic}$ ,  $H_V$  and  $P/c^{3/2}$  were fit to the MSA model [57] (Table 3-8).

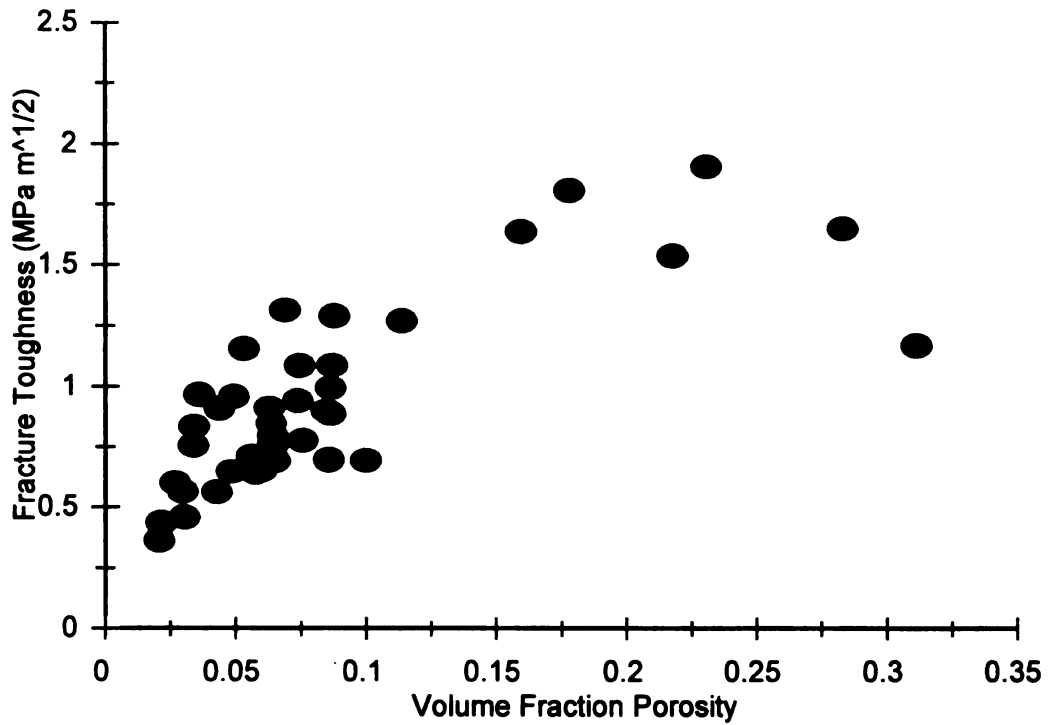


Figure 3-27 Calculated fracture toughness of the hydroxyapatite specimens in this study using the elastic modulus as function of volume fraction porosity  $\{K_{Ic}(E(P))\}$  (Equation 3-6, material dependent constant  $b_E = 2.93$  [54]).

Table 3-8 Experimental data for  $\text{YBa}_2\text{Cu}_3\text{O}_{7-x}$  from Tancret et al. [78] and the fit, for this study, to the MSA model  $\ln(A) = \ln(A_0) - b_A P_p$ , where A represents the property (E,  $H_v$ , etc.),  $A_0$  = the property at zero porosity (y-intercept for the linear regression),  $b_A$  is the slope of the log-linear relation, and  $P_p$  is the volume fraction porosity. Included for comparison are the fracture toughness values calculated, for each porosity, using equation 3-3  $\{K_{Ic} = \zeta(E/H)^{1/2} P c^{-3/2}\}$ , for this study. Column 6 contains the fracture toughness calculated with constant elastic modulus ( $E = 120$  GPa),  $\{K_{Ic}(\text{Indent, constant E})\}$ . Fracture toughness values in column 7 were calculated using the measured specimen elastic modulus [78], in equation 3-3  $\{K_{Ic}(\text{Indent})\}$ .

$P_p$ Volume fraction porosity	E [78] (GPa)	$H_v$ [78] (GPa)	$P/c^{3/2}$ [78] (MPa m <sup>1/2</sup> )	$K_{Ic}$ [78] (SENB) (MPa m <sup>1/2</sup> )	$K_{Ic}^*$ (Indent, constant E) (MPa m <sup>1/2</sup> )	$K_{Ic}^{**}$ (Indent) (MPa m <sup>1/2</sup> )
0.05	97.2	3.95	15.85	N/A	1.40	1.26
0.06	81.1	4.08	18.03	1.73	1.57	1.29
0.07	62.6	4.09	13.35	1.58	1.16	0.84
0.15	51.4	N/A	N/A	N/A	N/A	N/A
0.16	74.4	2.91	12.75	1.09	1.31	1.03
0.25	32	1.09	N/A	0.73	N/A	N/A
0.29	22	0.64	7.65	0.43	1.68	0.72
0.31	19	0.5	5.05	0.37	1.25	0.50
MSA Fit of the above properties						
$A_0$	120	7.08	20.5	2.54	1.34	1.35
b	5.57	7.98	3.89	5.84	-0.180	2.65
$r^2$	0.898	0.953	0.898	0.963	0.023	0.734

N/A- data not available from Tancret et al. [78]

\* Calculated with Equation 3-3 setting  $E = 120$  GPa,  $H_v$  from column 3 and  $P/c^{3/2}$  from column 4.

\*\*Calculated with equation 3-3 using E from column 2,  $H_v$  from column 3 and  $P/c^{3/2}$  from column 4.

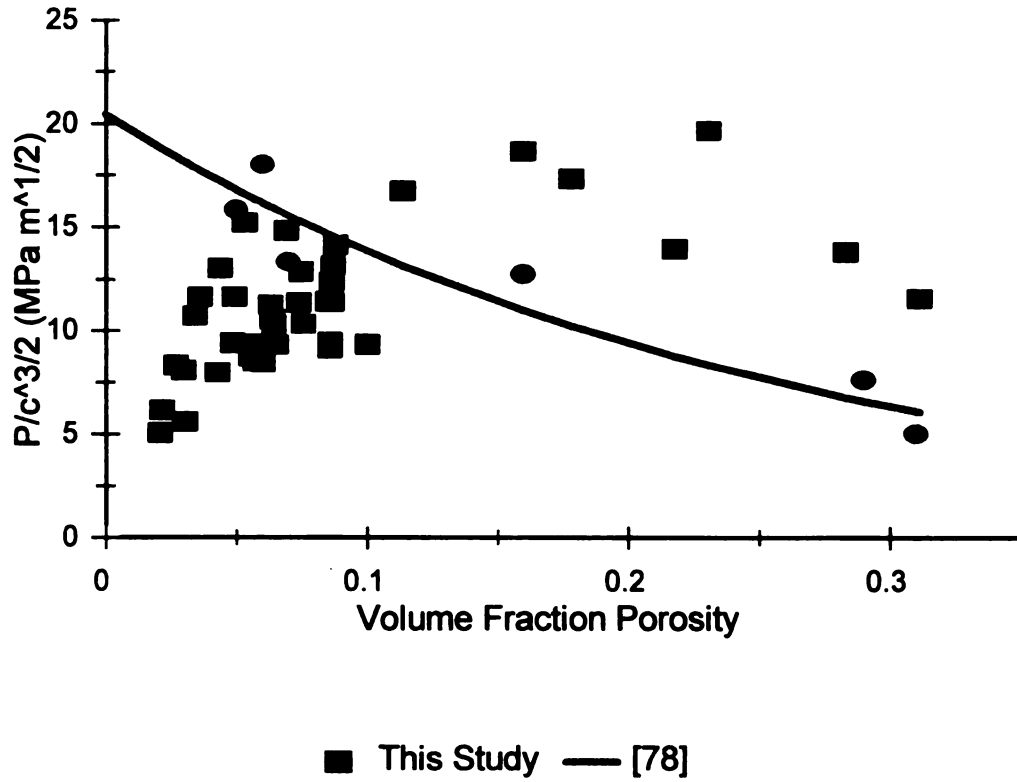


Figure 3-28 Crack parameter  $P/c^{3/2}$  as a function of the volume fraction porosity for hydroxyapatite from this study and for  $YBa_2Cu_3O_{7-x}$  from Tancret et al. [78]. The line through the  $YBa_2Cu_3O_{7-x}$  data is from the MSA fit ( $\ln P/c^{3/2} = \ln(P/c^{3/2}_0) - b_p P_p$ ) of the crack parameter  $P/c^{3/2}$  [78].

From Equation 3-3, the indentation fracture toughness was calculated using the elastic modulus, Vickers hardness, and  $P/c^{3/2}$  for each  $\text{YBa}_2\text{Cu}_3\text{O}_{7-x}$  specimen. The resulting indentation fracture toughness values fit to the MSA model exhibited significantly smaller material dependent constant ( $b_k = 2.65$ ) than the  $b_k$  value (5.84) determined from the MSA fit of the fracture toughness values determined by SENB [78] (Table 3-8, Figure 3-29). The fracture toughness values of the  $\text{YBa}_2\text{Cu}_3\text{O}_{7-x}$  specimens calculated by equation 3-3 with a constant elastic modulus ( $E_0 = 120$  GPa), along with each specimen's Vickers hardness and crack parameter ( $P/c^{3/2}$ ) are unvarying over the entire porosity range (Table 3-8, Figure 3-29).

$\text{YBa}_2\text{Cu}_3\text{O}_{7-x}$  high temperature superconducting ceramic has a orthorhombic crystal structure [79].  $\text{YBa}_2\text{Cu}_3\text{O}_{7-x}$  is similar in the mechanical properties of the elastic modulus and hardness as hydroxyapatite (Table 3-9).

### 3.5.1.3 Porosity dependence of the empirical constant $\zeta$

The difference between the fracture toughness of  $\text{YBa}_2\text{Cu}_3\text{O}_{7-x}$  determined by SENB and by the indentation method suggests the correction factor,  $\zeta$ , may be a function of the volume fraction porosity. The constant  $\zeta$  had been determined by comparing indentation crack patterns of a number of “well behaved” reference ceramics [40] to fracture toughness values determined by conventional fracture toughness techniques such as double torsion (DT) [39,40], and double cantilever beam (DCB) [40]. Using the MSA model for the SENB fracture toughness data to serve as the correct fracture toughness values, as a function of porosity, and the MSA model fit ( $\ln(K_{ic}) = \ln(K_{ic0}) - b_K P_P$ , Equation 1-8) for the indentation fracture toughness values, as a function of porosity, a

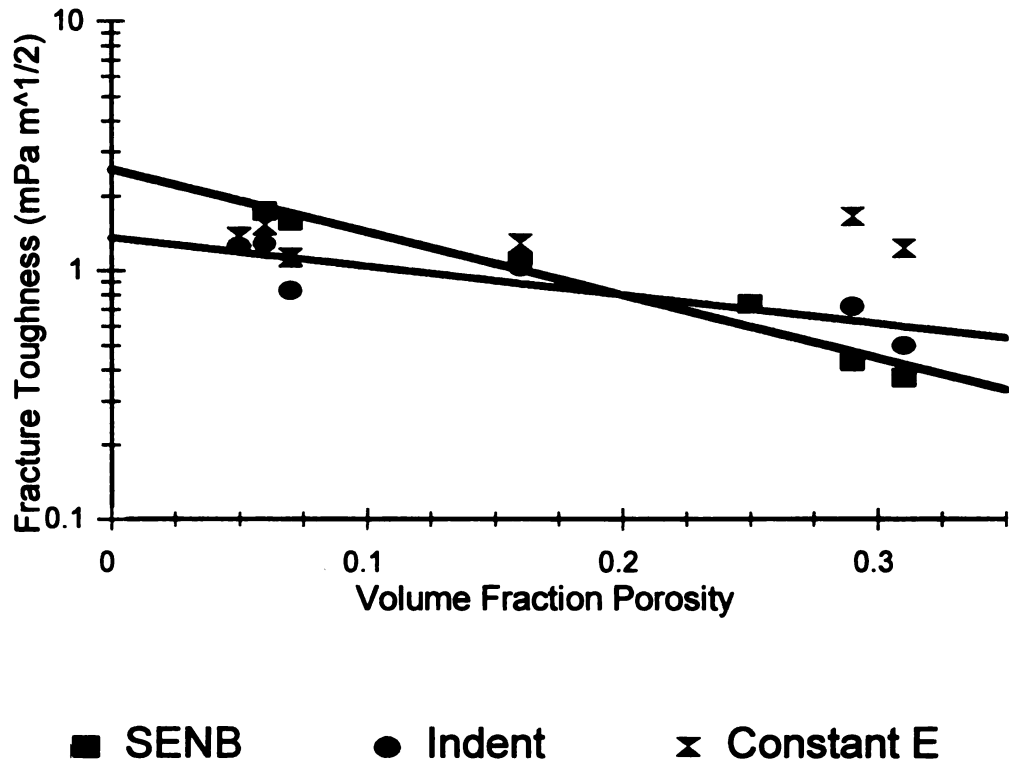


Figure 3-29 Fracture toughness  $\text{YBa}_2\text{Cu}_3\text{O}_{7-x}$  of as a function of the volume fraction porosity determined by SENB [78] (Table 3-7), Indentation method  $K_{Ic} = \zeta (E/H)^{1/2} P/c^{3/2}$  (Equation 3-3) with the data from Table 3-7, and the indentation method (Equation 3-3) with constant elastic modulus ( $E = 114$  GPa) from Tancret et al. [78].

Table 3-9 Comparison of the zero porosity mechanical properties of  $\text{YBa}_2\text{Cu}_3\text{O}_{7-x}$  and HAP ( $\text{Ca}_{10}(\text{PO}_4)_6(\text{OH})_2$ ).

Material	$E_0$	$H_{v0}$	$K_{ic0}$
$\text{YBa}_2\text{Cu}_3\text{O}_{7-x}$ *	114 GPa [78]	5.0 GPa [78]	2.4 MPa $\text{m}^{1/2}$ [78]
MSA Fit**	120 GPa [78]	7.1 GPa [78]	2.5 MPa $\text{m}^{1/2}$ [78]
$\text{Ca}_{10}(\text{PO}_4)_6(\text{OH})_2$	115 GPa [54] 117 GPa [80]	6.0 GPa [This study] 6.4 GPa [22]	1.1 MPa $\text{m}^{1/2}$ [54] 1.2 MPa $\text{m}^{1/2}$ [76]

\*  $\text{YBa}_2\text{Cu}_3\text{O}_{7-x}$  data fit by Tancret et al. [78] using power law functions:  $E = E_0(1-P_p)^m$ ;  $H_{v0} = H_{v0}(1-P_p)^m$  and  $K_{ic} = K_{ic0}(1-P_p)^m$  where  $P_p$  is the porosity, and  $m$  is a microstructure dependent exponent.

\*\*  $\text{YBa}_2\text{Cu}_3\text{O}_{7-x}$  data [78] fit to the MSA model ( $\ln(A) = \ln(A_0) - b_A P_p$ ), for this study (from Table 3-8)

correction factor as a function of the volume fraction porosity  $\zeta(P_p)$  can be calculated for porous  $\text{YBa}_2\text{Cu}_3\text{O}_{7-x}$  [78], (Equation 3-7).

$$\zeta(P_p) = \frac{K_{Ic0}(SENB)e^{-b_K P_p}}{K_{Ic0}(Indent)e^{-b_K P_p}} = e^{\Delta b_K P_p} \frac{K_{Ic0}(SENB)}{K_{Ic0}(Indent)} \quad (3-7)$$

where the difference between the material dependent parameters  $b_K$  (Indent) and  $b_K$  (SENB) are from the MSA model fit ( $\ln(K_{Ic}) = \ln(K_{Ic0}) - b_K P_p$ , Equation 1-8) of the  $\text{YBa}_2\text{Cu}_3\text{O}_{7-x}$  data,  $\Delta b_K = b_K$  (Indent) -  $b_K$  (SENB),  $K_{Ic0}$ (SENB) is the zero porosity fracture toughness determined from the SENB data fit to the MSA model,  $K_{Ic0}$ (Indent) is the zero porosity fracture toughness determined from the indentation fracture toughness data fit to the MSA model. For the data from Tancret et al. [78] (Table 3-8) the correction equation  $\zeta(P_p) = 1.88 e^{-3.19P_p}$ . Adding  $\zeta(P_p)$  to the indentation fracture toughness equation (Equation 3-3) relates the calculated fracture toughness from the indentation method to the fracture toughness determined by SENB and results in (Equation 3-8).

$$K_{Ic} = \zeta(P_p) \left( \frac{E}{H_V} \right)^{1/2} \frac{P}{c^{3/2}} \quad (3-8)$$

Application of  $\zeta(P_p)$  to the indentation fracture toughness of sintered hydroxyapatite ( $K_{Ic}\{E(P_p)\}$ ) (Equation 3-6) can be used as a first approximation to correct the indentation fracture toughness method to porous ceramics (Equation 3-9).

$$K_{Ic} \{ \zeta(P_p), E(P_p) \} = \zeta(P_p) E_0 e^{-\frac{1}{2} b_E} \left( \frac{1}{H_V} \right)^{1/2} \frac{P}{c^{3/2}} \quad (3-9)$$

The fracture toughness correction ( $K_{Ic} \{ \zeta(P_p), E(P_p) \}$ ) of the sintered hydroxyapatite specimens in this study further lessens the porosity dependence of the fracture toughness (Figure 3-30), as compared to the fracture toughness calculated by equation 3-6 ( $K_{Ic} \{ E(P_p) \}$ ) (Figure 3-27).

### 3.5.2 Examples of deviations from the MSA model for fracture toughness

From the 21 examples found in the literature in which the fracture toughness of porous ceramics were measured only 4 show the fracture toughness increasing slightly or remaining unchanged as the porosity increases (Table 3-10). The normalized fracture toughness parameter data from Ricote et al. [48] and Case et al. [81] (Figure 3-31) depends less on the specimen porosity than the sintered hydroxyapatite specimens in this study (Figure 3-32). The critical volume fraction porosity ( $P_c$ ) for which physical properties drop precipitously is seen for  $Gd_2O_3$  at  $P_c \sim 0.30$  [81]. At  $P \sim 0.25$  the fracture toughness parameter of the sintered hydroxyapatite specimens drops off precipitously and appears to indicate the critical volume fraction for sintered hydroxyapatite.

### 3.5.3 Possible toughening mechanisms in sintered hydroxyapatite

Fracture toughness is a measure of the energy needed to extend a crack [82]. Crack deflection by pores may increase the fracture toughness as the porosity increases



Table 3-10 Fracture toughness/porosity trends fit to the MSA model ( $\ln(K_{i0}) = \ln(K_{i0}) - b_k P_p$ ) from the literature data for a variety of porous ceramics. The processing method (prc) and fracture toughness test method (meth.) are included.

Ceramic (prc*)	Porosity range %	$b_k$ (meth.**)	Reference
Al <sub>2</sub> O <sub>3</sub> (HP)	2-40	2.2 (DCB)	Wu and Rice from [53,58]
Al <sub>2</sub> O <sub>3</sub> (PC)	4-42	3.4 (NB)	Lam et al. from [53]
Al <sub>2</sub> O <sub>3</sub> (HP)	0-9	2 (WOF)	Cappola and Bradt from [53]
Al <sub>2</sub> O <sub>3</sub> (S)	0-44	3.4 (NB)	Pabst from [53]
Al <sub>2</sub> O <sub>3</sub> (HP/S)	2-46	4.2 (NB)	Claussen et al. from [53]
Al <sub>2</sub> O <sub>3</sub> (S)	5-50	2.5 (N/A)	Evans and Tappin from [53]
Al <sub>2</sub> O <sub>3</sub> (HP)	2-14	no fit (DCB)	[53]
MgO (HP)	5-25	no fit (DCB)	[53]
Gd <sub>2</sub> O <sub>3</sub> (CIP/S)	3-47	no fit (NB)	[81]
HAP (CIP/S)	3-27	2.79 (TPB)	[54] fit in this study
HAP (HP,S)	1-29	2.81 (Ind)	[56] fit in this study
HAP (CIP,S)	2-31	no fit (Ind)	[this study]
PZT (S)	2-15	2.4 (DT)	Biswas and Fulrath from [53]
PCT (N/A)	4-28	no fit (Ind)	[48]
YBa <sub>2</sub> Cu <sub>3</sub> O <sub>7-x</sub>	5-31	5.8 (SENB)	[78] fit in this study
YBa <sub>2</sub> Cu <sub>3</sub> O <sub>7-x</sub>	5-31	2.7 (Ind)	[78] fit in this study
SiC (S)	1-7	1.8 (N/A)	Seshardi et al. from [58]
B <sub>4</sub> C (HP)	0-15	2.3 (DCB)	Wu and Rice from [58]
B <sub>4</sub> C (HP)	0-15	3.4 (DT)	Hollenberg & Walther from [53]
Si <sub>3</sub> N <sub>4</sub> (HP/S)	0-10	5.2 (Ind)	Mukhoyadhyay et al. from [53]
Si <sub>3</sub> N <sub>4</sub> (HP/S)	0-50	2.4 (N/A)	Rice et al. from [53]

\*HP-hot pressed, PC-pressure cast, S-sintered, /S-and sintered, CIP-cold isostatic pressing, HP,S-hot pressed specimens plus sintered specimens, N/A-data not available.

\*\*DCB-double cantilever beam, NB-notch beam, WOF-work of fracture, TPB-three point bend, Ind-indentation crack measurement, DT-double torsion, SENB-single edge notched beam, N/A-data not available.

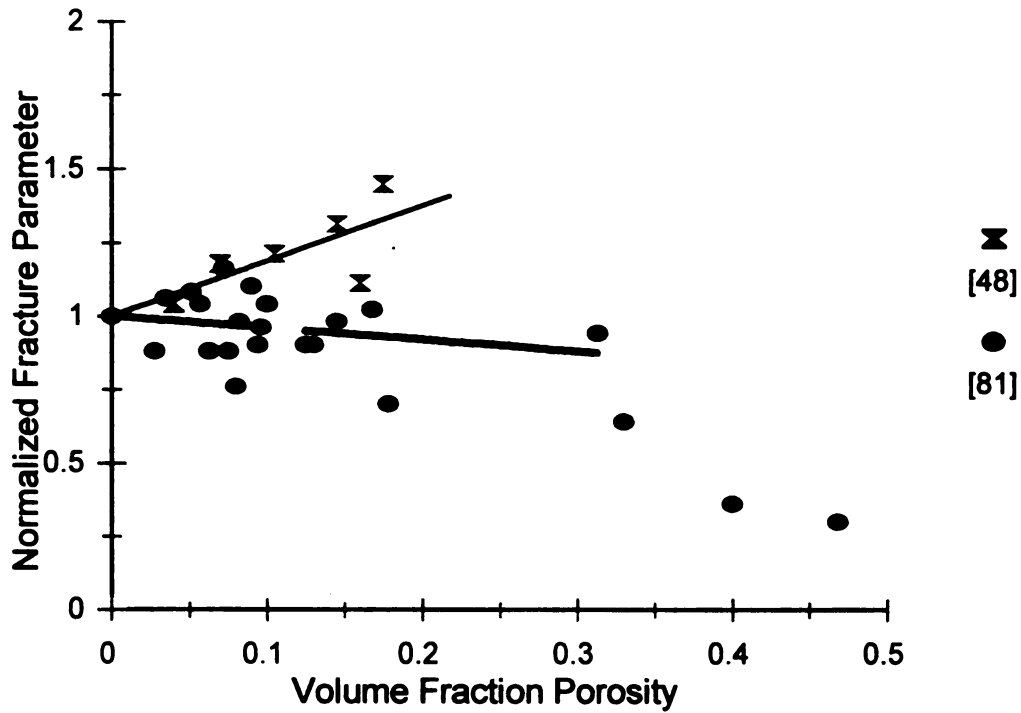


Figure 3-31 Normalized fracture toughness parameters (fracture toughness for Ricote [48], and fracture energy for Case et al. [81]) studies in which the fracture toughness parameters increased or decreased slightly, over a significant volume fraction porosity range. Normalization is done by dividing the fracture toughness by the zero porosity fracture toughness as determined by the intercept of the linear fit. The linear fit (included in plot) calculated for the entire range of Ricote et al's data [48]. The linear fit calculated for the Case et al. [81] data was done for specimens with < 0.30 volume fraction porosity. The ceramics in question are calcium modified lead titanate for Ricote [48] and gadolinia for Case et al. [81].

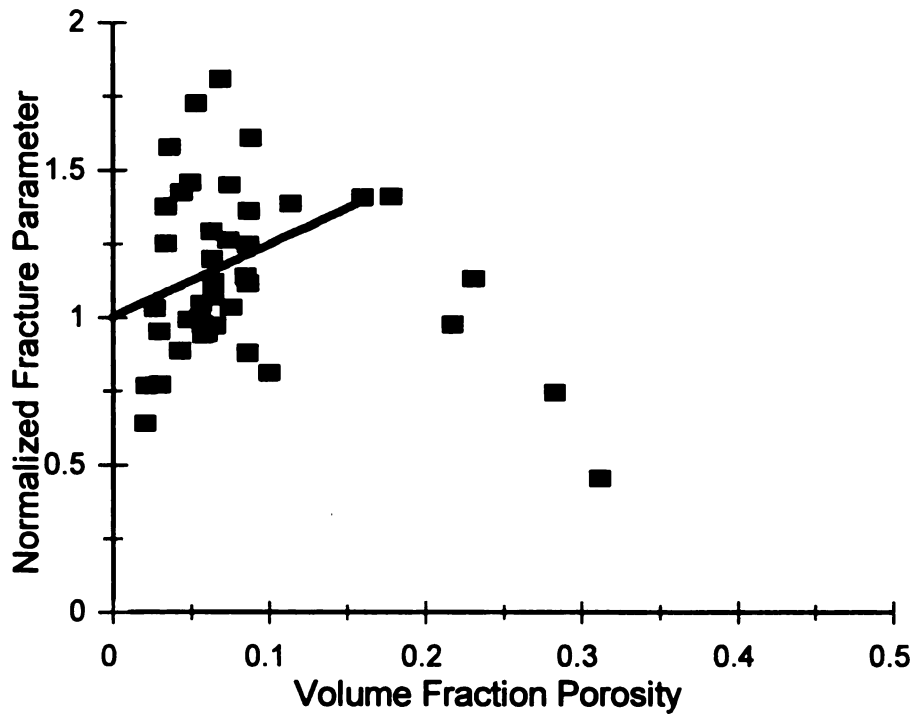


Figure 3-32 Normalized fracture toughness for sintered hydroxyapatite specimens in this study. Normalization is done by dividing the fracture toughness by the zero porosity fracture toughness as determined by the intercept of the linear fit. The linear fit (included in plot) was calculated for hydroxyapatite specimens < 0.20 volume fraction porosity.

[83,84]. For a specific crack-pore geometry the fracture toughness may increase if the pores cause the direction of crack propagation to deviate from the direction normal to the applied stress [82]. In general, however, the fracture toughness decreases as porosity increases due to the local applied stress acting over decreasing cross sectional area [85,82]. Fracture toughness decreases with increasing porosity (Section 3.4) for both sintered hydroxyapatite [54,56], and  $\text{YBa}_2\text{Cu}_3\text{O}_{7-x}$  [78].

Microcracks induced by thermal expansion anisotropy or thermal expansion mismatch can decrease the fracture toughness for many non-cubic ceramics [53]. For example microcracking due to thermal expansion anisotropy was deemed responsible for a 15% decrease in the fracture toughness of  $\beta$ -silicon nitride as the average grain size increased [51].

Chou et al. [77] compared the elastic modulus and fracture toughness of SiC platelet reinforced alumina for two different SiC platelet sizes.  $E$  and  $K_{Ic}$  for SiC platelet (24 $\mu\text{m}$  average diameter) reinforced alumina decreased 40% and 50% respectively as the volume fraction of SiC platelets increased from 0.0 to 0.4 [77]. Alumina reinforced by SiC platelets of 12  $\mu\text{m}$  average diameter exhibited a 65% increase in  $K_{Ic}$  for 0.4 volume fraction SiC addition [77]. Thermal expansion mismatch resulted in microcracking between the large SiC platelets and the alumina matrix [77].

Microcracking due to thermal expansion mismatch and phase transformation resulted in toughening by crack shielding and a locally reduced elastic modulus for  $\text{MoSi}_2/\text{unstabilized ZrO}_2$  composite [86].  $K_{Ic}$  values for 20 volume percent  $\text{ZrO}_2/\text{MoSi}_2$  were over twice that of  $\text{MoSi}_2$  [86].

The absence of apparent grain size-property trends in the data from the sintered

hydroxyapatite specimens in this study implies that either 1) No microcracks exist or 2) Microcrack damage has saturated for the grain size range included in this study [36].

### 3.6 Thermal Expansion

Thermal expansion data for a high purity alumina reference specimen collected by identical methods as the sintered hydroxyapatite specimens prepared for this study, was compared to the American Institute of Physics Handbook [87] data for alumina (Table 3-11). The average thermal expansion coefficients from 3 different runs with the alumina reference specimen were plotted against the handbook data (Figure 3-33). There was reasonable agreement up to  $\sim 400^{\circ}\text{C}$ , for thermal expansion coefficient ( $\alpha$ ) taken on heating and cooling, with significant divergence between the heating and cooling curves above  $600^{\circ}\text{C}$  (Figure 3-33).

Table 3-11 Thermal expansion data for Alumina, from *American Institute of Physics Handbook 2<sup>nd</sup> Edition* [87].

Temperature ( $^{\circ}\text{C}$ )	Parallel c-axis ( $\times 10^{-6} / ^{\circ}\text{C}$ )	Perpendicular c-axis ( $\times 10^{-6} / ^{\circ}\text{C}$ )	Polycrystalline ( $\times 10^{-6} / ^{\circ}\text{C}$ )*
0	5.5	4.6	4.9
200	7.8	7.1	7.33
400	8.9	8.1	8.37
600	9.4	8.5	8.8
800	9.7	8.8	9.1

\* calculated from lattice expansion data and equation 1-3.

Thermal expansion coefficient data for sintered hydroxyapatite specimens numbers

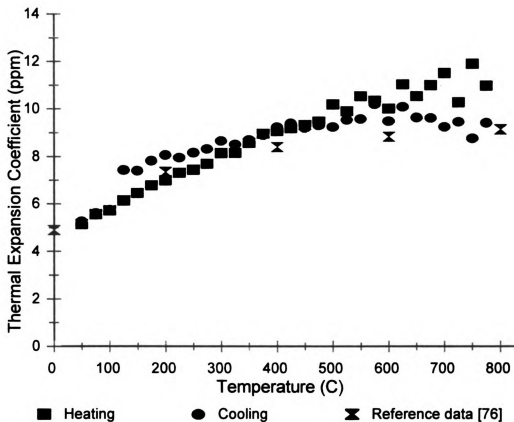


Figure 3-33 Thermal expansion coefficient for high purity alumina determined by dilatometry, as a function of temperature and compared with the American Institute of Physics Handbook Value [76] (Table 3-6). Dilatometry data taken from Appendix A.

4-10 and numbers 11-12 on heating showed much more variability at temperatures greater than 600° C (Figure 3-34). The thermal expansion coefficients collected during cooling, for the same experimental runs, exhibit significant scatter at all temperatures and had a different shape than the heating data (Figure 3-35). The average thermal expansion coefficient, measured during heating, for all the hydroxyapatite specimens increases from 12.9 ppm at 100° C to 19.1 ppm at 600° C and the average thermal expansion coefficient measured during cooling increases very little being 19.1 ppm at 100° C and 20.8 ppm at 600° C (Table 3-12). No correlation between the grain size, and the thermal expansion coefficients, measured at 400° C, are seen (Figure 3-36).

The difference, Delta ( $\Delta$ ), in the thermal expansion coefficient data, for the hydroxyapatite specimens, between the heating and cooling curves, for all the runs, is positive below 500° C and goes negative at temperatures greater than 500° C (Figure 3-37).

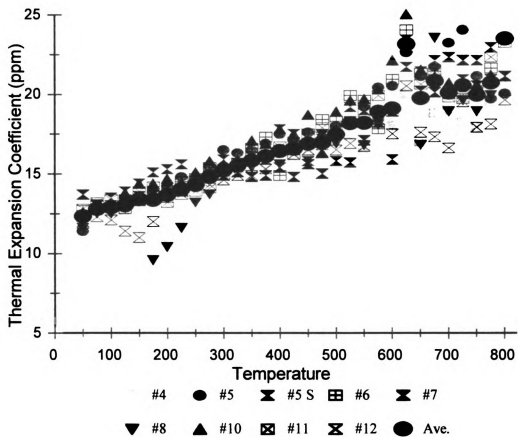


Figure 3-34 Thermal expansion coefficients, measured by dilatometry on heating, for sintered hydroxyapatite specimens numbers 4-8 and numbers 10-12. Data taken from Appendix A.

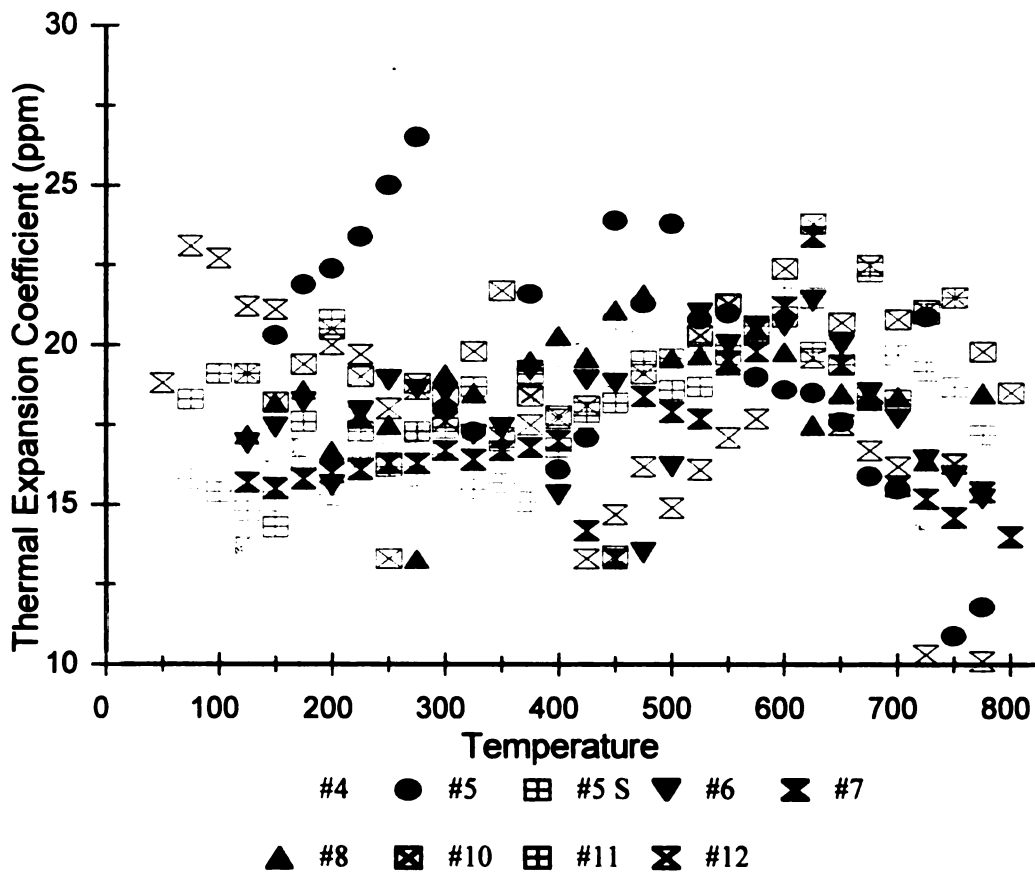


Figure 3-35 Thermal expansion coefficient data for sintered hydroxyapatite, from cooling dilatometry. The data taken from Appendix A.

Table 3-12 The averaged thermal expansion coefficients for sintered hydroxyapatite specimen numbers 4-8, and 10-12 by dilatometry. The delta is the difference between the cooling data and the heating data:  $\Delta = \alpha_{cool} - \alpha_{heat}$ .

Temperature (°C)	Heating data (ppm)	Cooling data (ppm)	Delta (ppm)
100	12.89	19.07	6.18
200	13.75	18.41	4.66
300	15.12	17.78	2.66
400	16.34	17.42	1.08
500	17.52	18.78	1.26
600	19.79	20.77	0.98
700	20.20	17.52	-2.68
750	20.92	16.96	-3.96

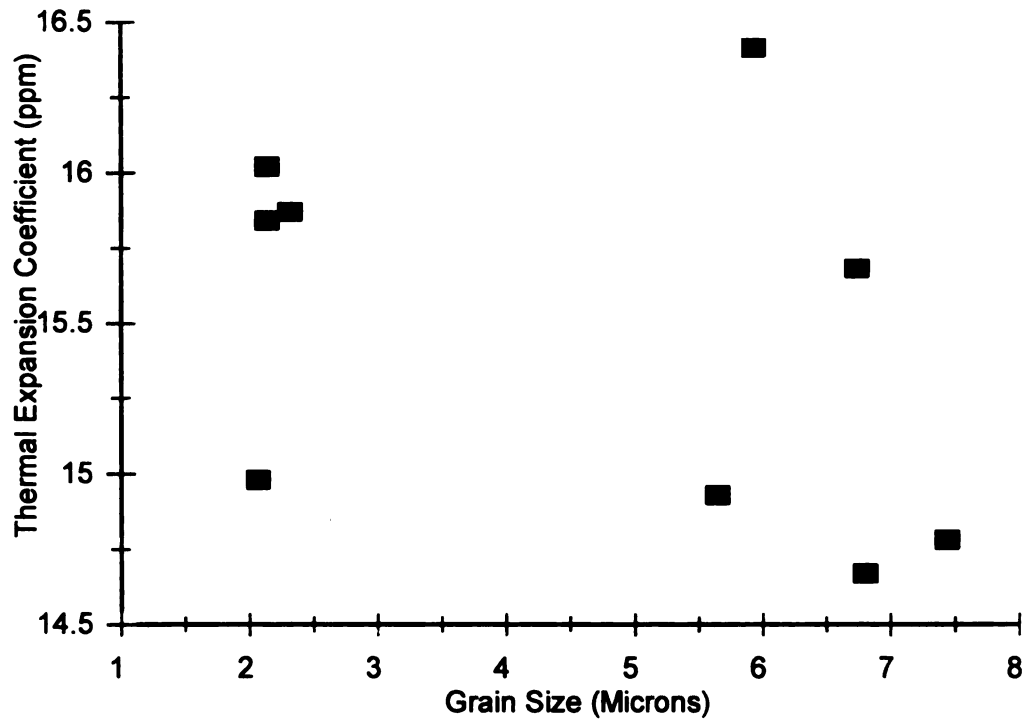


Figure 3-36 Average thermal expansion coefficient for sintered hydroxyapatite specimens #4-8 and #10-12 (heating to 600° C) as a function of the average grain size. The data was taken from Appendix A.

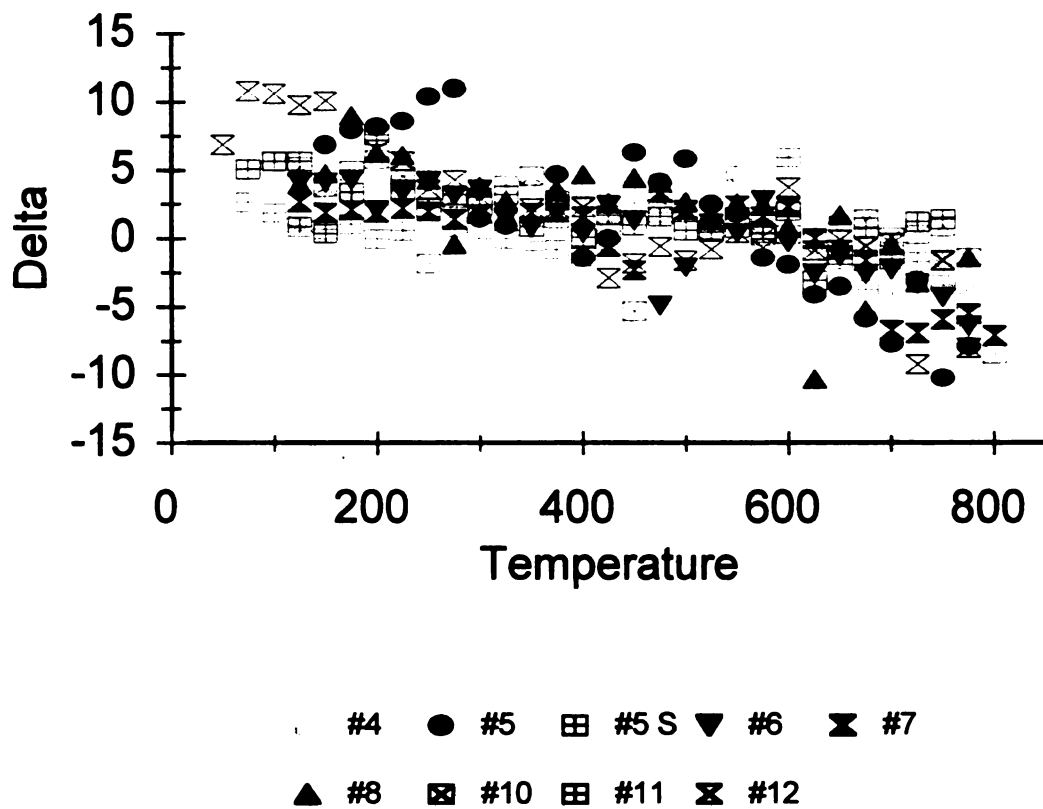


Figure 3-37 Difference in the thermal expansion coefficient for sintered hydroxyapatite,  $\Delta = \alpha_{\text{cooling}} - \alpha_{\text{heating}}$ , as a function of temperature. Dilatometry data taken from Appendix A.

### 3.7 Dielectric measurements

#### 3.7.1 Circuit capacitance measurement and correction

The circuit used to measure the relative permittivity was calibrated using the alumina reference specimen (ADS995, Coors) of known dielectric properties [72] (Table 3-13). The average measured capacitance (from three measurements at 45 kHz) of the circuit (Figure 2-7) with the alumina reference specimen inserted in the electrodes was 46.23 pF at 45 kHz. The capacitance of the alumina reference specimen in the electrodes ( $C_{ADS}$ ) was calculated from the known relative permittivity at 45 kHz and the geometry of the electrodes  $C_{ADS} = 28.89$  pF (Equation 3-10) [88].

$$C_{ADS} = (\epsilon_0 k_d A) / d \quad (3-10)$$

Where  $\epsilon_0$  is the permittivity of free space,  $k_d$  is the relative permittivity,  $A$  is the area of the electrodes (corrected to add the width of the guard gap per ASTM D 150-95 [73]), and  $d$  is the specimen thickness. The circuit capacitance  $C_c$  was then established to be the difference in the measured capacitance  $C_m$  and the capacitance calculated for the reference specimen  $C_{ADS}$ . The circuit capacitance was determined to be  $C_c = C_m - C_{ADS} = 17.34$  pF. The capacitance for the sintered hydroxyapatite specimens was determined by subtracting the circuit capacitance (17.34 pF) from the measured circuit capacitance. The circuit capacitance determined at 45 kHz was used at all frequencies.

Table 3-13 Dielectric characteristics for Coors ADS 995 alumina substrate. Data from Tech Specs, Thin Film Substrates Technical Specifications 10-3-0897 from Coors Ceramics, Golden, CO [72].

Frequency	Dielectric constant	Loss Factor	$Q = 1/(\text{Loss factor})$
1 kHz	$9.9 \pm 1$	0.003	333
1 MHz	$9.9 \pm 1$	0.001	1000

### 3.7.2 Relative permittivity of hydroxyapatite

The relative permittivity of the hydroxyapatite specimens was calculated from corrected capacitance measurements. The geometry of the electrodes and specimen thickness were used to calculate the relative permittivity of sintered hydroxyapatite by rearranging equation 3-3 [88] (Equation 3-11).

$$k_d = C d / \epsilon_o A \quad (3-11)$$

where the variables are as defined for equation 3-10.

The fully dense hydroxyapatite relative permittivity ( $k_{cer}$ ), was calculated for MGT1 (Table 3-14) by a simple fit of the data to equation 1-9. For each specimen the difference of the measured relative permittivity  $k_d$  and the calculated  $k_m$ , from equation 1-9 was calculated with the specimen's relative density and the variable  $k_{cer}$ . The differences were then summed. The fully dense hydroxyapatite relative permittivity ( $k_{cer}$ ) was incremented in equation 1-9 until the sum of the differences was at a minimum. The fully dense hydroxyapatite relative permittivity ( $k_{cer}$ ) was also calculated for MGT2 and equation 1-10 (Table 3-14).

The relative permittivity of sintered hydroxyapatite at 45 kHz decreased as the relative density decreased (Figure 3-38). As a function of the relative density the data for the hydroxyapatite specimens more closely matched MGT2 than MGT1 (Figure 3-38). The relative permittivity of the sintered hydroxyapatite is stable over the measured frequency range (45 kHz - 7.3 MHz) (Figure 3-39, Figure 3-40).

The relative permittivity of hydroxyapatite sintered with  $Mg^{2+}$  additives and partially decomposed, as determined by x-ray diffraction was measured by Fanovich et al. [89]. The relative permittivity of the sintered hydroxyapatite specimens measured by

**Table 3-14** Relative permittivity for sintered hydroxyapatite from this study and Fanovich et al. [89] and the fit parameters for the Maxwell-Garnet equations.

	This study		Fanovich et al. [89]		
	Fit parameters		Fit parameters		
	MGT1	MGT2	MGT1	MGT2	
$k_{cer}$	13.01	17.63	15.4	28.3	
Difference per data point*	0.831	0.698	1.39	0.696	
Specimen Label	Relative Density	$k_m$	Mg <sup>2+</sup> weight %	Relative Density	$k_m$
44	0.952	11.63	1	0.897	13.62
14	0.951	13.55	0	0.856	12.61
43	0.947	11.62	3	0.846	9.81
45	0.937	12.05	5	0.830	9.45
16	0.936	12.64			
42	0.936	12.47			
50	0.931	11.53			
49	0.924	12.02			
46	0.918	11.63			
41	0.769	7.94			
36	0.658	5.62			
33	0.579	4.93			

- \* The sum of the differences between the measured data and the fit equation divided by the number of total data points.

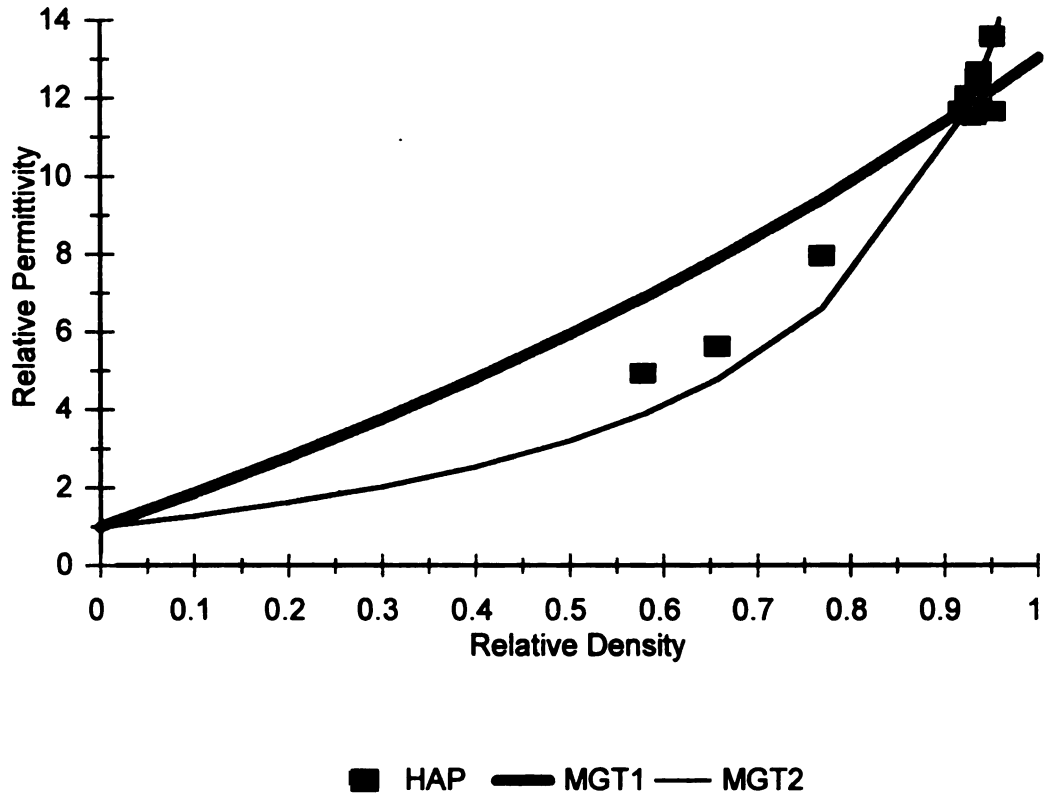


Figure 3-38 Relative permittivity data from sintered hydroxyapatite and the fitted Maxwell-Garnet equations MGT1 (Equation 1-9) and MGT2 Equation (1-10). The data was taken from Table 3-9.

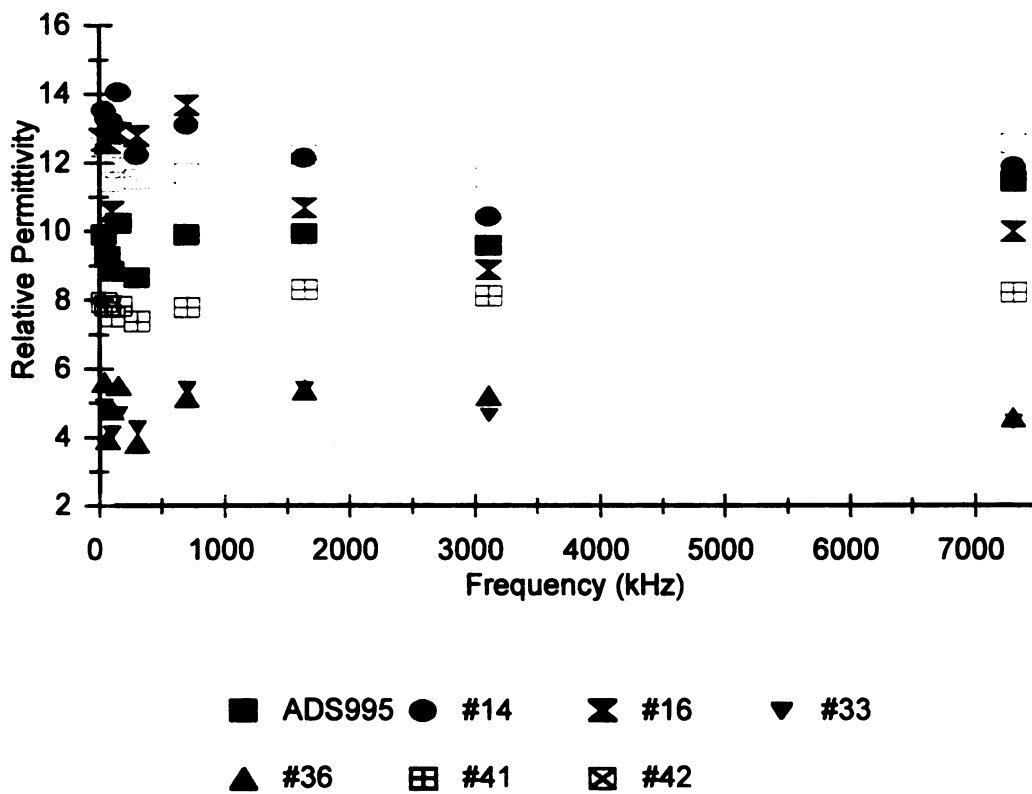


Figure 3-39 Relative permittivity for the sintered hydroxyapatite specimen numbers 14, 16, 33, 41, 42 and the alumina reference material ADS995 as a function of frequency. The data was taken from Appendix B.

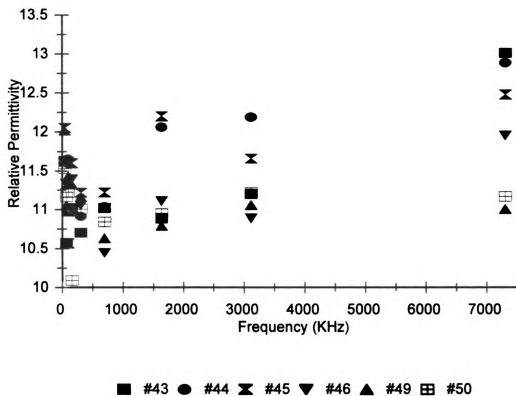


Figure 3-40 Relative permittivity for sintered hydroxyapatite specimen numbers 43-46, 49 and 50 as a function of frequency. The data was taken from Appendix B.

Fanovich et al. [89] were greater than the sintered hydroxyapatite specimens in this study as a function of relative density. Fitting the data from Fanovich et al. [89] to MGT1 and MGT2 produced a closer match to MGT2 (Table 3-14). Sintered monoclinic hydroxyapatite of 97.6% relative density was determined to have a relative permittivity of 15.4 at 100 kHz by Ikoma et al. [26].

#### 4.0 Summary and Conclusions

Commercially available hydroxyapatite powder can be sintered to 96% relative densities by simple uniaxial die pressing and pressure-less sintering at 1300<sup>o</sup> C. Final sintered density is a strong function of the pre-sintering densification. A linear relationship between final sintering density and uniaxial die pressure was determined. The final sintered density of hydroxyapatite specimens sintered at 1300<sup>o</sup> C for less than 120 minutes increased 0.27% in relative density for each additional MPa of pressure applied. An increase in the relative density of sintered hydroxyapatite to 98% required cold isostatic pressing before sintering at 1300<sup>o</sup> C. Average grain sizes for the hydroxyapatite specimens fell between 1.5 μm and 7.5 μm and are a function of sintering time and temperature.

There were no decomposition phases of hydroxyapatite detected by x-ray diffraction for hydroxyapatite specimens sintered at 1300<sup>o</sup> C with sintering times up to 11 hours and at 1400<sup>o</sup> C for as long as 4 hours. The phase stability of the hydroxyapatite is attributed to the slightly rich calcium content (36-37% by specific analysis) of the commercial hydroxyapatite powder and from the moisture present in the ambient atmosphere of the furnaces used.

The Vickers hardness values measured for the sintered hydroxyapatite specimens in this study were successfully fit, as a function of the volume fraction porosity (P), to the exponential decay equation ( $H_v = H_0 e^{-bP}$ ) with the zero porosity hardness value  $H_0 = 6.00 \pm 0.7$  GPa and decay constant  $b = 6.03$ .

Fracture toughness of the sintered hydroxyapatite specimens in this study diverged from the expected exponential decay function as the porosity increased. The measured

fracture toughness is 0.4-0.6 MPa m<sup>1/2</sup> for sintered hydroxyapatite specimens of 97% relative density. The fracture toughness of sintered hydroxyapatite increased to 2.5-2.7 MPa m<sup>1/2</sup> at 72-75% relative density. Published data from other researchers on the fracture toughness of sintered hydroxyapatite was successfully fit, in this study, to the exponential decay equation with nearly identical b values of 2.786 [54] and 2.812 [56]. Fracture toughness of specimens at 97% relative density were 1.34-1.5 MPa m<sup>1/2</sup> for hydroxyapatite whisker reinforced hydroxyapatite[56] and 1.01-1.2 MPa m<sup>1/2</sup> for dense unreinforced sintered hydroxyapatite [54,56,76].

Corrections to the indentation fracture toughness equation (Equation 2-6, Equation 3-3) for the decrease in the elastic modulus as the porosity increased decreased the calculated fracture toughness over the entire porosity range (  $K_{Ic}(E(P_p))$ , Equation 3-6). The exponential in equation 3-6 decreased  $K_{Ic}$  to a greater degree as the porosity increased.  $K_{Ic}$  increased as the porosity increased up to  $\approx 0.2$  volume fraction then decreased.  $K_{Ic}$  peaked at  $\approx 1.6$  MPa m<sup>1/2</sup> for specimens of 0.225 volume fraction porosity.

Comparing the fracture toughness measured by SENB to that measured by the indentation method for YBa<sub>2</sub>Cu<sub>3</sub>O<sub>7-x</sub> [78] suggested a further correction to the indentation fracture toughness equation  $K_{Ic}(E(P_p))$ . Assuming the empirical constant is a function of porosity  $\zeta(P_p)$ ,  $K_{Ic}$  measured by the indentation method can be equated to  $K_{Ic}$  measured by SENB for the YBa<sub>2</sub>Cu<sub>3</sub>O<sub>7-x</sub> specimens.  $\zeta(P_p)$  added to  $K_{Ic}(E(P_p))$  produced  $K_{Ic}(\zeta(P_p),E(P_p))$  (Equation 3-9). Applying  $K_{Ic}(\zeta(P_p),E(P_p))$  to the indentation of the sintered hydroxyapatite specimens prepared for this study increased  $K_{Ic}$  to 0.6-1.0 MPa m<sup>1/2</sup> at low porosity ( $\sim 0.03$  volume fraction porosity).  $K_{Ic}$  peaked at 1.8-2.0 MPa m<sup>1/2</sup> for volume fraction porosities 0.06 to 0.17 before decreasing.

Both corrections to the indentation fracture toughness equation (Equation 3-6, and 3-9) when applied to the sintered hydroxyapatite indentation data produced increasing  $K_{Ic}$  at low and moderate porosities (0.02-0.15) before falling off. A small percentage (5 out of 21) of the  $K_{Ic}$ /Porosity studies found in the literature report other than decreasing  $K_{Ic}$  as porosity increases.

The hysteresis seen in the heating and cooling curves of sintered hydroxyapatite from the dilatometer was determined to be an artifact of the apparatus and not due to microcracking. The same hysteresis was seen for dilatometry data for the non-microcracked alumina specimen. The thermal expansion coefficients for sintered hydroxyapatite, averaged for the heating data for all the hydroxyapatite specimens tested, equals  $12.89 \times 10^{-6} / ^\circ\text{C}$  at  $100^\circ\text{C}$ ,  $13.75 \times 10^{-6} / ^\circ\text{C}$  at  $200^\circ\text{C}$ ,  $16.34$  at  $400^\circ\text{C}$  and  $19.79 \times 10^{-6} / ^\circ\text{C}$  at  $600^\circ\text{C}$ . The dilatometer was not accurate above  $600^\circ\text{C}$  based on the comparison between the handbook data [71] and the dilatometer values for the high purity alumina specimen above  $600^\circ\text{C}$ .

The maximum relative dielectric permittivity of sintered hydroxyapatite in this study was  $k = 13.55$  for a specimen of 95.1% relative density. The minimum relative dielectric permittivity  $k = 4.93$  for a specimen at 58.0% relative density. Maxwell-Garnet mixing laws were used to determine the zero porosity relative permittivity and the functional relationship between the relative permittivity and porosity of sintered hydroxyapatite specimens. The first mixing law (MGT1) assumes spherical pores in a ceramic matrix and was the least successful in fitting the data from this study. MGT2 in which spherical ceramic particles are in a matrix of air fit the data more successfully. MGT1 predicted a zero porosity relative permittivity of 13.01. MGT2 predicted  $k_0 =$

17.63 from the data in this study.

#### **4.1 Further Research**

The indentation technique for fracture toughness measurements used in this study, though used successfully for sintered hydroxyapatite by Suchanek et al. [56] needs further scrutiny. The size of the indentations grew as the sintered hydroxyapatite specimens became more porous, as expected. The larger indents, however, failed to produce the increased extent of the half-penny cracks. Possible mechanisms that would limit the indentation cracks in porous hydroxyapatite are densification below the indent and crack bridging between pores. Densification below the indent tip under load would absorb energy and disrupt the plastic/elastic interface responsible for indentation crack growth [90]. Crack bridging results in greater surface areas formed from half penny cracks of seemingly the same length.

## APPENDIX A

### Appendix A Thermal expansion data.

The thermal expansion data collected at 25 °C intervals from 50 °C to 800 °C for both the heating and cooling curves. The data was taken for sintered hydroxyapatite samples numbers (4-8, 10 and 11) along with two sintered alumina specimens.

**Table A1** Thermal expansion data for Hydroxyapatite samples number 4, 5 with no dwell at 800 °C, and 5 with a pause at 800 °C. The data is used in Figures 3-26 to 3-27.

Temperature (°C)	4 (µm/m °C)		5 (µm/m °C)		5 soak (µm/m °C)	
	Heat	Cool	Heat	Cool	Heat	Cool
50	12.2	0	11.4	N/A	12.0	N/A
75	12.7	3	12.7	N/A	13.1	15.8
100	12.6	0	13.0	N/A	13.5	15.4
125	12.6	13.7	13.0	N/A	13.9	14.8
150	13.1	16.1	13.4	20.3	14.4	15.1
175	13.4	16.8	13.9	21.9	15.1	16.2
200	14	N/A	14.2	22.4	15.3	15.3
225	13.8	17.8	14.8	23.4	15.6	16.2
250	14.1	18.8	14.6	25.0	14.4	16.6
275	14.5	17.2	15.5	26.5	15.0	15.9
300	14.2	17.7	16.5	18.0	15.9	16.6
325	14.9	17.0	16.3	17.3	15.5	15.5
350	15.0	18.6	16.5	N/A	15.9	15.7
375	15.4	18.5	16.9	21.6	15.9	15.1
400	16.6	19.3	17.5	16.1	17.8	16.5
425	16.1	19.8	17.1	17.1	17.5	17.4
450	16.2	20.7	17.6	23.9	15.8	18.4
475	16.1	20.2	17.2	21.3	17.2	19.1

APPENDIX A

Table A1 (cont'd)

Temperature (°C)	4 ( $\mu\text{m}/\text{m } ^\circ\text{C}$ )		5 ( $\mu\text{m}/\text{m } ^\circ\text{C}$ )		5 soak ( $\mu\text{m}/\text{m } ^\circ\text{C}$ )	
	Heat	Cool	Heat	Cool	Heat	Cool
500	17.0	19.6	18.0	23.8	17.7	19.6
525	17.4	20.2	18.3	20.8	19.2	19.8
550	16.6	21.3	19.2	21.0	19.0	19.8
575	18.1	18.9	20.4	19.0	18.8	20.7
600	18.0	20.4	20.5	18.6	15.9	21.8
625	20.0	20.9	22.6	18.5	21.7	21.5
650	17.0	18.1	21.1	17.6	21.4	19.9
675	18.8	18.2	21.7	15.9	22.1	18.4
700	19.0	15.5	23.2	15.5	20.0	19.7
725	18.2	14.5	24.0	20.9	20.9	19.2
750	17.9	16.3	21.1	10.9	22.1	18.7
775	19.5	15.8	19.7	11.8	22.9	17.2
800	20.7	N/A	20.0	9.64	N/A	N/A

Table A2 Thermal expansion data for Hydroxyapatite samples number 7, 8, and 10 from Figures 3-26 to 3-27.

Temperature (°C)	6 ( $\mu\text{m}/\text{m } ^\circ\text{C}$ )		7 ( $\mu\text{m}/\text{m } ^\circ\text{C}$ )		8 ( $\mu\text{m}/\text{m } ^\circ\text{C}$ )	
	Heat	Cool	Heat	Cool	Heat	Cool
50	12.7		13.7		11.6	
75	12.8		13.0		12.5	
100	13.0		12.9		12.5	
125	12.8	16.9	13.0	15.7	13.2	17.2
150	13.3	17.4	13.6	15.5	13.4	18.2
175	13.9	18.2	13.7	15.8	9.58	18.6
200	13.5	15.6	14.1	16.0	10.4	16.7

Appendix A

Table A2 continued

Temperature (°C)	6 (µm/m °C)		7 (µm/m °C)		8 (µm/m °C)	
	Heat	Cool	Heat	Cool	Heat	Cool
225	14.5	17.9	13.9	16.1	11.6	17.7
250	14.7	18.9	14.3	16.3	13.2	17.5
275	15.4	18.6	14.9	16.3	13.7	13.3
300	14.9	18.5	14.9	16.7	15.3	19.1
325	15.7	17.2	15.1	16.4	15.7	18.5
350	16.6	17.4	14.8	16.7	15.4	N/A
375	17.3	19.2	14.9	16.8	15.9	19.5
400	14.9	15.3	15.4	17.0	15.6	20.3
425	16.5	18.9	14.8	14.2	17.0	19.6
450	17.5	18.8	15.6	13.3	16.7	21.1
475	18.4	13.5	15.0	18.4	17.5	21.6
500	18.3	16.2	15.8	17.9	16.9	19.6
525	19.9	21.0	15.7	17.7	18.3	19.7
550	19.6	20.0	17.1	19.5	16.8	19.4
575	17.8	20.6	18.2	19.8	18.1	20.5
600	20.9	20.6	18.9	21.2	19.0	19.8
625	24.0	21.4	23.4	23.4	27.8	17.5
650	21.3	20.0	20.2	19.4	16.8	18.5
675	21.1	18.5	20.1	18.5	23.51	18.3
700	20.0	17.7	22.3	15.6	18.9	18.4
725	19.7	16.4	22.1	15.2	19.6	16.4
750	20.2	15.9	20.5	14.6	18.9	N/A
775	21.6	15.2	20.9	15.4	19.9	18.5
800	27.2	N/A	21.1	14.0	28.9	N/A

APPENDIX A

Table A3 Thermal expansion data for Hydroxyapatite samples numbers 10, 11, and 12 from Figures 3-26 to 3-27.

Temperature (°C)	10 (μm/m °C)		11 (μm/m °C)		12 (μm/m °C)	
	Heat	Cool	Heat	Cool	Heat	Cool
50	12.6	N/A	12.8	N/A	11.9	18.8
75	12.8	N/A	13.2	18.3	12.3	23.1
100	13.0	N/A	13.4	19.1	12.1	22.7
125	13.8	19.1	13.4	19.1	11.4	21.2
150	14.4	18.2	13.9	14.3	11.0	21.1
175	14.4	19.4	14.2	17.6	12.0	N/A
200	14.7	20.5	13.2	20.8	13.5	20.0
225	14.4	19.0	13.7	17.3	14.0	19.7
250	15.1	13.3	13.9	16.2	14.4	18.0
275	15.8	18.8	14.1	17.3	14.3	18.6
300	15.6	18.4	15.0	17.4	14.6	17.6
325	15.9	19.8	15.5	18.7	14.9	N/A
350	17.1	21.7	16.1	17.0	14.9	17.1
375	16.9	18.4	16.3	19.1	15.3	17.5
400	17.8	17.8	16.7	16.8	15.4	17.7
425	17.5	18.1	16.2	17.9	16.2	13.3
450	18.7	13.4	17.2	18.2	16.5	14.7
475	16.3	19.1	17.9	19.5	16.8	16.2
500	18.9	N/A	18.0	18.6	16.5	14.9
525	19.6	20.3	18.2	18.7	16.9	16.1
550	19.7	21.3	18.9	19.7	16.7	17.1
575	20.3	20.5	19.9	20.3	18.4	17.7
600	22.1	22.4	18.9	20.9	17.5	21.2

APPENDIX A

Table A3 continued

625	25.0	23.8	22.9	19.8	20.5	19.6
650	21.5	20.7	20.6	19.4	17.6	17.5
675	21.1	22.5	21.5	22.3	17.3	16.7
700	20.7	20.8	19.8	18.3	16.6	16.2
725	20.8	21.1	19.8	21.0	19.5	10.3
750	20.6	21.5	20.1	21.5	17.9	16.3
775	21.2	19.8	22.3	N/A	18.1	10.1
800	26.9	18.5	23.2	N/A	19.6	N/A

Table A4 Thermal expansion data for the alumina sample number 1 with 1 g weight, alumina number 1 with 5 g weight (denoted 1a) and alumina sample number 2.

Temperature (°C)	1 (μm/m °C)		1a (μm/m °C)		2 (μm/m °C)	
	Heat	Cool	Heat	Cool	Heat	Cool
50	5.24		4.92	5.27		
75	5.66		5.40	5.62		
100	5.80		5.84	5.76	5.49	
125	6.26	8.77	6.06	6.09		
150	6.57	8.38	6.38	6.41		
175	6.73	8.78	6.74	6.85		
200	7.09	8.24	7.03	7.03	6.76	8.90
225	7.14	8.53	7.38	7.36		
250	7.42	8.71	7.28	7.58		
275	7.56	8.92	7.77	7.69		
300	7.8	8.77	8.12	7.95	8.61	9.20
325	7.86	8.77	8.31	8.21		
350	8.35	8.96	8.90	8.39		

APPENDIX A

Table A4 continued

Temperature (°C)	#1 (µm/m °C )		#1a (µm/m °C )		#2 (µm/m °C )	
	Heat	Cool	Heat	Cool	Heat	Cool
375	9.36	9.04	8.72	8.73		
400	8.9	9.20	9.00	9.09	9.15	9.36
425	9.15	9.57	9.15	9.18		
450	9.4	9.25	9.36	9.1		
475	9.95	9.58	9.40	8.97		
500	9.93	8.95	9.82	9.89	11.0	8.81
525	9.97	9.35	9.95	9.69		
550	11.0	8.99	10.4	10.1		
575	10.5	9.54	9.66	10.8		
600	10.5	8.67	9.96	10.3	9.16	9.40
625	10.5	8.62	11.0	11.5		
650	10.3	8.32	10.3	10.9		
675	11.3	8.48	10.9	10.7		
700	10.7	7.31	11.5	11.5	12.2	8.83
725	9.24	7.36	9.99	11.5		
750	11.8	5.96	12.3	11.5		
775	10.2	7.26	11.1	11.5		

APPENDIX A

Table A5 The averaged thermal expansion data for sintered hydroxyapatite (from Tables A1,A2 and A3) and alumina (from Table A4).

Temperature (°C)	HAP ( $\mu\text{m}/\text{m } ^\circ\text{C}$ )		Alumina ( $\mu\text{m}/\text{m } ^\circ\text{C}$ )	
	Heat	Cool	Heat	Cool
50	12.32	18.8	5.14	5.27
75	12.79	19.07	5.56	5.62
100	12.89	19.07	5.72	5.76
125	13.01	17.21	6.14	7.43
150	13.39	17.36	6.45	7.40
175	13.35	18.06	6.77	7.82
200	13.66	18.41	6.98	8.06
225	14.03	18.34	7.29	7.95
250	14.30	17.84	7.43	8.15
275	14.80	18.06	7.67	8.31
300	15.21	17.78	8.12	8.64
325	15.50	17.55	8.13	8.49
350	15.81	17.74	8.55	8.68
375	16.09	18.41	8.94	8.89
400	16.41	17.42	9.04	9.22
425	16.54	17.37	9.16	9.38
450	16.87	18.06	9.29	9.18
475	16.93	18.77	9.44	9.28
500	17.46	18.78	10.16	9.22
525	18.17	19.37	9.87	9.52
550	18.18	19.90	10.50	9.55
575	18.89	19.78	10.32	10.17
600	19.08	20.77	9.98	9.46

APPENDEIX A

Table A5 continued

Temperature (°C)	HAP ( $\mu\text{m}/\text{m } ^\circ\text{C}$ )		Alumina ( $\mu\text{m}/\text{m } ^\circ\text{C}$ )	
	Heat	Cool	Heat	Cool
650	19.72	19.01	10.5	9.61
675	20.80	18.81	10.97	9.59
700	20.06	17.52	11.48	9.21
725	20.51	17.22	10.24	9.43
750	19.92	16.96	11.87	8.73
775	20.68	15.48	10.93	9.38
800	23.45	14.05	N/A	N/A

## APPENDIX B

### Appendix B The dielectric data

The calculated relative permittivity and the measured quality factor Q, for the Alumina substrate (ADS 995) and hydroxyapatite specimens numbers 14, 16, 33, 36, 41-46, 49, 50. The data was taken in the frequency range 45 kHz to 7.3 MHz.

Table B1 Dielectric data for alumina substrate (1.016 mm in thickness).

Frequency (kHz)	Relative permittivity	Q
45.0	9.9	333
72.17	9.3	244
101.62	8.8	268
160.77	10.2	235
307.17	8.7	196
702.20	9.9	309
1641.90	9.9	217
3112.91	9.6	246
7302.00	11.4	195

## APPENDIX B

**Table B1** Dielectric data for hydroxyapatite specimen number 14 (2.845 mm in thickness).

Frequency (kHz)	Relative Permittivity	Q
45.0	13.6	52.6
72.17	13.3	25.4
101.62	13.2	30.3
160.77	14.1	35.9
307.17	12.2	42.5
702.20	13.1	50.7
1641.90	12.1	55.9
3112.91	10.4	58.1
7302.00	11.9	69.2

**Table B1** Dielectric data for hydroxyapatite specimen number 16 (2.969 mm in thickness).

Frequency (kHz)	Relative Permittivity	Q
45.0	12.6	56.2
72.17	12.6	27.0
101.62	10.6	35.8
160.77	12.9	37.1
307.17	12.8	44.4
702.20	13.7	64.4
1641.90	10.7	84.8
3112.91	8.9	80.8
7302.00	9.9	115

APPENDIX B

Table B1 Dielectric data for hydroxyapatite specimen number 33 (1.123 mm in thickness).

Frequency (kHz)	Relative Permittivity	Q
45.0	4.9	185
72.17	4.7	105
101.62	4.1	96.8
160.77	4.7	82.8
307.17	4.3	108
702.20	5.4	93.7
1641.90	5.4	84.4
3112.91	4.6	104
7302.00	4.5	132

Table B1 Dielectric data for hydroxyapatite specimen number 36 (1.730 mm in thickness).

Frequency (kHz)	Relative Permittivity	Q
45.0	5.6	186
72.17	3.9	87.7
101.62	4.8	93.9
160.77	5.5	77.6
307.17	3.8	90.8
702.20	5.2	79.2
1641.90	5.4	65.6
3112.91	5.2	84.6
7302.00	4.6	88.2

## APPENDIX B

**Table B1** Dielectric data for hydroxyapatite specimen number 41 (0.866 mm in thickness).

Frequency (kHz)	Relative Permittivity	Q
45.0	7.9	156
72.17	7.8	108
101.62	7.5	114
160.77	7.8	95.4
307.17	7.4	101
702.20	7.8	86.3
1641.90	8.3	71.7
3112.91	8.1	61.4
7302.00	8.2	42.4

**Table B1** Dielectric data for hydroxyapatite specimen number 42 (1.113 mm in thickness).

Frequency (kHz)	Relative Permittivity	Q
45.0	12.5	37.2
72.17	12.3	26.3
101.62	11.5	28.7
160.77	11.9	33.1
307.17	11.5	41.8
702.20	11.7	49.9
1641.90	12.3	56.3
3112.91	11.6	72.3
7302.00	12.6	72.6

## APPENDIX B

**Table B1** Dielectric data for hydroxyapatite specimen number 43 (1.336 mm in thickness).

Frequency (kHz)	Relative Permittivity	Q
45.0	11.6	127
72.17	10.6	70.4
101.62	11.0	92.7
160.77	11.0	125
307.17	10.7	87.8
702.20	11.0	134
1641.90	10.9	139
3112.91	11.2	133
7302.00	13.0	119

**Table B1** Dielectric data for hydroxyapatite specimen number 44 (1.214 mm in thickness).

Frequency (kHz)	Relative Permittivity	Q
45.0	11.6	110
72.17	11.6	78.6
101.62	11.7	87.2
160.77	11.0	95.8
307.17	10.9	134
702.20	11.0	155
1641.90	12.1	165
3112.91	12.2	177
7302.00	12.9	148

## APPENDIX B

**Table B1** Dielectric data for hydroxyapatite specimen number 45 (1.610 mm in thickness).

Frequency (kHz)	Relative Permittivity	Q
45.0	12.1	229
72.17	11.3	148
101.62	10.6	168
160.77	11.6	135
307.17	11.2	152
702.20	11.2	173
1641.90	12.2	164
3112.91	11.7	156
7302.00	12.5	131

**Table B1** Dielectric data for hydroxyapatite specimen number 46 (1.651 mm in thickness).

Frequency (kHz)	Relative Permittivity	Q
45.0	11.6	184
72.17	11.3	97.3
101.62	11.6	106
160.77	11.4	158
307.17	11.1	108
702.20	10.4	179
1641.90	11.1	112
3112.91	10.9	138
7302.00	11.9	111

**APPENDIX B**

**Table B1** Dielectric data for hydroxyapatite specimen number 49 (1.580 mm in thickness).

Frequency (kHz)	Relative Permittivity	Q
45.0	12.0	245
72.17	11.1	154
101.62	11.4	146
160.77	11.3	158
307.17	11.2	157
702.20	10.6	199
1641.90	10.8	166
3112.91	11.1	127
7302.00	11.0	157

**Table B1** Dielectric data for hydroxyapatite specimen number 50 (1.595 mm in thickness).

Frequency (kHz)	Relative Permittivity	Q
45.0	11.5	188
72.17	11.2	136
101.62	11.2	140
160.77	10.1	93.1
307.17	11.0	103
702.20	10.8	132
1641.90	11.0	123
3112.91	11.2	106
7302.00	11.2	150

## References

- [1] Larry L. Hench, "Bioceramics". *Journal of the American Ceramic Society*, 81 [7], pp.1705-1727 (1998).
- [2] A.M.J.H. Sueter, "Existence Region of Calcium Hydroxylapatite and the Equilibrium with Coexisting Phases at Elevated Temperatures", *Reactivity of Solids*, pp 806-812, J.S. Anderson, M.W. Roberts, Eds., Chapman and Hall, London (1972).
- [3] P. V. Riboud, "Composition and stability of apatites in the system CaO-P<sub>2</sub>O<sub>5</sub> - Iron oxide - H<sub>2</sub>O at high temperatures", *Annales de chimie*, 8 pp 381-390 (1973).
- [4] J.C. Trombe, G. Montel, "Some Features of the Incorporation of Oxygen in Different Oxidation States in the Apatitic Lattice-I", *J. Inorg. Nucl. Chem.* Vol. 40, pp 15-21, (1978).
- [5] R. M. H. Verbeek, H. J. M. Heiligers, F. C. M. Driessens, and H. G. Schaeken, "Effect of Dehydration of Calcium Hydroxylapatite on its Cell Parameters", *Z. anorg. allg. Chem.* 466, pp 76-80, (1980).
- [6] Jiming Zhou, Xingdong Zhang, Jiyong Chen, "High temperature characteristics of synthetic hydroxyapatite", *Journal Of Materials Science: Materials in Medicine*, 4 pp 83-85 (1993).
- [7] A. Royer, J.C. Viguie, M. Heughebaert, J.C. Heughebaert: "Stoichiometry of Hydroxyapatite: influence on the Flexural Strength", *Journal of Materials Science: Materials in Medicine*, 4, pp76-82, (1993).
- [8] Kimihiro Yamashita, Kazuhisa Kitagaki, and Takao Umegaki: "Thermal Instability and Proton Conductivity of Ceramic Hydroxyapatite at High Temperatures", *Journal of the American Ceramic Society*, 78 [5], pp.1191-1197 (1995).
- [9] Pauchiu E. Wang, T.K. Chaki: "Sintering Behaviour and Mechanical Properties of Hydroxyapatite and Dicalcium Phosphate", *Journal of Materials Science: Materials in Medicine* 4 pp.150-158, (1993).
- [10] A.J. Ruys, C.C. Sorrel, A. Brandwood, B.K. Milthorpe: "The Effects of Sintering Atmosphere on the Chemical Compatibility of Hydroxyapatite and Particle Additives at 1200° C", *Journal of Materials Science: Materials in Medicine*, 6, pp297-301, (1995).

- [11] Anna Slosarczyk, Ewa Stobierska, Zofia Paskiewicz, Mark Gawlicki: "Calcium Phosphate Materials Prepared from Precipitates with Various Calcium:Phosphorus Molar Ratios", *Journal of the American Ceramic Society*, 79 [10], 2539-2544 (1996).
- [12] Wojciech L. Suchanek and Masahiro Yoshimura, "Preparation of Fibrous, Porous Hydroxyapatite Ceramics from Hydroxyapatite Whiskers", *Journal of the American Ceramic Society*, 81, [3], pp 765-767, (1998).
- [13] Kazuo Kondo, Masahiko Okuyama, Hidetoshi Ogawa and Yoshimasa Shibata, "Preparation of High-Strength Apatite Ceramics", *Communications of the American Ceramic Society*, November 1984, pp C222-223.
- [14] W. Fix, H. Heymann and R. Heinke, "Subsolidus Relations in the System  $2\text{CaO SiO}_2\text{-}3\text{CaO P}_2\text{O}_5$ ", *Journal of the American Ceramic Society*, 52, [6] pp 46-47 (1969).
- [15] J.C. Elliott, *Structure and Chemistry of the Apatites and Other Calcium Orthophosphates*, Elsevier, (1994).
- [16] Sir Lawrence Bragg, G.F. Claringbull, W.H. Taylor: *Crystal Structures of Minerals*, Cornell University Press.
- [17] Ralph W.G. Wyckoff: *Crystal Structures Volume 3 Inorganic Compounds  $R_x(M X_4)_y, R_x(M_n X_p)_y$ , Hydrates and Ammoniates*, Second Edition, Interscience Publishers.
- [18] D.E.C. Corbridge; *Studies in Inorganic Chemistry 20, Phosphorous An Outline of its Chemistry and Uses*, Fifth Edition, Elsevier (1995).
- [19] Tsuyoshi Kijima and Masayuki Tsutsumi, "Preparation and Thermal Properties of Dense Polycrystalline Oxyhydroxyapatite", *Journal of the American Ceramic Society*, 62 [9-10], pp.455-460 (1979)
- [20] M. Akao, H. Aoki, K. Kato, "Mechanical Properties of Sintered Hydroxyapatite for Prosthetic Applications", *Journal of Material Science*, 16, pp.809-812 (1981).
- [21] Keizo Uematsu, Masaki Takagi, Tsunehiro Honda, Nozumu Uchida and Katsuichi Saito: "Transparent Hydroxyapatite Prepared by Hot Isostatic Pressing of Filter Cake", *Journal of the American Ceramic Society*, 72 [8], pp.1476-1478, (1989).

- [22] A. Cuneyt Tas, F. Korkusuz, M. Timucin, N. Akkas: "An Investigation of the Chemical Synthesis and High Temperature Sintering Behaviour of Calcium Hydroxyapatite (HA) and Tricalcium Phosphate (TCP) Bioceramics", *Journal of Materials Science: Materials in Medicine* 8 pp.91-96, (1997).
- [23] Yi Fang, Dinesh K. Agrawal, Della M. Roy, and Rustum Roy: "Fabrication of Porous Hydroxyapatite Ceramics by Microwave Processing", *Journal of Material Research*, Vol. 7 No. 2, pp.490-494 (1992).
- [24] J.C. Elliott, P.E. Mackie, R.A. Young: "Monoclinic Hydroxyapatite", *Science*, Vol 180, pp.1055-1057 (1973).
- [25] H.B. Van Rees, M. Mengeot, E. Kostiner: "Monoclinic-Hexagonal Transition in Hydroxyapatite and Deuterhydroxyapatite Single Crystals", *Mat. Res. Bull.* Vol 8, No. 11, pp.1307-1309 (1973).
- [26] Toshiyuki Ikoma, Atsushi Yamazaki: "Preparation and Dielectric Property of Sintered Monoclinic Hydroxyapatite", *Journal of Materials Science Letters* 18, pp.1225-1228 (1999).
- [27] Hiroyuki Suda, Masatomo Yashima, Masoto Kakihana, and Masahiro Yoshimura, "Monoclinic ↔ Hexagonal Phase Transition in Hydroxyapatite Studied by X-ray Powder Diffraction and Differential Scanning Calorimetry Techniques", *J. Phys. Chem.*, 99, pp 6752-6754, (1995).
- [28] G. R. Fischer, P. Bardhan, J. E. Geiger, "The lattice thermal expansion of hydroxyapatite", *Journal of Materials Science Letters*, 2, pp 577-578, (1983).
- [29] W.G. Perdok, J Christoffersen and J. Arends, "The Thermal Lattice Expansion of Calcium Hydroxyapatite", *Journal of Crystal Growth*, 80, pp 149-154, (1987).
- [30] M. Jarcho, C.H. Bolen, M.B. Thomas, J. Bobick, J.F. Kay, R.H. Doremus, "Hydroxylapatite synthesis and characterization in dense polycrystalline form", *Journal of Materials Science*, 11, pp 2027-2035, (1976).
- [31] Je-Won Choi, Young-Min Kong and Hyoun-Ee Kim, In-Seop Lee, "Reinforcement of Hydroxyapatite Bioceramic by Addition of Ni<sub>3</sub>Al and Al<sub>2</sub>O<sub>3</sub>", *Journal of the American Ceramic Society*, 81, [7], pp 1743-1748, (1998).
- [32] M. Mathew, L.W. Schroeder, B. Dickens and W.E. Brown: "The Crystal Structure of α-Ca<sub>3</sub>(PO<sub>4</sub>)<sub>2</sub>", *Acta Cryst.* B33, pp1325-1333 (1977).

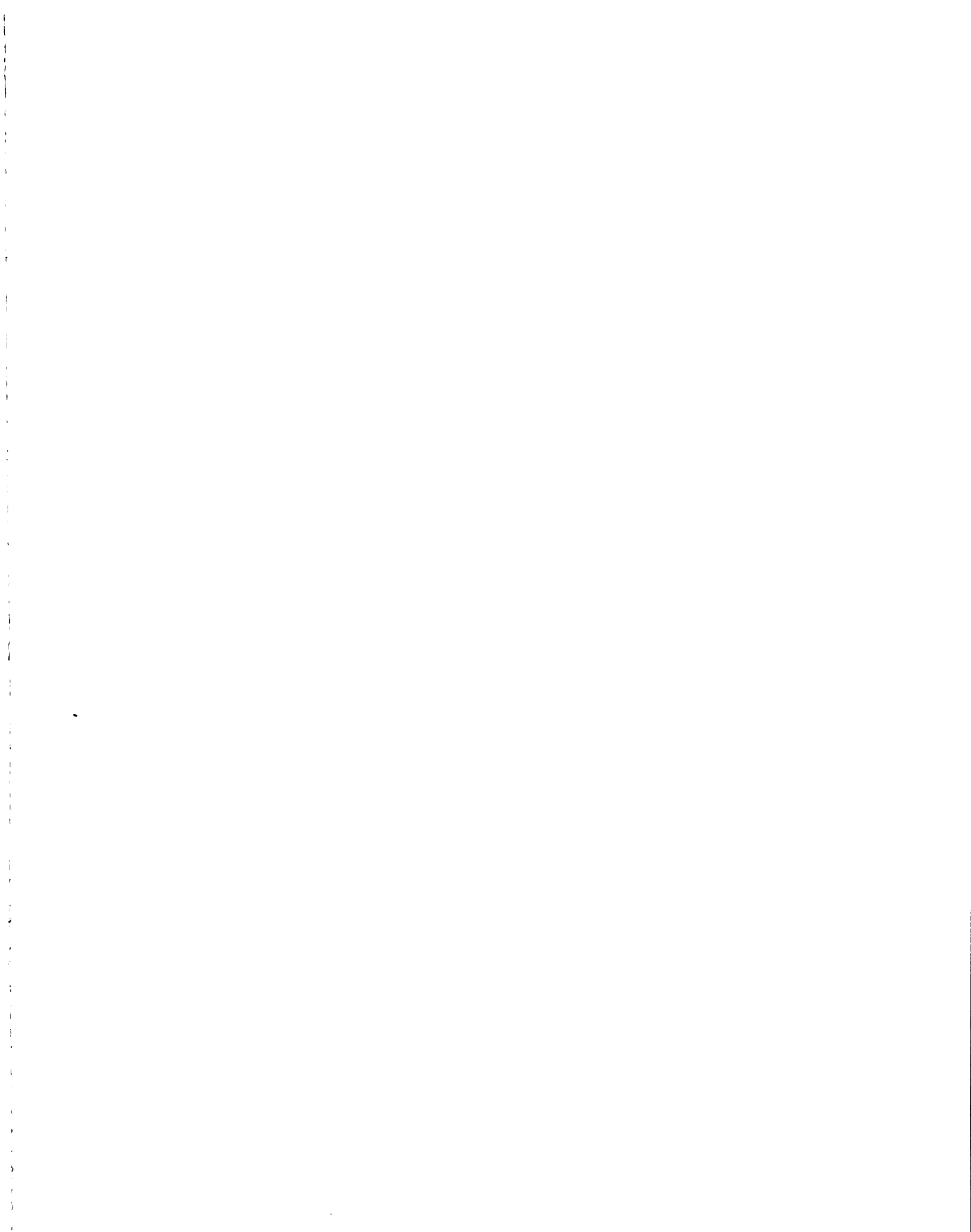
- [33] B. Dickens, L.W. Schroeder, and W.E. Brown, "Crystallographic Studies of the Role of Mg as a Stabilizing Impurity in  $\beta$ -Ca<sub>3</sub>(PO<sub>4</sub>)<sub>2</sub>. I. The Crystal Structure of Pure  $\beta$ -Ca<sub>3</sub>(PO<sub>4</sub>)<sub>2</sub>", *Journal of Solid State Chemistry* 10, pp 232-248, (1974).
- [34] B. Dickens, W.E. Brown, G.J. Kruger and J.M. Stewart, "Ca<sub>4</sub>(PO<sub>4</sub>)<sub>2</sub>O, Tetracalcium Diphosphate Monoxide. Crystal Structures and relationships to Ca<sub>3</sub>(PO<sub>4</sub>)<sub>3</sub>OH and K<sub>3</sub>Na(SO<sub>4</sub>)<sub>2</sub>", *Acta Cryst.* B29, pp 2046-2056, (1973)
- [35] W.D. Kingery, H.K. Bowen, D.R. Uhlmann, *Introduction to Ceramics*, Second Edition, John Wiley & Sons, 1976.
- [36] J.J Cleveland and R.C. Bradt, "Grain Size/Microcracking Relations for Pseudobrookite Oxides", *Journal of the American Ceramic Society*, 61, [11-12], pp 478-481, (1978).
- [37] Bernard J. Hockey, "Plastic Deformation of Aluminum Oxide by Indentation and Abrasion", *Journal of the American Ceramic Society*, 54, [5], pp 223-231, (1971).
- [38] Brian Lawn, Rodney Wilshaw, "Review Indentation Fracture: principles and applications", *Journal of Materials Science*, 10, pp 1049-1081, (1975).
- [39] A.G. Evans and E.A. Charles, "Fracture Toughness Determinations by Indentation", *Journal of the American Ceramic Society*, 59, [7-8], pp 371-372, (1976).
- [40] G.R. Anstis, P. Chantikul, B.R. Lawn, and D.B. Marshall, "A Critical Evaluation of Indentation Techniques for measuring Fracture Toughness: I, Direct Crack Measurements", *Journal of the American Ceramic Society*, 64, [9], pp 533-538, (1981).
- [41] James Lankford, "Indentation microfracture in the Palmqvist crack regime: implications for fracture toughness evaluation by the indentation method", *Journal of Materials Science Letters*, 1, pp 493-495, (1982).
- [42] M.T. Laugier, "Palmqvist cracking in WC-Co composites", *Journal of Material Science Letters*, 4, pp 207-210, (1985).
- [43] Roy W. Rice, Carl Cm. Wu, and Fred Borchelt, "Hardness-Grain-Size Relations in Ceramics", *Journal of the American Ceramic Society*, 77, [10], pp 2539-2553, (1994).
- [44] Andreas Krell and Paul Blank, "Grain Size Dependence of Hardness in Dense Submicrometer Alumina", *Journal of the American Ceramic Society*, 78, [4], (1995).

- [45] M. Desmaison-Brut and J. Montintin, F. Valin and M. Boncoeur, "Influence of Processing Conditions on the Microstructure and Mechanical Properties of Sintered Yttrium Oxides", *Journal of the American Ceramic Society*, 78, [3], pp 716-722, (1995).
- [46] M.J. Mayo, R.W. Siegel and Y.X. Liao, W.D. Nix, "Nanoindentation of nanocrystalline ZnO", *Journal of Materials Research*, 7, (4) pp 973-979, (1992).
- [47] M.J. Mayo, R.W. Siegel and A. Narayanasamy, W.D. Nix, "Mechanical properties of nanophase TiO<sub>2</sub> as determined by nanoindentation", *Journal of Materials Research*, 5, (5), pp 1073-1082, (1990).
- [48] J. Ricote, L. Pardo, B. Jimenez, "Mechanical characterization of calcium-modified lead titanate ceramics by indentation methods", *Journal of Materials Science* pp 3248-3254, (1994).
- [49] Dong Soo Baik, Kwang Soo No and John Soung-Soon Chun, "Mechanical Properties of Mica Glass-Ceramics", *Journal of the American Ceramic Society*, 78, [5], pp 1217-1222, (1995).
- [50] Jie Luo, R. Stevens, Wai Lo, A.M. Campbell, "Anisotropic plastic and elastic-deformation in highly textured superconducting (Bi, Pb)<sub>2</sub> Sr<sub>2</sub> Ca<sub>2</sub> Cu<sub>3</sub> O<sub>x</sub> ceramics", *Journal of Materials Science*, 30, (12), pp 3050-3056, (1995).
- [51] Naoto Hirosaki and Yoshio Akimune, "Effect of Grain Growth of β-Silicon Nitride on Strength, Weibull Modulus, and Fracture Toughness", *Journal of the American Ceramic Society*, 76, [7], pp 1892-1894, (1993).
- [52] R.W. Rice, R.C. Pohanka, and W.J. McDonough, "Effect of Stresses from Thermal Expansion Anisotropy, Phase Transformations, and Second Phases on the Strength of Ceramics", *Journal of the American Ceramic Society*, 63, [11-12], pp 703-710, (1980).
- [53] R.W. Rice, "Grain size and porosity dependence of ceramic fracture energy and toughness at 22<sup>o</sup> C", *Journal of Materials Science*, 31, pp 1969-1983, (1996).
- [54] G. DeWith, H.J.A. Van Dijk, N. Hattu, K. Prijs, "Preparation, microstructure and mechanical properties of dense polycrystalline hydroxy apatite", *Journal of Material Science*, 16, pp 1592-1598, (1981).
- [55] R. Halouni, D. Bernache-Assolant, E. Champion, A. Ababou, "Microstructure and related properties of hot pressed hydroxyapatite ceramics", *Journal of Material Science: Materials in Medicine*, 5, pp 563-568, (1994).

- [56] Wojciech Suchanek, Masatomo Yashima, Masato Kakihana and Masahiro Yoshimura, "Hydroxyapatite/Hydroxyapatite-Whisker Composites without Sintering Additives: Mechanical Properties and Microstructural Evolution", *Journal of the American Ceramic Society*, 80, [11], pp 2805-2813, (1997).
- [57] R.W. Rice, "Evaluation and extension of physical property-porosity models based on minimum solid area", *Journal of Materials Science*, 31, pp 102-118, (1996).
- [58] R.W. Rice, "Comparison of physical property-porosity behaviour with minimum solid area models", *Journal of Material Science*, 31, pp 1509-1528, (1996).
- [59] T.H. Nielson and M.H. Leipold, "Thermal Expansion in Air of Ceramic Oxides to 2200<sup>o</sup> C", *Journal of the American Ceramic Society*, 46, [8], pp 381-387, (1963).
- [60] R.L. Coble and W.D. Kingery, "Effect of Porosity on Physical Properties of Sintered Alumina", *Journal of the American Ceramic Society*, 39, [11], pp 377-385, (1956).
- [61] W.R. Manning, O. Hunter Jr., F.W. Calderwood, and D.W. Stacy, "Thermal Expansion of Nb<sub>2</sub>O<sub>5</sub>", *Journal of the American Ceramic Society*, 55, [7], pp 342-347, (1972).
- [62] J.A. Kuszyk and R.C. Bradt, "Influence of Grain Size on Effects of Thermal Expansion Anisotropy in MgTi<sub>2</sub>O<sub>5</sub>", *Journal of the American Ceramic Society*, 56, [8], pp 420-423, (1973).
- [63] Fred J. Parker and Roy W. Rice, "Correlation between Grain Size and Thermal Expansion for Aluminum Titanate Materials", *Communications of the American Ceramic Society*, 72, [12], pp 2364-2366, (1989).
- [64] E.D. Case, J.R. Smyth, O. Hunter Jr., "Microcrack Healing During Temperature Cycling of Single Phase Ceramics", *Fracture Mechanics of Ceramics, Volume 5*, Plenum Press (1983).
- [65] J.P. Calame, A. Birman, Y. Carmel, D. Gershon, and B. Levush, A.A. Sorokin and V.E. Semenov, D. Dadon, L.P. Martin and M. Rosen, "A dielectric mixing law for porous ceramics based on fractal boundaries", *Journal of Applied Physics*, 80, (7), pp 3992-4000, (1996).
- [66] Particle size distribution test (16 March 2000), Hydroxyapatite powder item number C-2071-1, Batch number X16907-T, run number 13112, measurement number 364, Batch number X21949, run number 13113, measurement number 372, Cerac Incorporated, Milwaukee, WI.
- [67] Type R N.I.S.T Monograph 175 Revised to ITS-90, "Revised Thermocouple Reference Tables", Published by Omega Engineering, Stamford CT.

- [68] Emscope SC500 instruction booklet.
- [69] *Powder diffraction file for inorganic phases*, American Society for Testing and Materials, Philadelphia, PA, 1967.
- [70] B.D. Cullity, *Elements of X-Ray Diffraction* Second Edition, Addison-Wesley Publishing Company, Inc. 1978.
- [71] J.B. Wachtman, *Mechanical Properties of Ceramics*, pp 82-84, John Wiley and Sons, New York, 1996.
- [72] Thin Film Substrates Technical Specifications 10-3-0897, Coors Ceramics Company, Golden CO. 1998
- [73] ASTM Designation D 150 - 95, "Standard Test Methods for AC loss Characteristics and Permittivity (Dielectric Constant) of Solid Electrical Insulation", pp26-44.
- [74] Hui Lu, Zhe Qu, Yanchun Zhou, "Preparation and mechanical properties of dense polycrystalline hydroxyapatite through freeze drying", *Journal of Materials Science: Materials in Medicine*, 9, pp 583-587, (1998).
- [75] S. Best, W. Bonfield, "Processing behaviour of hydroxyapatite powders with contrasting morphology", *Journal of Materials Science*, pp 515-521, (1994).
- [76] Champion E, Gautier S, BernacheAssolant D, "Characterization of hot pressed  $\text{Al}_2\text{O}_3$  -platelet reinforced hydroxyapatite composites", *Journal of Materials Science: Materials in Medicine*, 7, pp 125-130, (1996).
- [77] Yeong-Shyung Chou and David J. Green, "Silicon Carbide Platelet/Alumina composites: II, Mechanical Properties", *Journal of the American Ceramic Society*, 76, [6], pp 1452-1458, (1993).
- [78] Tancret F, Desgardin G, Osterstock F, "Influence of porosity on the mechanical properties of cold isostatically pressed and sintered  $\text{YBa}_2\text{Cu}_3\text{O}_{7-x}$  superconductors", *Philosophical Magazine A*, vol. 75 (2), pp 505-523 Feb. (1997).
- [79] D.R. Clarke, "The Development of High-Tc Ceramic Superconductors: An Introduction", *Advanced Ceramic Materials*, Volume 2/Number 3B/July 1987, Published by the American Ceramic Society (1987)
- [80] Dale E. Grenoble, J. Lawrence Katz, Karl L. Dunn, Robert S. Gilmore and K. Linga Murty, "The Elastic Properties of Hard Tissues and Apatites", *Journal of Biomedical Research*, Vol. 6 pp 221-233, (1972).

- [81] E.D. Case, J.R. Smyth, "Room-temperature fracture energy of monoclinic  $Gd_2O_3$ ", *Journal of Materials Science Letters* 16 pp 3215-3217 (1981).
- [82] Michel W. Barsoum, *Fundamentals of Ceramics*, McGraw-Hill 1997.
- [83] Becher PF, "Microstructural design of toughened ceramics", *Journal of the American Ceramic Society*, 74, [2], pp 255-269, (1991).
- [84] ElRaghy T, Zavalianos A, Barsoum MW, Kalidindi SR, "Damage mechanisms around hardness indentations in  $Ti_3SiC_2$ ", *Journal of the American Ceramic Society*, 80, [2], pp 513-516, (1997).
- [85] R. W. Rice, "Limitations of pore-stress concentrations on the mechanical properties of porous materials", *Journal of Materials Science*, 32, pp 4731-4736 (1997).
- [86] Yi DQ, Li CH, "MoSi<sub>2</sub>-ZrO<sub>2</sub> composites-fabrication, microstructure and properties", *Material Science and Engineering A Vol 261:(1-2)* pp 89-98 (1999).
- [87] *American Institute of Physics Handbook Second Edition*, p 4-72, McGraw-Hill Book Company, Inc., New York, NY, 1963.
- [88] Howard V. Malmstadt, Christie G. Enke, Stanley R. Church, *Electronics and Instrumentation for Scientists*, page 476, The Benjamin/Cummings Publishing Company, Inc., Reading MA, 1981.
- [89] M.A. Fanovich, M.S. Castro, J.M. Porto Lopez, "Analysis of the microstructural evolution in hydroxyapatite ceramics by electrical characterisation", *Ceramics International*, 25, pp 517-522, (1999).
- [90] B.R. Lawn, A.G. Evans, "A model for crack initiation in elastic/plastic indentation fields", *Journal of Material Science*, 12, pp 2195-2199, (1977).



MICHIGAN STATE UNIVERSITY LIBRARIES



3 1293 02088 2753